MEASURING RELIABLE AGES FOR STARS: CALIBRATION OF THE [C/N] CHEMICAL CLOCK AND THE IMPACT OF ATOMIC DIFFUSION ON ABUNDANCE/AGE DETERMINATION OF MAIN SEQUENCE TURNOFF STARS

by

TAYLOR M. SPOO

Bachelor of Science, 2019
Angelo State University
San Angelo, TX

Master of Science, 2021
Texas Christian University
Fort Worth, TX

Submitted to the Graduate Faculty of the
College of Science and Engineering
Texas Christian University
in partial fulfillment of the requirements
for the degree of

Doctorate of Philosophy

August 2024

MEASURING RELIABLE AGES FOR STARS: CALIBRATION OF THE [C/N] CHEMICAL CLOCK AND THE IMPACT OF ATOMIC DIFFUSION ON ABUNDANCE/AGE DETERMINATION OF MAIN SEQUENCE TURNOFF STARS

by

Taylor M. Spoo

Thesis Approved:

Peter M. Frinchaboy III, Major Professor

Kat Barger

Richard Bonde

Jamie Tayar

For The College of Science and Engineering

ACKNOWLEDGEMENTS

I would like to thank my advisor, Dr. Peter M. Frinchaboy, for his mentorship and guidance. Thank you to our REU students Kaitlyn (Summer 2022) and Kaleo (Summer 2023)! I would like to thank my lab mates, John, Amy, Natalie, Alessa, and Jonah, for being my academic family that encouraged and supported me throughout graduate school. I would like to thank my friends and family for their love and support through out the years; I would not be here without you all. I would loike to thank the ASU Physics and Math Departments for preparing me for graduate school, and in particular Dr. Susan Abernathy, and Dr. Kenneth Carrell for their mentorship. Addtionally, I would like to thank my therapist Dr. Lindy Lotz, due to a combination of graduate school and personal life issue she was able help me complete in graduate school. (I highly recommend TCU Counseling & Mental Health Center if you need help with mental health.) Thanks to my cats, Silas and Lola, for all your laughs and cuddles. Finally, I would like to thank my partner, Ashton, for being my biggest supporter.

This research made use of Astropy, a community-developed core Python package for Astronomy (Astropy Collaboration, 2013) as well as Scipy (Virtanen et al. 2020), Numpy (Harris et al. 2020), and Fitsio (Pence 1999). The Author acknowledges support by the National Science Foundation under award AST-1715662 & AST-2206541. Addtionally, the Author gratefully acknowledge support for this research from the National Science Foundation's Research Experience for Undergraduates program (PHY-1852267 & PHY-2244258).

Funding for the Sloan Digital Sky Survey IV has been provided by the Alfred P. Sloan Foundation, the U.S. Department of Energy Office of Science, and the Participating Institutions. SDSS-IV acknowledges support and resources from the Center for High Performance Computing at the University of Utah. The SDSS website is www.sdss.org. SDSS-IV is managed by the Astrophysical Research Consortium for the Participating Institutions of the SDSS Collaboration including the Brazilian Participation Group, the Carnegie Institution for Science, Carnegie Mellon University, Center for Astrophysics — Harvard & Smithsonian, the Chilean Participation Group, the French Participation Group, Instituto de Astrofísica de Canarias, The Johns Hopkins University, Kavli Institute for the Physics and Mathematics of the Universe (IPMU) / University of Tokyo, the Korean Participation Group, Lawrence Berkeley National Laboratory, Leibniz Institut für Astrophysik Potsdam (AIP), Max-Planck-Institut für Astronomie (MPIA Heidelberg), Max-Planck-Institut für Astrophysik (MPA Garching), Max-Planck-Institut für Extraterrestrische Physik (MPE), National Astronomical Observatories of China, New Mexico State University, New York University, University of Notre Dame, Observatário Nacional / MCTI, The Ohio State University, Pennsylvania State University, Shanghai Astronomical Observatory, United Kingdom Participation Group, Universidad Nacional Autónoma de México, University of Arizona, University of Colorado Boulder, University of Oxford, University of Portsmouth, University of Utah, University of Virginia, University of Washington, University of Wisconsin, Vanderbilt University, and Yale University.

Contents

List of Figures

List of Tables

List of Abbreviations

CMD	Color Magnitude Diagram
HRD	Hertzsprung-Russell Diagram
RV	Radial Velocity (Doppler velocity)
RA	Coordinates of Right Ascension
Dec	Coordinates of Declination
PM	Proper motion (an object's velocity in RA and Dec)
$\log g$	Surface gravity
T_{eff}	Effective Surface Temperature
kpc	kiloparsec
S/N	Signal to Noise Ratio
RC	Red Clump Stars
RGB	Red Giant Branch
SB2	Double Lined Spectroscopic Binaries
FDU	First Dredge-Up
$M_{\odot}$	Solar mass (the mass of the sun)
[Fe/H]	metallicity (on a log scale, relative to the sun)
[C/N]	relative abundance of element C to N, also on a log scale
[X/Fe]	relative abundance of element X to Fe, also on a log scale
APOGEE	Apache Point Observatory Galactic Evolution Experiment
SDSS	Sloan Digital Sky Survey
OCCAM	Open Cluster Chemical Abundance and Mapping Survey
2MASS	2 Micron All Sky Survey
ASPCAP	APOGEE Stellar Parameter and Chemical Abundance Pipeline
DR17	17^{th} Data Release from SDSS
VAC	SDSS Value Added Catalog
NGC	New General Catalog (Dreyer 1888)

Chapter 1

Introduction

1.1 General Scientific Introduction

Measuring the age for a star is one of the most difficult tasks in astronomy. Even getting an age for our Sun cannot be measured directly, which has been done through radioactive dating of meteorites. In this work, we calibrate a new method for determining ages of stars, as well as explore a specific complication that needs to be understood to use another recent age determination method. Each of these efforts are tied to requiring a deeper detailed understanding of how stars evolve.

1.1.1 Stellar Evolution

Once a star is formed, it will go through many stages of evolution including main sequence (MS), subgiant branch (SGB), red giant branch (RGB), horizontal branch/red clump (HB/RC), and asymptotic giant branch (AGB). The first stage is the MS phase, this

is where the star will live most of its life burning hydrogen to helium. The length of time stars stay in this stage is based on the mass of the star. The temperature of the core is also dependant on the mass which determines the nuclear process is used to convert hydrogen to helium. The processes are proton-proton (p-p) chains or the carbon-nitrogen-oxygen (CNO) cycle. In particular, the CNO-cycle is an independent process, where carbon, nitrogen, and oxygen are used as catalysts, both destroyed and reformed throughout the process, to convert hydrogen and form helium-4 plus energy to power the star. The CNO-cycle is sensitive to temperature and depending on the mass of the star, the core temperature will change, e.g., a more massive star runs hotter. Hence, stars more massive than the Sun ($M > 1.5M_{\odot}$, Hansen et al. 2004) have higher central temperature and their "hydrogen-burning" is predominately due to CNO-cycle, while lower mass stars are dominated by the p-p chain. When the MS phase ends, the hydrogen burning stops in the core of the star. At this point the star will "turnoff" the main sequence, which is referred to as the main sequence turnoff (MSTO).

For low-mass ($0.7 \lesssim M \lesssim 2M_{\odot}$) and intermediate-mass ($2 \lesssim M \lesssim 9$–$10M_{\odot}$) stars, the first stage off the MS is called the SGB. As the star moves off the MS, the star ceases to burn hydrogen in the core and the core contracts. During this time, the star has a hydrogen-burning shell and shell-burning produces more energy than the core during the MS phase. This causes the luminosity to increase, effective temperature to decrease, and the convective envelopes expand slightly.

The following stage is the RGB phase. During this phase, the convective envelopes expand and surface temperatures drop. Now, the carbon and nitrogen created in the stellar interior from the MS phase of the star are brought to the stellar surface via convective

envelopes. These convective envelopes move material from deeper layers of the star to the surface called dredge-ups. When convective envelope reaches the maximum penetration depth into the core, it is called the first dredge-up (FDU). Due to this convective mixing, the stellar atmosphere will display a variation in the chemical composition.

As the star continues to evolve, it will move up the RGB on the Hertzsprung-Russell diagram (HRD) until it reaches the tip of the RGB. Once at this tip, the star can experience the "helium flash", where the core temperature is hot enough to overcome the Coulomb barrier resulting in helium burning happening all at once within the core. After the He-flash, these evolved stars will begin to settle together next to the RGB portion of the HR diagram called the horizontal branch (HB), where the redder portion is considered the red clump (RC) and sometimes refer to as the "red extremity of the HB". This dichotomy between the RC and HB stars is because RC stars are mostly associated with younger, more metal-rich populations than those associated with HB stars, although RC stars are more abundant than HB stars (Girardi 2016). The RC is an important phase in stellar evolution. These evolved stars are on the "helium main sequence" supported by helium fusion within their core and are found to be slightly hotter, but of similar luminosity to many RGB stars, which can make them difficult to separate in older populations.

After He-burning has exhausted, the star will move from the HB and continue up the AGB. The name AGB comes from the evolutionary track approaching the RGB asymptotically from the left. The AGB can be thought of as the He-burning-shell analog to the RGB H-burning-shell. The star now has a carbon-oxygen core and follows similar steps in evolution as the helium core. There are two shells of burning: (1) He-burning

shell which is dominate and (2) H-burning shell which is nearly inactive. This is a thermally-unstable configuration and results in thermal pulses. Due to less energy being produced, the core will contract and heat up causing envelopes to expand and cool, and convection to begin throughout. Mixing occurs due to the second dredge up inducing an increase in helium and nitrogen abundances. High radiation pressure in the envelope will cause strong stellar winds and consequently the star will lose a significant amount of mass.

1.1.2 Stellar Abundance Analysis Basics

Spectral observations of a star are used to determine the abundance of certain elements within the photosphere, the "surface" of the star, of the star. This is possible because in quantum mechanics it is well known that atoms will absorb photons at particular wavelengths (or energies) and later will release those photons. Applying this knowledge to the "surface" of the star, photons emitted from the deeper interior of the star are then absorbed by atoms in the atmosphere of the star, which produce discrete lines in the spectra. How strong these lines are is determined mostly by the temperature of the star. The temperature will impact if the atom is ionized or the electron(s) of the atom are excited to a higher energy level as well as determine which energy levels are primarily inhabited. The combination of excited and ionized atoms determine which spectral lines are stronger and more prevalent than others within the stellar spectrum.

To obtain the amount (or abundance) of each element, modeling is needed. A model stellar atmosphere is created using the fundamental parameters of the star (e.g., effective

temperature; T_{eff}, surface gravity; $\log g$, etc.). This model is then used to determine the number of atoms needed to generate the correct depth and width of a spectral line being considered. These elemental abundances are extremely large and are normally expressed in a ratio of logs. In particular, when reporting the overall metallicity of a star, it is common to report the Fe-to-H abundance, is defined as:

$$[Fe/H] \equiv \log_{10}\left(\frac{N_{Fe}}{N_H}\right)_* - \log_{10}\left(\frac{N_{Fe}}{N_H}\right)_\odot$$

where the zero point is based on the Sun (denoted $\odot$; e.g., an $[Fe/H] = 0$ means the observed star has the same metallicity as the Sun). In the case of large-scale spectroscopic surveys, they typically use a multidimensional grid for each star. This process identifies a best fit stellar atmosphere model with a chi-squared goodness-of-fit test. A more detailed discussion is in §2.1.1.

1.1.3 Surface Abundance Variations

It is normally assumed that the observed stellar surface abundances is relatively constant and is equivalent to the bulk abundance of the star. This is not always the case. Stars can have changes in their surface abundance based on internal processes (e.g., stellar mixing Shetrone et al. 2019) and external processes (e.g., interacting binaries Bufanda et al. 2023). For this section, the focus will be on internal processes, but it well known that stars interacting with another celestial body can induce surface abundance variations.

Canonical mixing in standard stellar models accounts for convection and overshoot. An example overshoot is when a convective region extends past the predicted region

based on the convective stability criterion also known as the Schwarzchild criterion. When canonical mixing is not enough to explain the variation, the term extra-mixing is introduced as a way to describe unconfirmed source of mixing that is not included in the standard stellar models. Charbonnel & Lagarde (2010) proposed a theoretical reasoning to explain extra-mixing of [Li/H], [C/H], [N/H], and C-12/C-13 after the FDU observed in metal-poor stars (Gratton et al. 2000) to be thermohaline mixing. This mixing is related to the "salt-fingers instability", where the Ledoux stability criteria are satisfied, and is dependant on the inversion of the mean molecular weight gradient which is hotter for metal-poor stars ([Fe/H] $<$ -0.5) than in metal-rich stars ([Fe/H] $\geq$ -0.5). This dependency supports the presences of extra-mixing in metal-poor stars and the lack of extra-mixing in metal-rich stars. However, this is only one method to explain extra-mixing, where another processes could be at play, and understanding the underlining physics in the stellar structures is an active field of research.

Atomic diffusion is another stellar process that affects stars at the main sequence turnoff (MSTO) and on the SGB, which has been theorized for over a century to operate in stars (Chapman 1917b;a). This process is a combination of gravitational settling causing elements to sink below the surface and radiative levitation working against it thus changing the surface abundance of the star. Over time, the surface abundance no longer reflects the star's birth abundance or average abundance, because the elements have sunk out of the convection zone and are no longer being mixed back to the star's surface where we can observe. Once a star's convective envelope starts to deepen on the RGB, new elements that have diffused out are mixed back into the envelope, restoring the surface to "normal" (Michaud et al. 2015). Fortunately this phenomenon, atomic

diffusion, has been well studied (Michaud et al. 2015, and citations therein) and has been observed in the globular clusters: M 92 (Boesgaard et al. 1998, King et al. 1998), NGC 6397 (Korn et al. 2006; 2007), and NGC 6752 (Gruyters et al. 2013; 2014). More recently, there have also been observations of atomic diffusion in the globular cluster M 4 (Nordlander et al. 2024) and in the open clusters: M 67 (Souto et al. 2019; 2018, Liu et al. 2019, Bertelli Motta et al. 2018, Gao et al. 2018, Önehag et al. 2014), NGC 2420 (Semenova et al. 2020), and Coma Berenices (Souto et al. 2021).

1.1.4 Large-Area Stellar Abundances Surveys

Large-scale, high-resolution spectroscopic surveys are required for us to reliably explore detailed stellar abundance variations across the Galaxy. Here, we present large-scale, high-resolution surveys that are currently available to the astronomical community.

The European Space Agency (ESA) revolutionized the astronomy field by launching *Gaia*. This telescope is undergoing a space-based all-sky astrometric and photometric survey that probes extensive regions of the Galactic disk and provides reliable distances for over a billion stars. Hundreds of star clusters were discovered (Gaia Collaboration et al. 2018, Cantat-Gaudin et al. 2018) after the second data release of Gaia, and both membership and fundamental parameter estimates (distance, age) were improved for over 1800 clusters observed (Cantat-Gaudin et al. 2020).

The GALactic Archaeology with HERMES (GALAH) survey is a large scale and high-resolution ($R \simeq 28,000$) observational project that provides spectra from the High Efficiency and Resolution Multi-Element Spectrograph (HERMES) at the Anglo-Australian

telescope (AAT). The GALAH survey has high quality spectroscopic data and is able to measure up to 29 elemental abundances. In a study by Bouma et al. (2021), the authors used lithium depletion dating as one of their techniques to assess cluster membership in the open cluster NGC 2516, and found this method to have considerable uncertainty due to potential K dwarfs that are rapidly rotating, and hence showing elevated lithium abundances. Additionally, GALAH has been observing a large number of MSTO and SGB stars for the purpose of measuring stellar ages for these stars to study for Galactic archaeology.

Gaia-ESO is a ground-based survey established before the launch of Gaia and is used to compliment the astrometry and photometry of the space mission by creating benchmark stars to calibrate Gaia observations. This survey is a large publicly available spectroscopic survey that provides high-quality spectroscopic data from the Very Large Telescope (VLT) FLAMES and UVES instruments for 100,000 stars in the Galaxy, both in the field and in star clusters. Relevant to this work, the FLAMES instrument can measure over 12 elements in observed stars. For more metal-rich stars, the measured lithium abundance is used as an age indicator by the Li depletion boundary technique in open clusters (e.g. Jeffries et al. 2013, Martín et al. 2018).

The Apache Point Observatory Galactic Evolution Experiment (APOGEE), a Sloan Digital Sky Survey (SDSS) program, is a large sky, high-resolution ($R \sim 22.50$), infrared ($1.51 - 1.70\,\mu m$) survey that samples major populations in the Milky Way, which is more fully described in §3.3. APOGEE has the ability to measure over 15 elemental abundances, which specifically include abundances for carbon, nitrogen, and oxygen, key elements in the evolution of higher mass stars. Actually, the ratio of [C/N] has been

found to correlate with age in evolved stars that have experienced dredging (Casali et al. 2019, Spoo et al. 2022).

1.1.5 Star Clusters

A star cluster is a gravitationally bound group of stars that all formed from the same giant gas cloud. Since the whole cluster is formed from one giant gas cloud, the stars within the cluster all form with essentially identical elemental abundances and kinematic properties. Due to the stars possessing similar properties, astronomers can use these properties to infer information about the age of a cluster and the stellar populations within them by creating a Hertzsprung-Russel diagram (HRD), Kiel diagram (T_{eff} vs. $logg$), or a Color-Magnitude diagram (CMD), shown in Figure 1.1. Star clusters are useful because they provided the first data to constrain models and study stellar evolution, as well as, can be useful probes for age-dating parts of our Galaxy. Star clusters fall into two types: open clusters and globular clusters.

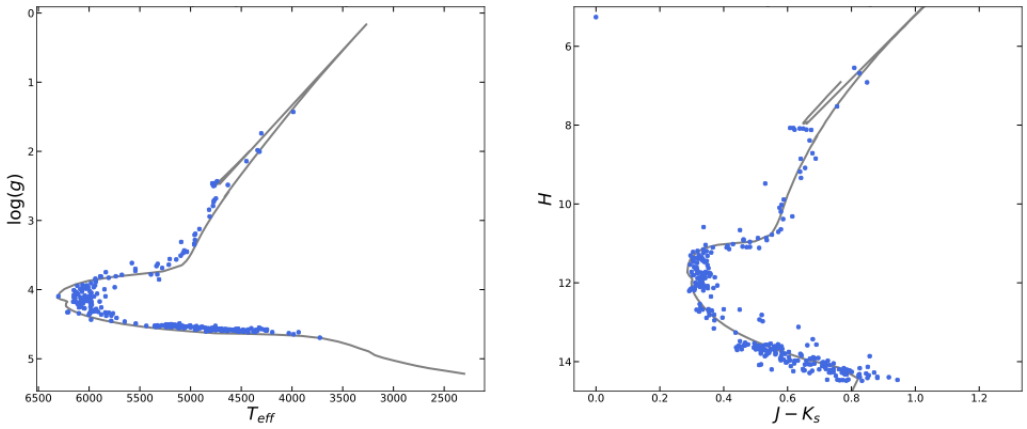

Figure 1.1: *(left)* An example of an Kiel Diagram (T_{eff} vs. $logg$). *(right)* An example of a CMD.

Open clusters are typically smaller containing anywhere from a few dozen stars to a

few ten-thousands of stars and are typically not very densely packed, hence the name "open", but are gravitationally bound. These clusters are "young" (less than 10 Gyr) and metal-rich ($-0.5 <$ [Fe/H] $< +0.4$ dex). Also, they generally live in the disk of our Galaxy and are sometimes called disk clusters.

Globular clusters are typically larger, containing several thousand to around millions of stars that live within a densely packed spherical, gravitationally-bound system. These clusters are considered stellar "dinosaurs" as they survived for billions of years, with some clusters approaching the age of the Universe. The metallicity of these clusters are considered to be metal-poor ($-2.5 <$ [Fe/H] < -0.7 dex). They are mostly associated with the bulge and halo, or inner-most and outer-most parts of the Milky Way, but they do live throughout our Galaxy.

1.2 Motivation & Age Determination Methods

To understand how the Milky Way formed and evolved, we need to be able to age-date a large number of stars covering a wide range of ages and chemistry. To do this, we need to be able to determine the ages of "field" stars, non-cluster member stars. However, stellar ages are difficult to measure accurately outside of clusters. A common method to determine stellar ages is to compare key parameters, whether directly observed (e.g., colors and apparent magnitudes, the latter combined with parallaxes) or directly inferred (e.g., $\log g$, $T_{\rm eff}$), to stellar evolution models which allow accurate relative aging of stars, but is complicated due to degeneracies in these parameters caused by chemical differences.

As large-scale surveys are completed, astronomers are able to further investigate

Galactic evolution, both kinematically and chemically. Surveys that use high-resolution spectroscopic data can provide chemical abundances for various elements in stellar populations including clusters. These elemental abundances can be used to further constrain stellar ages using key diagnostics, such as [C/N] abundances and Li-depletion. Since the ESA *Gaia* survey can provide accurate parallaxes, and thus distances, this opens an opportunity to use subgiants in the field as age-probes. Combining spectroscopic surveys with high-precision photometry to measure small fluctuations, stellar masses, and hence ages, can be determined asteroseismically. With all these large-sky surveys available and becoming available, arises a new and exciting era of Galactic archaeology.

1.2.1 Cluster Ages

We can create stellar models that provide astronomers with relative, and hopefully, absolute, ages for stars since stellar evolution is derived from star clusters. The age of cluster can be determined by measuring the position of the main sequence turnoff (MSTO) or the strength of the SGB. Since clusters contain stars that all formed at the same time and higher-mass stars evolve faster than lower-mass stars, the difference in mass creates noticeable variations in the HRD or CMD. Specifically as the cluster gets older, stars of lower masses transition from MS to the RGB, and the MSTO will "move down" the MS, becoming dimmer and cooler, as shown in Figure 1.2. Hence, star clusters have been used as the primary source for reliable age indicators.

1.2.2 Sub-giant Branch Location Ages

An interesting age indicator is the location of the sub-giant branch, as stars with masses less than 2-2.5$M_{\odot}$ that have longer enough evolutionary time scales to allow the sub-giant branch to form. As stellar ages increase the sub-giant branch stars will have a lower luminosity similar to the age variation of MSTO.

Since *Gaia* released precise parallaxes, and therefore good distances, allowing reliable absolute magnitude determining is possible for a large number of stars, in particularly sub-giants. These stars can then be compared to isochrones as the sub-giant branches runs parallel to each other over time as it grows fainter, see Figure 1.3. This method has allure as sub-giants are relatively bright so they can be used as a deeper probe without

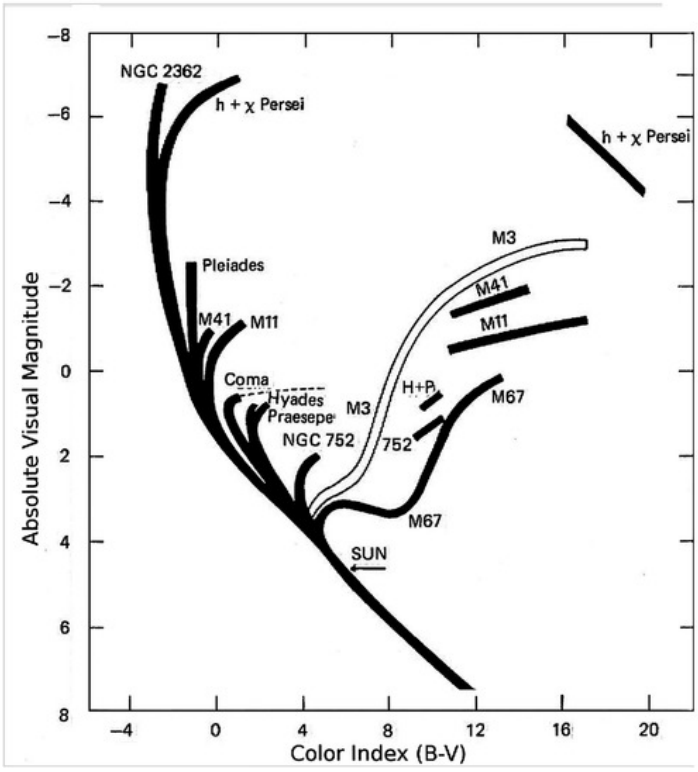

Figure 1.2: Figure 1 of Sandage (1957). The CMD is comprised of multiple stars clusters, with varied ages, mapped over top each other. This shows how the MSTO will "move down" the MS with age.

using too much time, but stellar evolution might leave this method at a disadvantage, see Chapter 3.

1.2.3 Chemical Clocks

As more large-scale spectroscopic surveys, such as APOGEE, Gaia-ESO, GALAH, become more available, a promising method for determining reliable ages for field stars is using "chemical clocks". While astronomers have long identified that most elemental abundances increase with time due to supernovae enrichment, e.g., iron, a true chemical clock is an elemental abundance, or abundance ratio, that *closely* correlates with age, preferably independent of the stars overall "metallicity". Recent large-scale spectroscopic surveys, which provide a large number of chemical abundances measurements for hundreds of thousands of stars, make it more feasible to apply "chemical clocks" for a large

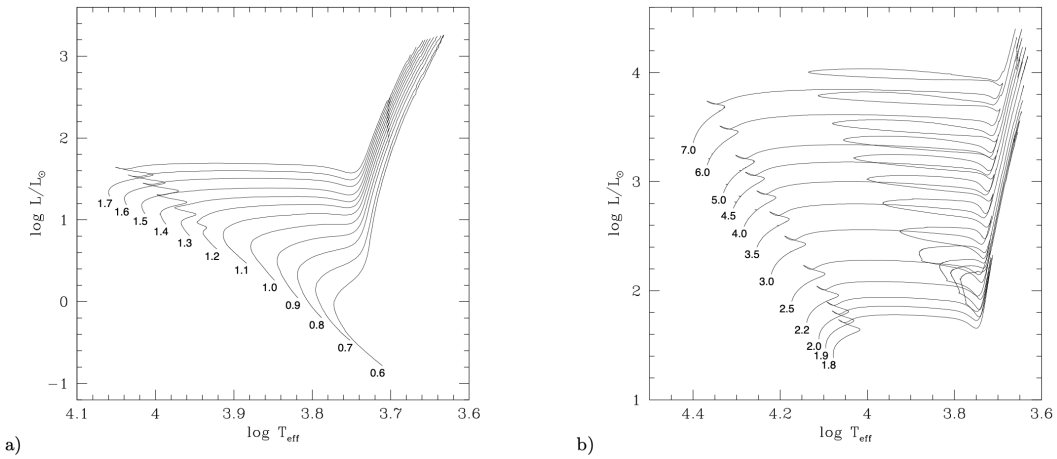

Figure 1.3: Figure 2 panels a and b of Girardi et al. (2000). The HRD is comprised of multiple isochrones as a function of mass. The stellar mass (in $M_{\odot}$) is indicated at the initial point of the evolution. This shows as the mass is decreased (and the age increases) the strength of the SBG decreases. Notice as well how the SGB runs almost parallel to each other with age.

number of stars within the MW, as doing spectroscopic observations are normally time-expensive. Of the potential "chemical clocks" available, astronomers have significant work with calibrating three: Li-depletion, [s-process/α], and [C/N].

1.2.3.1 Li-Depletion

When the Big Bang occurred, trace amounts of lithium were created alongside hydrogen and helium, constrained by the results of big bang nucleosysthesis. Unlike most elements lighter than iron, lithium is easily nuclear burned within a star and not formed, so what trace the amount of lithium that is left after being processed can indicate the age of the star. The less lithium the star has the older the star should be. This relationship has been shown in many studies (Jeffries et al. 2013, Martín et al. 2018, Bouma et al. 2021) to age stars within open clusters. *This method only works for stars in their main sequence stage*, as once the star evolves to its red-giant phase the first dredge-up and other mixing events will burn the remaining lithium on the surface, thereby breaking the relationship between the lithium and the star's age. This restricts the method to only main sequence stars which are fainter, and therefore not ideal targets for large-scale surveys with limited observational time.

1.2.3.2 s-Process to Alpha Element Abundances

Due to how elements build overtime, different element abundance groups within the star will be different depending on age. Elements referred to as s-process elements are those formed through a process called "slow" neutron capture. This nucleosynthesis process happens with lower neutron density and intermediate stellar temperatures. Under these

conditions, the rate of acquiring neutrons is slower than the rate of radioactive decay to a more stable isotope. Elements that are referred to as alpha elements (α) are those that are integer multiples of an alpha particle, two protons and two neutrons that comprise the nucleus of a helium atom, that are produced in high-mass star nucleosynthesis, which include the elements: O, Ne, Mg, Si, S, Ar, Ca, and Ti.

When observing younger stars, s-process elements will increase, while the alpha elements will decrease. Using the right combination of elements from these two subcategories can lead to a relationship with age. For example, Viscasillas Vázquez et al. (2022) found [Ba/α] ratios are more sensitive to age than [Y/α] ratios, where specifically ratio of [Ba/Al] was able to reproduce ages for individual stars within open clusters in their sample. This method can be utilized on both dwarf and giant stars which would be ideal for large scale surveys.

While this is fascinating, this particular chemical clock is still an on going field of research where the applications and limitations are not yet fully understood. For example, [s-process/α] chemical clocks have been shown by Casali et al. (2020) to have yield variation, which affects inferred ages of stars in the inner Galaxy. Additionally, the [s-process/α] method requires a large signal-to-noise (S/N) to reliable measure s-process elements effectively which requires more observational time. Due to the combination of being time expensive and the uncertainty of which [s-process/α] is best for large portion of the Galaxy makes this chemical clock less ideal as an age-probe at this time.

1.2.3.3 Carbon-to-Nitrogen ([C/N]) Element Abundances

During the main sequence evolutionary stage, stars burn hydrogen into helium in their core in two main ways: proton-proton chains or the CNO cycle. Stars with the CNO cycle have carbon (C), nitrogen (N), and oxygen (O) as catalysts to fuse hydrogen to helium. When the stars reach the end of their hydrogen fuel the star will begin to evolve into its red giant phase. During this transition, convective envelopes of the outer regions of the star will penetrate deeper into the star's core where the previously processed C and N are dredged to the surface where it can now be observed. When these envelopes reach maximum penetration depth this is called the first dredge up (FDU). The max depth is determined by the mass of that star and from the stellar theory we know the mass and stellar age are closely related, hence the ratio of C and N ([C/N]) observed in the surface can be used to determine age. This chemical clock is applicable to evolve red giants and has been empirically shown in previous studies, such as Casali et al. (2019) and Spoo et al. (2022). Being able to use RGB stars is ideal for large-scale surveys as they are bright and can be observed for less time than MS stars.

1.2.4 Asteroseismic Ages

A relatively recent method that is highly regarded, is using asteroseimology to determine stellar ages. Asterosiemic ages use a combination of spectroscopic and high-precision photometry to measure frequency modes in stars that are dependant on the structure, and therefore mass of the star. As mass correlates to age for stars, one can derive ages for stars using astroseismic photometric measurements from NASA missions like *Kepler*

and *TESS*.

Examples of current available astroseismic surveys are APOKASC (Pinsonneault et al. 2018, Pinsonneault et al. *in prep.*) and APO-K2 (Schonhut-Stasik et al. 2024), which combine data from the spectroscopic SDSS/APOGEE survey and the photometry from the NASA *Kepler* and *Kepler-2* missions, respectively. The amount of stars within these surveys are not sufficient enough to apply to full scale of the Galaxy as they are limited to certain regions observed by *Kepler* as shown in Figure 1.4.

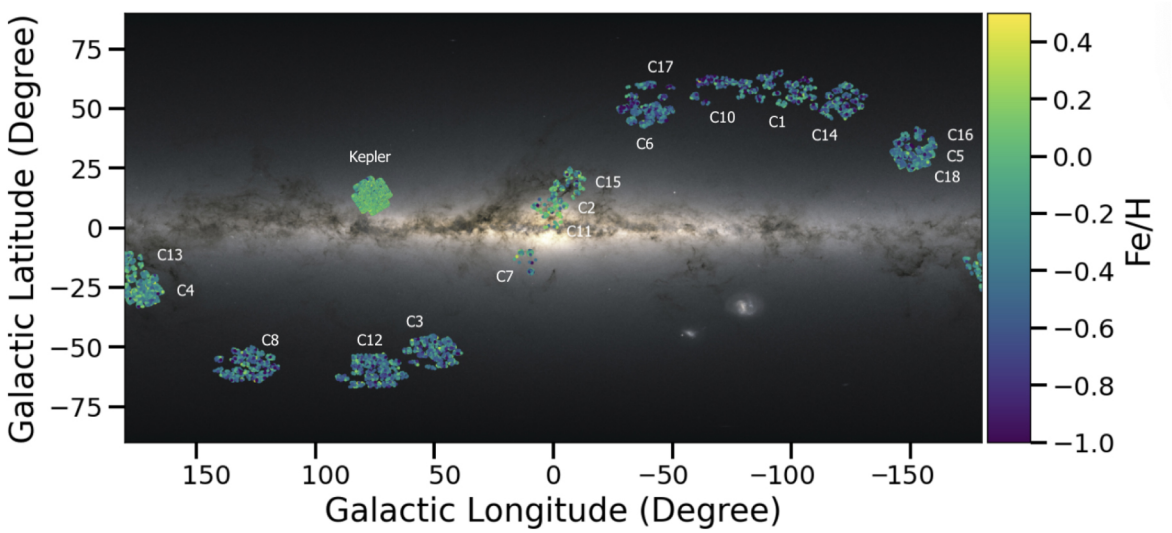

Figure 1.4: Figure 6 of Schonhut-Stasik et al. (2024). A Galactic observation map of the NASA *Kepler* and *K2* missions. The singular Kepler observation field is label as *Kepler*. The *K2* mission observation fields are labeled with a 'C' and number following an S-like curve.

1.3 Scientific Question

In Galactic archeology, astronomers want to understand how the Milky Way formed and evolved. To be able to "time-stamp" events in chronological order, we need a reliable method to age-date large numbers of stars. Currently, the most reliable method is ages

from star clusters, but clusters are limited in location and number.

A useful tool to expand age-dating capabilities is chemical clocks: chemical abundances that are linked to stellar ages. Currently, the [C/N]-Age relationship from Spoo et al. (2022) is restricted to the metal-rich disk of the Galaxy. This is only a one portion of our Galaxy and for us to gain better insight into the full picture of the Milky Way's evolution, we need to be able to probe older and more metal-poor regions. Which raises the question: *can we use the older, more metal-poor globular clusters to expand our relationship further?*

While these chemical changes help us to estimate ages on the RGB, chemical changes can also hinder age estimations in other parts of the HRD. On the MS, MSTO, and SGB, the surface abundances of a star changes from a combination of gravitational settling and radiative levitation working against it, a process known as atomic diffusion. In this case, the surface abundance is not an accurate prediction of the bulk abundances that determine the stellar age. Recent studies suggest that this effect is not negligible, and in fact the ages derived from isochrones can be overestimated by 10-20% if atomic diffusion is not accounted for (Dotter et al. 2017). Therefore, as we look for other methods to use on field stars as age-probes for the Galaxy, *are there going to be evolutionary complications we need to account for?*

Chapter 2

[C/N]-Age Calibration Extension for Metal-Poor Stars

2.1 SDSS/APOGEE Survey

The study makes use of the Apache Point Observatory Galactic Evolution Experiment surveys (APOGEE-1 & -2; Majewski et al. 2017, Majewski et al., *in prep*) which were part of the Sloan Digital Sky Survey III & IV (Eisenstein et al. 2011, Blanton et al. 2017). Data was taken with the 2.5-m Sloan Foundation Telescope (Gunn et al. 2006) at the Apache Point Observatory and the 2.5-m du Pont telescope (Bowen & Vaughan 1973) at the Las Campanas Observatory, using the APOGEE North and South spectrographs (Wilson et al. 2019), conducted between May 2011 and January 2021. APOGEE Target selection is described in Zasowski et al. (2013; 2017), Beaton et al. (2021), and Santana et al. (2021), with open cluster targeting also detailed in Frinchaboy et al. (2013) and

Donor et al. (2018).

The data used in this study uses the APOGEE reduction pipeline (Nidever et al. 2015) and the Stellar Parameters and Chemical Abundances Pipeline (ASPCAP; García Pérez et al. 2016), which employ the Stellar Atmosphere Models (Mészáros et al. 2012), Stellar Spectral Libraries (Zamora et al. 2015), and the APOGEE line-list (Shetrone et al. 2015). The APOGEE Stellar Parameters and Chemical Abundances Pipeline (ASPCAP; García Pérez et al. 2016) reports stellar parameters and chemical abundances for 20+ elements, including carbon and nitrogen, that are difficult to measure in optical spectra. APOGEE is uniquely suited for this project because this survey reliably measures C, N, and O abundances, allowing accurate [C/N] ratios to be calculated.

2.1.1 SDSS/APOGEE Survey DR17

In this work, we use the final data release of the APOGEE-2 survey available from SDSS-IV Data Release (DR17; Abdurro'uf et al. 2022), including all APOGEE observations from August 2011 to January 2021 and has $\sim 734,000$ stars. A full description of data quality and parameter limitations for the APOGEE DR17 is described in Abdurro'uf et al. (2022) and Holtzman et al., *in prep.* The primary release for APOGEE DR17 has changed the ASPCAP analysis code compared to previous data releases, because the library of synthetic spectra was calculated using Synspec code, which allows for non-local thermodynamic equilibrium (NLTE) line formation while assuming a plane parallel geometry, which becomes less valid for the largest giant stars. Where all previous APOGEE data releases used the Turbospectrom code (Plez 2012) which assumes

spherical geometry, but does not account for NLTE affected elements.

2.1.2 APOGEE-RC Catalog

This work uses data to verify red clump stars using the APOGEE-RC catalog (Bovy et al. 2014, Bovy et al., *in prep*) based on the APOGEE survey. The APOGEE RC catalog includes $\sim 51,000$ likely RC stars, determined by the stellar position in color-metallicity–surface-gravity–effective-temperature space based on a method calibrated using stellar evolution models and asteroseismology data. Because RC stars are nearly constant in luminosity, they can be used as standard candles and the APOGEE-RC catalog has been used for numerous studies of the Milky Way (e.g., Nidever et al. 2014, Hayden et al. 2015, Loebman et al. 2016). For this work, we utilize the ability to isolate stars in the RGB and RC evolutionary states.

2.1.3 Price-Whelan et al. (2020) Catalog

This work uses data as additional verification if stars are in close binary systems using the Price-Whelan et al. (2020) value added catalog (VAC) based on the APOGEE survey. This catalog includes 232,495 sources, determined by their custom Monte Carlo sampler called The Joker through radial velocities. Stars within a binary system can interact with each other, which can cause the surface abundance to change. For this work, we utilize this ability to flag stars that are binaries, as these binary systems may be determined to be older than the Universe through [C/N]-Age relationship.

2.1.4 Patton et al. (2024) Catalog

This work uses data the Patton et al. (2024) catalog based on the APOGEE survey to verify rapidly rotating giants. This catalog includes 3217 active red giant candidates, determined by using a control sample of well-studied Kepler fields to establish a relationship between rotation and anomalies in the spectroscopic solution compared to a typical giant. (Typical giants should have near zero rotation due to conservation of angular momentum when the star "puffs out" during stellar evolution.) With this relationship, Patton et al. (2024) found stars within the APOGEE survey with similar solutions to be considered candidates than the *vsini* measurements we use to confirm. For this work, we utilize this ability to flag stars that are rapidly rotating for stars that may be determined to be older than the Universe through [C/N]-Age relationship. Having this flag gives an explanation for such large determined ages, because (1) this is a sign the star has interacted with another object which could have changed the surface abundance, or (2) have wider lines due to rotation, which would affect the determined abundance values from the APOGEE pipeline, since the pipeline assumes giants do not rotate due to conservation of angular momentum.

2.2 The ESA *Gaia* Survey

The ESA *Gaia* mission is a space-based all-sky astrometric and photometric survey that probes extensive regions of the Galactic disk. Hundreds of star clusters were discovered (Gaia Collaboration et al. 2018, Cantat-Gaudin et al. 2018) after the second data release of Gaia, and both membership and fundamental parameter estimates (distance, age)

were improved for over 1800 clusters observed (Cantat-Gaudin et al. 2020). Gaia (EDR3; Riello et al. 2021) was released on 3 December 2020. Gaia Data Release 3 (Gaia DR3) was released on 13 June 2022.

2.2.1 The Cantat-Gaudin et al. (2020) Catalog

Cantat-Gaudin et al. (2020) used the *Gaia* DR2 catalog of $\sim$ 1.3 billion stars with proper motions, parallaxes, and deep homogeneous photometric data to provide one of the first precision all-sky analysis of open clusters in the Milky Way. The data is then used in their artificial neural network to estimate age, distance, and interstellar reddening for about 230,000 stars in 2017 star clusters.

2.3 The ACS Survey of Galactic Globular Clusters

We have used the ACS Survey of Galactic globular clusters (Wagner-Kaiser et al. 2017) to provide ages for our globular cluster sample in this work. This survey is comprised of 69 clusters and uses data from Hubble Space telescope imaging for the ACS Treasury Survey to determine single population isochrones. The fits use robust Bayesian analysis techniques to measure absorptions, ages, distances, and He-values for each cluster.

2.4 Analysis

To obtain a more complete picture of the older part of the Milky Way (e.g., bulge, streams, and halo) through the chemical clock [C/N], we need to expand our calibration sample to

include the older and more metal poor stars where good ages can be derived, i.e., globular clusters. Since globular clusters are among the oldest objects in our Universe, they provide a snapshot into the early stages of our Milky Way. However, stepping forward with utilizing globular clusters in our calibration introduces an added layer of complexity due to their cluster characteristics such as low metal content and many having multiple populations of stars, plus lower-mass stars can have additional evolutionary chemical changes.

In Shetrone et al. (2019), it was found that stars more metal poor than $[Fe/H] \approx -0.5$ will experience extra-mixing along the RGB; this extra-mixing can be significant enough that the link between [C/N] and age may change. To exclude the effects of extra-mixing, additional cuts must be made in surface gravity to select stars that have experienced the first dredge up (FDU) but have not undergone any further extra mixing. This extra mixing happens to occur near the red bump phase (Fraser et al. 2022, Tayar & Joyce 2022) and hence, the surface gravity cuts would be right before this evolutionary phase.

Unlike open clusters, many globular clusters have more than one population of stars (e.g., Milone & Marino 2022, and references therein), and therefore we need to be able to separate the two populations. The first population of stars will have similar chemical compositions as the Galactic-field stars with analogous metallicity, while second populations possess peculiar abundances in some light-elements when compared to field stars due to the unique enrichment history of the cluster. The elemental abundance variation is found in both RGB stars and MS stars implying the chemical variation is not due to stellar evolution (Milone & Marino 2022). For light elements such as C, N, O, and Na, second population stars will be enhanced with N and Na while depleted in C and O when

compared to the first population. These elements have well-defined relationships such as the Na-N and C-O correlations and Na-O and C-N anti-correlations found as a prevalent feature across globular clusters with multiple populations. Another relationship found in a majority of globular clusters is a correlation between [Al/Fe] and [Na/Fe]. Since these (anti)correlations exist, we can use them to separate the first population of stars from the second population of stars within their corresponding chemical spaces.

2.4.1 Globular Cluster Member Selection

To select stars with reliable carbon and nitrogen measurements for our analysis, we followed quality cuts outlined in Table 1 of Spoo et al. (2022) for bitwise flags, and signal-to-noise ratio (SNREV). The globular clusters used in this work were selected because they were observed in the APOGEE survey, and have reliable ages from Wagner-Kaiser et al. (2017). Reliable cluster members were determined using the APOGEE membership flag (MEMBER) and from the Gaia based membership probabilities of Vasiliev & Baumgardt (2021). We only used Vasiliev & Baumgardt (2021) probabilities that were greater than 0.999. We compared this membership method with methods within Myers et al. (2022) and Schiavon et al. (2024) and found all three methods obtained the same stellar membership for all globular cluster used in this work, therefore combining the Spoo et al. (2022) sample with our globular cluster sample does not lose uniformity.

2.4.2 Calibration Sample Selection

For us to select stars that are reliable for our calibration extension, we need to obtain RGB stars from the first stellar population formed in the cluster. First, we selected RGB stars using a polynomial fit within color-magnitude space, both in Gaia and 2MASS photometry, and then we applied offsets until it clearly delineated AGB so they could be rejected, as shown in Figure 2.1. Once the RGB stars are isolated we separated the populations using known (anti)correlations in chemical space, as shown in Figures 2.2 and 2.3. Next, we removed peculiar enriched stars using [C/N] versus [C+N/Fe] plots to compare them to halo fields stars with similar [Fe/H] and [Mg/Fe], as shown in Figure 2.4. The [C/N] versus [C+N/Fe] selection ensures the selected stars in the calibration best represents the field star sample for the new relationship to be implemented on. Following these selections, we applied surface gravity cuts, from Table 2 of Shetrone et al. (2019), to remove stars that have experienced the FDU but have not undergone extra mixing, shown in Figure 2.5. After applying this criteria, our globular cluster sample summary is shown in Table 2.1 which includes: cluster names, cluster ages reported from Wagner-Kaiser et al. (2017), DR17 average [Fe/H], and DR17 average [C/N] for members stars with reliable measurements that best represent the field sample7

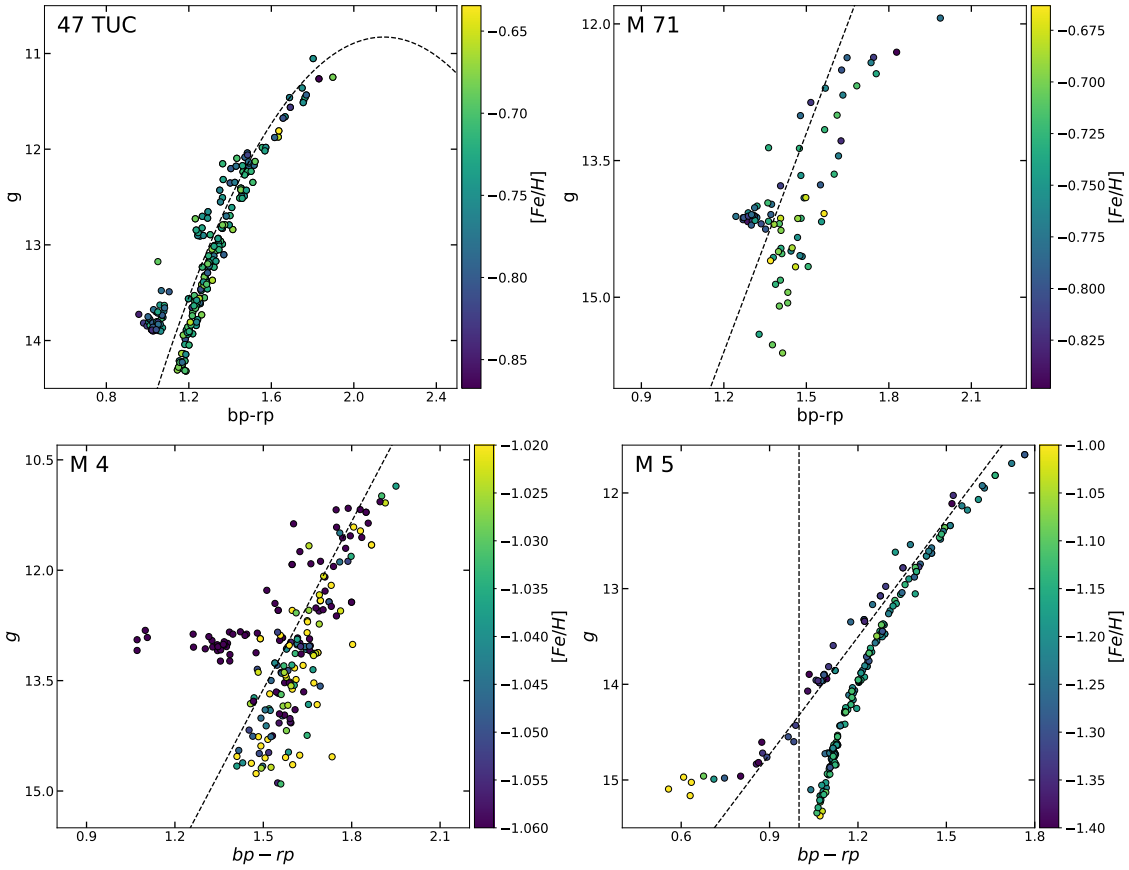

Figure 2.1: Gaia CMD for globular clusters 47 TUC, M 71, M 4, and M 5 colored by [Fe/H]. Black dashed lines represent the polynomial functions used to isolate RGB members of each cluster. Note the magnitude errors are smaller than the markers. Note the magnitude errors are smaller than the markers.

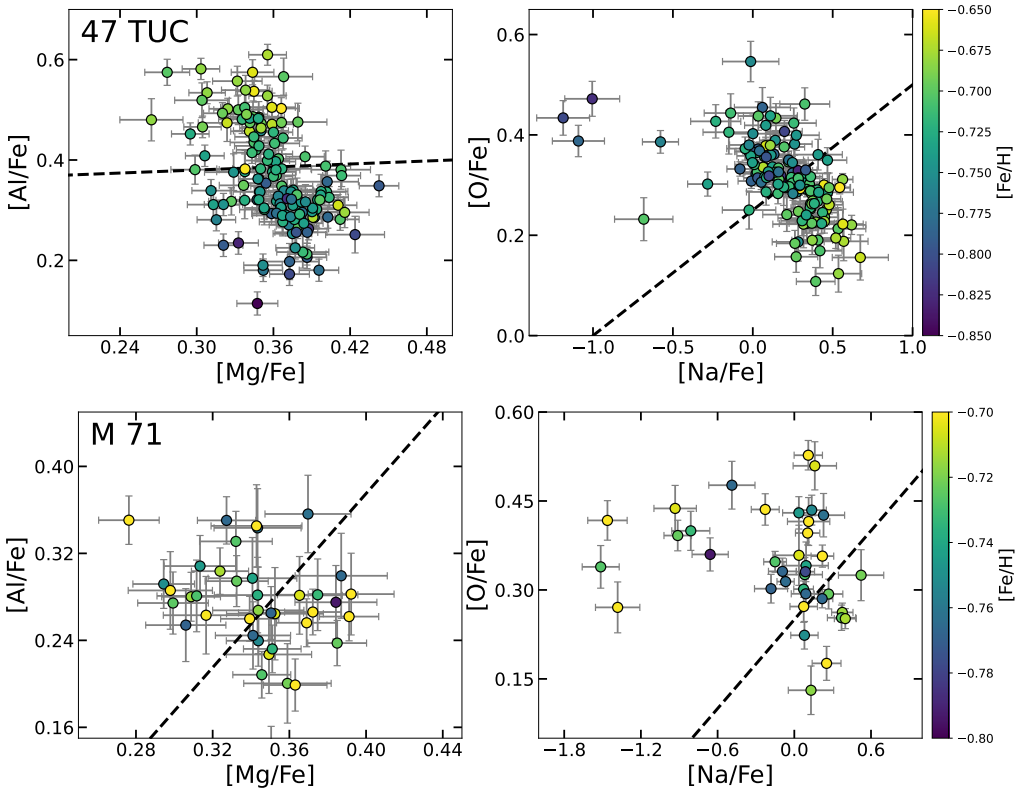

Figure 2.2: [Al/Fe]-[Mg/Fe] and [O/Fe]-[Na/Fe] (Anti)Correlation plots for globular clusters 47 TUC (*top set*) and M 71 (*bottom set*) colored by [Fe/H]. Grey dashed lines represent functions to isolate the two generations of stars within the RGB sample.

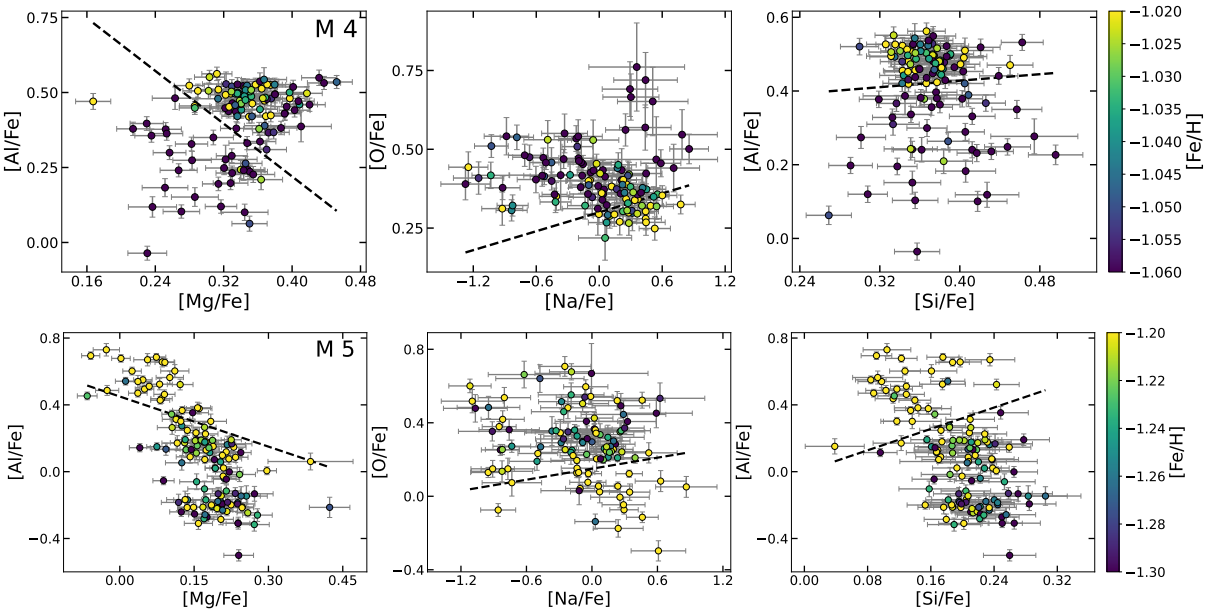

Figure 2.3: [Al/Fe]-[Mg/Fe], [O/Fe]-[Na/Fe], and [Al/Fe]-[Si/Fe] (Anti-)Correlation plots for globular clusters M 4 (*top set*) and M 5 (*bottom set*) colored by [Fe/H]. Grey dashed lines represent functions to isolate the two generations of stars within the RGB sample.

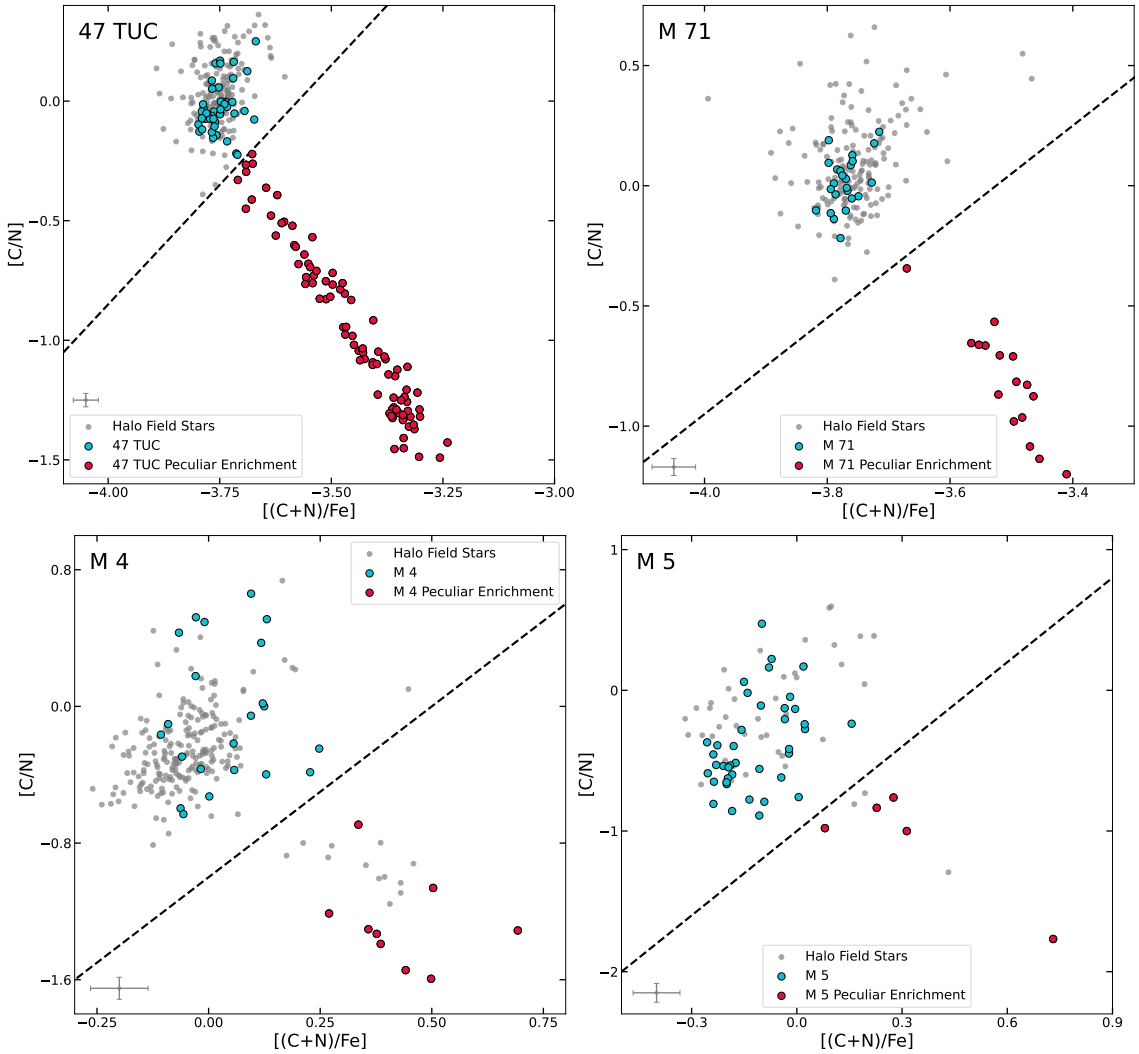

Figure 2.4: [C/N] versus [C+N/Fe] plots for globular clusters 47 TUC, M 71, M 4, and M 5. Light grey dots are halo field stars with similar Mg and Fe abundance as the cluster. Stars outlined in black are members of the respective cluster, where those color in red are considered peculiar enriched stars within the cluster while those colored in cyan are those that are not and are similar to the field. The grey dashed line represents the cut we did to remove the peculiar stars from the calibration sample. A representative error bar is shown in the lower left-hand corner for each cluster's plot.

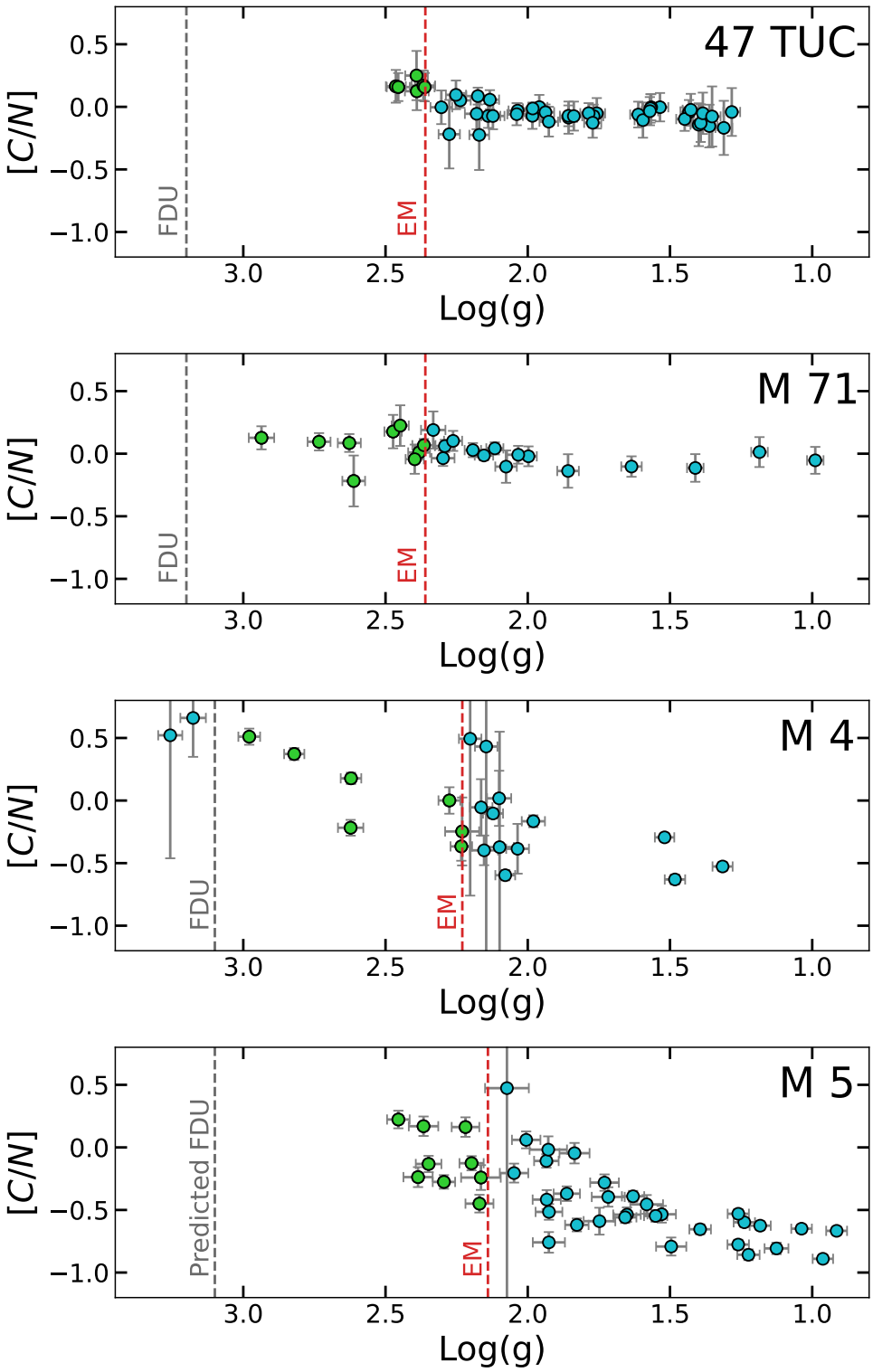

Figure 2.5: Log(g) vs [C/N] plot of first population of stars without peculiar enrichment. These are the same stars from Figure 2.4 shown in cyan. Stars used in out calibration are shown in green. The grey vertical dashed line and vertical red dashed line represent the FDU logg cut and extra-mixing (EM), respectively, from Table 2 of Shetrone et al. (2019).

Table 2.1: Cluster Sample

Cluster name	log Age[*,**] (yr)	[Fe/H] (dex)	[C/N] (dex)	DR17 Members
Globular clusters				
47 Tucanae	10.13	-0.72 ± 0.01	$+0.16 \pm 0.04$	6
M 71	10.13	-0.78 ± 0.00	$+0.09 \pm 0.04$	9
M 4	10.11	-1.04 ± 0.01	$+0.00 \pm 0.12$	7
M 5	10.08	-1.20 ± 0.01	-0.13 ± 0.07	9
Open clusters (from Spoo et al. 2022)				
Berkeley 17	9.86	-0.18 ± 0.01	-0.16 ± 0.01	8
Berkeley 18	9.64	-0.39 ± 0.01	-0.33 ± 0.01	18
Berkeley 2	8.77	-0.21 ± 0.01	-0.37 ± 0.05	6
Berkeley 21	9.33	-0.27 ± 0.01	-0.36 ± 0.01	3
Berkeley 22	9.39	-0.34 ± 0.02	-0.39 ± 0.12	5
Berkeley 29	9.49	-0.53 ± 0.01	-0.28 ± 0.01	2
Berkeley 31	9.45	-0.43 ± 0.02	-0.28 ± 0.00	2
Berkeley 53	8.99	-0.12 ± 0.01	-0.52 ± 0.02	6
Berkeley 66	9.49	-0.22 ± 0.01	-0.30 ± 0.01	5
Berkeley 71	8.94	-0.23 ± 0.00	-0.52 ± 0.03	5
Berkeley 75	9.23	-0.41 ± 0.01	-0.50 ± 0.04	3
Berkeley 85	8.62	$+0.06 \pm 0.02$	-0.42 ± 0.01	10
Berkeley 98	9.39	-0.04 ± 0.01	-0.38 ± 0.04	5
Czernik 20	9.22	-0.18 ± 0.01	-0.40 ± 0.05	4
Czernik 21	9.41	-0.33 ± 0.01	-0.28 ± 0.01	2
Czernik 30	9.46	-0.39 ± 0.00	-0.35 ± 0.02	2
ESO 211 03	9.11	-0.17 ± 0.01	-0.51 ± 0.02	15
ESO 518 03	9.15	$+0.11 \pm 0.02$	-0.45 ± 0.03	4
FSR 0494	8.95	-0.02 ± 0.01	-0.51 ± 0.01	5
FSR 0937	9.08	-0.37 ± 0.01	-0.44 ± 0.03	2
IC 1369	8.46	-0.11 ± 0.02	-0.56 ± 0.02	3
IC 166	9.12	-0.09 ± 0.01	-0.49 ± 0.04	13
King 5	9.01	-0.16 ± 0.01	-0.46 ± 0.01	4
King 7	8.35	-0.16 ± 0.02	-0.37 ± 0.07	7
Melotte 71	8.99	-0.15 ± 0.01	-0.48 ± 0.02	3
NGC 1193	9.71	-0.34 ± 0.01	-0.25 ± 0.03	3
NGC 1245	9.08	-0.09 ± 0.01	-0.48 ± 0.02	25
NGC 1798	9.22	-0.28 ± 0.01	-0.43 ± 0.02	10
NGC 1817	9.05	-0.16 ± 0.01	-0.40 ± 0.04	5
NGC 1857	8.40	-0.18 ± 0.00	-0.41 ± 0.01	2

Continued on next page

Table 2.1 – Continued

Cluster name	log Age*,** (yr)	[Fe/H] (dex)	[C/N] (dex)	DR17 Members
NGC 188	9.85	+0.06 ± 0.00	−0.24 ± 0.01	32
NGC 1907	8.77	−0.13 ± 0.00	−0.51 ± 0.05	3
NGC 1912	8.47	−0.17 ± 0.01	−0.44 ± 0.02	2
NGC 2158	9.19	−0.25 ± 0.00	−0.34 ± 0.01	41
NGC 2204	9.32	−0.28 ± 0.01	−0.42 ± 0.02	20
NGC 2243	9.64	−0.46 ± 0.01	−0.34 ± 0.04	6
NGC 2304	8.96	−0.14 ± 0.01	−0.40 ± 0.01	2
NGC 2324	8.73	−0.22 ± 0.01	−0.52 ± 0.04	4
NGC 2420	9.24	−0.20 ± 0.01	−0.34 ± 0.01	16
NGC 2447	8.76	−0.11 ± 0.01	−0.55 ± 0.02	3
NGC 2682	9.63	+0.00 ± 0.00	−0.37 ± 0.01	19
NGC 4337	9.16	+0.22 ± 0.01	−0.49 ± 0.01	6
NGC 6705	8.49	+0.10 ± 0.01	−0.44 ± 0.02	12
NGC 6791	9.80	+0.31 ± 0.01	−0.16 ± 0.01	41
NGC 6811	9.03	−0.05 ± 0.01	−0.52 ± 0.01	6
NGC 6819	9.35	+0.04 ± 0.01	−0.35 ± 0.02	42
NGC 6866	8.81	+0.01 ± 0.00	−0.56 ± 0.03	2
NGC 752	9.07	−0.06 ± 0.00	−0.44 ± 0.01	5
NGC 7789	9.19	−0.03 ± 0.00	−0.42 ± 0.01	65
Ruprecht 147	9.48	+0.12 ± 0.02	−0.40 ± 0.03	3
Ruprecht 85	8.31	−0.25 ± 0.01	−0.34 ± 0.15	2
SAI 116	8.10	+0.14 ± 0.00	−0.37 ± 0.10	2
Teutsch 12	8.92	−0.20 ± 0.01	−0.57 ± 0.03	4
Teutsch 51	8.83	−0.33 ± 0.01	−0.52 ± 0.01	3
Tombaugh 2	9.21	−0.37 ± 0.00	−0.61 ± 0.07	4
Trumpler 20	9.27	+0.11 ± 0.00	−0.51 ± 0.02	25
Trumpler 5	9.63	−0.45 ± 0.00	−0.27 ± 0.02	8

*Globular cluster ages are adopted to have 0.1 age uncertainty.
** Open cluster ages come from Cantat-Gaudin et al. (2020).

2.5 Results

After application of these additional membership and cluster age cuts the sample used for our [C/N]-age calibration (Figure 2.6) is comprised of the 49 clusters (530 stars) from

Spoo et al. (2022) plus four globular clusters: 47 TUC, M 71, M 4, and M 5 (31 stars). The full sample, presented in Appendix C, covers an age range of $8.62 \leq \log(Age[\mathrm{yr}]) \leq 10.13$ and a metallicity range of $-1.2 \leq [\mathrm{Fe/H}] \leq +0.3$. The individual globular cluster stars used in the calibration extension are shown in Table 2.2.

Table 2.2: Calibration Globular Cluster Sample Stellar Data from APOGEE DR17.

Cluster name	2MASS ID	T_{eff} (K)	log(g) (dex)	[Fe/H] (dex)	[C/N] (dex)
47 TUC	2M00204027-7201425	4753 ± 12	2.46 ± 0.04	-0.69 ± 0.01	0.16 ± 0.13
47 TUC	2M00215813-7158147	4809 ± 15	2.46 ± 0.04	-0.71 ± 0.01	0.16 ± 0.11
47 TUC	2M00231815-7211516	4814 ± 16	2.39 ± 0.04	-0.76 ± 0.01	0.13 ± 0.15
47 TUC	2M00251382-7159103	4813 ± 15	2.37 ± 0.04	-0.79 ± 0.01	0.17 ± 0.12
47 TUC	2M00233065-7150017	4756 ± 12	2.36 ± 0.03	-0.70 ± 0.01	0.16 ± 0.11
47 TUC	2M00235608-7141488	4811 ± 15	2.39 ± 0.04	-0.75 ± 0.01	0.25 ± 0.20
M 71	2M19533271+1841101	4825 ± 15	2.73 ± 0.04	-0.70 ± 0.01	0.10 ± 0.07
M 71	2M19533114+1845204	4858 ± 16	2.63 ± 0.04	-0.71 ± 0.01	0.09 ± 0.07
M 71	2M19533428+1846550	4854 ± 11	2.47 ± 0.03	-0.68 ± 0.01	0.18 ± 0.13
M 71	2M19533989+1844229	4858 ± 10	2.45 ± 0.03	-0.72 ± 0.01	0.22 ± 0.16
M 71	2M19534992+1841255	4914 ± 19	2.94 ± 0.04	-0.71 ± 0.01	0.13 ± 0.09
M 71	2M19535769+1844567	4866 ± 16	2.61 ± 0.04	-0.68 ± 0.01	-0.22 ± 0.20
M 71	2M19535018+1845525	4751 ± 13	2.38 ± 0.04	-0.73 ± 0.01	0.01 ± 0.03
M 71	2M19540228+1842447	4772 ± 15	2.37 ± 0.04	-0.76 ± 0.01	0.07 ± 0.05
M 71	2M19533593+1847564	4757 ± 10	2.40 ± 0.03	-0.75 ± 0.01	-0.04 ± 0.12
M 4	2M16223348-2631308	5050 ± 13	2.82 ± 0.04	-1.08 ± 0.01	0.37 ± 0.26
M 4	2M16225050-2642162	5291 ± 16	2.28 ± 0.04	-1.22 ± 0.01	0.00 ± 0.18
M 4	2M16231475-2645281	5063 ± 14	2.98 ± 0.04	-1.05 ± 0.01	0.51 ± 0.37
M 4	2M16232148-2638354	5272 ± 16	2.23 ± 0.04	-1.20 ± 0.01	-0.37 ± 0.27
M 4	2M16233193-2631314	5397 ± 39	2.23 ± 0.06	-1.22 ± 0.02	-0.25 ± 0.47
M 4	2M16233236-2629222	4932 ± 12	2.62 ± 0.04	-1.05 ± 0.01	0.18 ± 0.18
M 4	2M16233621-2640002	4982 ± 17	2.62 ± 0.04	-1.08 ± 0.01	-0.22 ± 0.22
M 5	2M15175206+0159462	4994 ± 14	2.45 ± 0.04	-1.21 ± 0.01	0.22 ± 0.26
M 5	2M15175554+0217164	4991 ± 17	2.35 ± 0.04	-1.12 ± 0.01	-0.13 ± 0.10
M 5	2M15181619+0205358	5001 ± 14	2.29 ± 0.04	-1.15 ± 0.01	-0.28 ± 0.23
M 5	2M15182846+0159283	4866 ± 16	2.22 ± 0.05	-1.29 ± 0.01	0.16 ± 0.22
M 5	2M15182917+0159269	4908 ± 17	2.17 ± 0.05	-1.23 ± 0.01	-0.45 ± 0.33
M 5	2M15183720+0208197	4887 ± 29	2.16 ± 0.07	-1.26 ± 0.02	-0.24 ± 0.21
M 5	2M15183873+0208200	4890 ± 14	2.20 ± 0.04	-1.16 ± 0.01	-0.13 ± 0.09
M 5	2M15183915+0205301	4940 ± 19	2.37 ± 0.05	-1.23 ± 0.01	0.17 ± 0.13
M 5	2M15183975+0212333	4992 ± 19	2.39 ± 0.05	-1.23 ± 0.01	-0.24 ± 0.35

2.5.1 The Extended DR17 [C/N] Abundance/Age Calibration

In log-log space the relationship between stellar age and [C/N] appears to follow polynomial curve; our best fit is given by:

$$\log[Age(\mathrm{yr})] = -1.83\,(\pm 0.88)\,[\mathrm{C/N}]^2 + 1.35\,(\pm 0.53)\,[\mathrm{C/N}] + 10.10\,(\pm 0.08) \quad (2.1)$$

The polynomial fit given by Equation 2.1 and shown in Figure 2.6 uses an Orthogonal Distance Regression method, from the `scipy` package ODR, to ensure errors in [C/N] and log[Age (yr)] were both equally considered in our fit. We also evaluated a linear fit and the results of that fitting can be found in Appendix A.

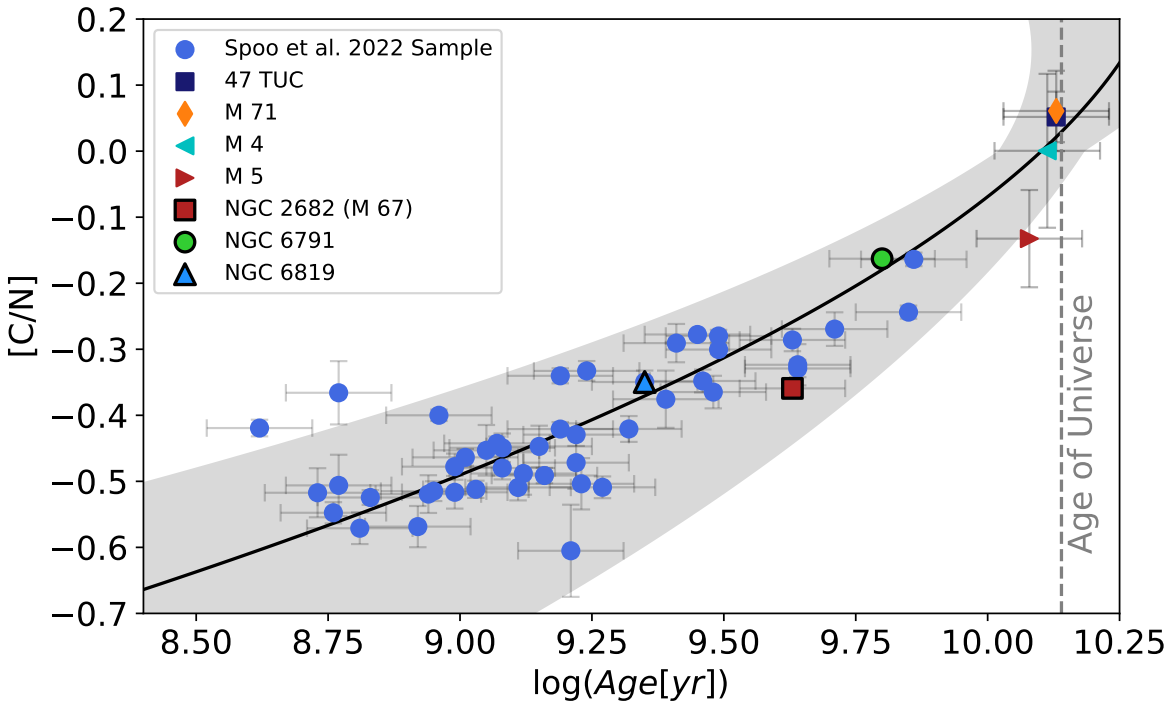

Figure 2.6: The [C/N] versus log(Age[yr]) distribution for the final sample, composed of Spoo et al. (2022) open cluster sample and globular clusters: 47 TUC, M 71, M 4, and M 5. Clusters represented by blue circles are from the final calibration sample of Spoo et al. (2022). Globular clusters 47 TUC, M 71, M 4, M 5, are represented with an indigo square, an orange thin-diamond, a cyan left-triangle, and a red right-triangle, respectively. Our new fit is shown as a solid black line, and the max possible calculated age envelope is shown with the grey region. The accepted age of the Universe is shown as a vertical grey-dashed line. The open clusters used in our asteroseismic age comparison are NGC 1817, NGC 2682 (M 67), NGC 6791, NGC 6811, and NGC 6819 and are shown in black outlined orange diamond, red square, green circle, red diamond, and blue triangle, respectively.

2.6 Comparison to Asteroseismic Ages

A natural comparison can be done to asterosiesmic-based ages from the NASA *Kepler* satellite. For this work, we have compared to the APOKASC 3 survey (Pinsonneault et al. 2018, Pinsonneault et al. *in prep.*) and the recently released APO-K2 (Schonhut-Stasik et al. 2024) survey. The APOKASC 3 survey uses a combination of APOGEE and *Kelper* data to obtain stellar ages while APOK-K2 uses a combination of APOGEE and *K2* data (Warfield et al. 2024). Warfield et al. (2024) also recalculated ages for the APOKASC2 stars with their age determining method. The following sections detail our comparison to the two surveys and our verification of our [C/N]-ages.

2.6.1 APOKASC 3

Our sample has 8671 stars in common with APOKASC3, including four open clusters (but no globular clusters). Of the four available open clusters, two open clusters were found to have reliable RGB cluster membership based on OCCAM probabilities, therefore we compare only these two clusters on a star-by-star basis.

For further verification, we apply our calibrations to open clusters that are also in the APOKASC 3 sample: NGC 6791 and NGC 6819, shown in Figure 2.7. We find that our calculated ages are consistent to the ages determined in Cantat-Gaudin et al. (2020) for all three clusters. The spread in the [C/N]-calibration ages within the cluster is due to the uncertainty of [C/N] in the individual cluster members, but such a spread is expected because our calibration is based on the average [C/N] abundance of the cluster. The representative uncertainty is shown in Figure 2.7.

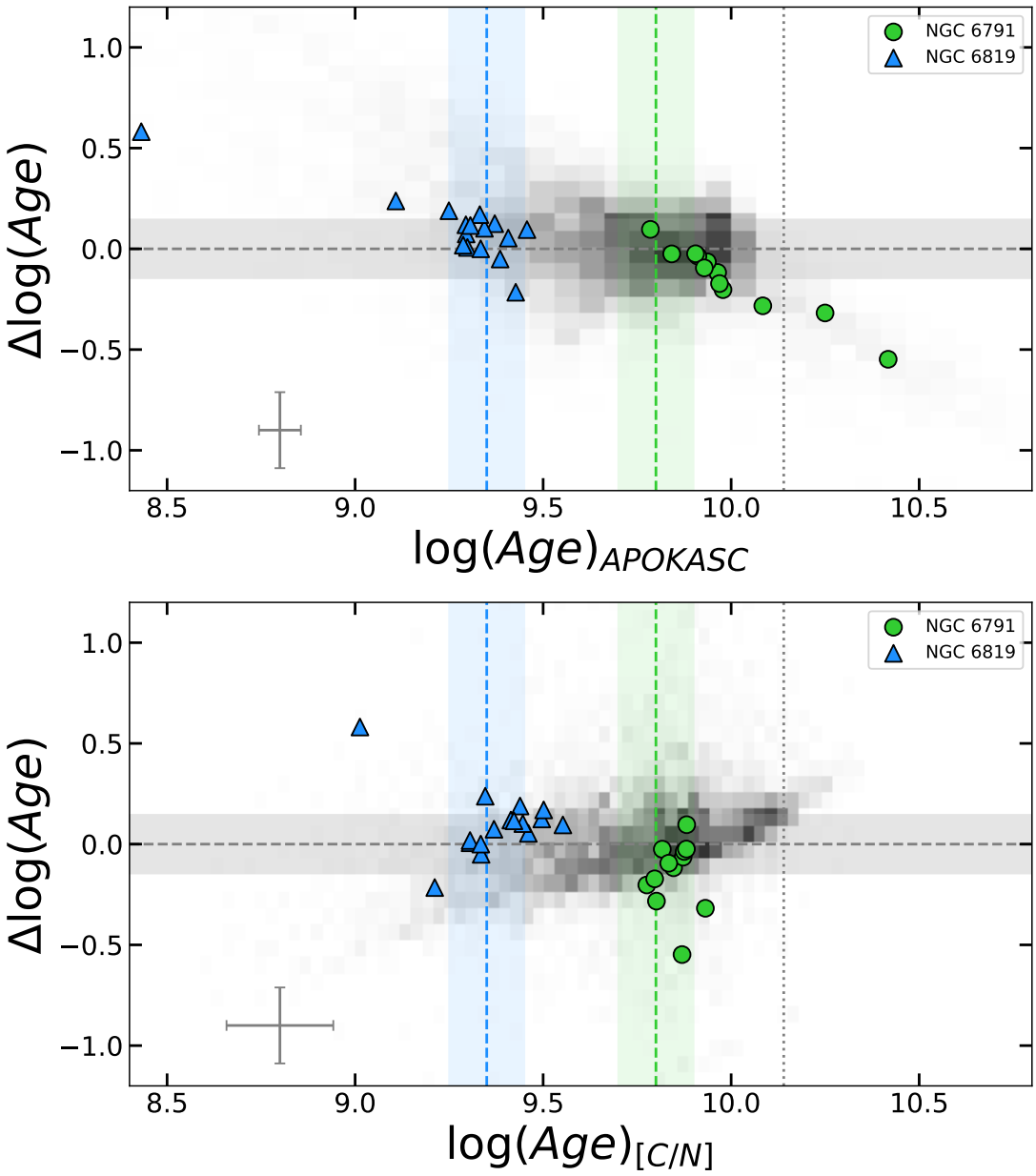

Figure 2.7: $\Delta \log[Age(yr)]$ as a function of APOKASC3 log[Age (yr)] (*top*) and [C/N]-based log[Age (yr)] (*bottom*). The grey-gradient shaded regions represent bins of field stars; darker bins imply more stars. The green circles and blue triangles represent cluster member RGB stars common to both samples NGC 6791 and NGC 6819, respectively. The vertical dashed lines are the Cantat-Gaudin et al. (2020) determined ages for each cluster and the respective shaded regions shows the error in cluster age. The horizontal grey-dashed line is where $\Delta \log[Age(yr)] = 0$ with the surrounding grey region representing a delta of -0.1 and $+0.1$. The vertical grey-dotted line shows the accepted age of the Universe. Median representative error bars are shown in each panel.

The outlier stars from NGC 6791 that are older than the Universe from asteroseismic age determination, shown with green circles that are between the vertical grey dotted line and $\log[Age(yr)] = 10.50$ in the top panel of Figure 2.7, both outlier stars are found to be in binary systems by Price-Whelan et al. (2020) while only one star is found to be rapidly rotating by Patton et al. (2024). The one found to be rapidly rotating is the green circle around $\log[Age(yr)] = 10.25$ and just to the right of the vertical grey dotted line that represents the accepted age of the Universe. Since the star is rapidly rotating, this usually indicates that mass transfer or tidal interactions has occurred, so the determined mass may not indicate age as well as potentially changing the surface abundance of carbon and nitrogen. Another thing to note for determined rapidly rotating stars, the APOGEE DR17 pipeline assumes giants are not significantly rotating and the broadening effects that are not accounted for will change the observed carbon and nitrogen abundance.

For our [C/N]-age method, we do determine some star ages that are calculated to be older than the Universe, but they only make up 1% of our sample. About a third of the "too old" stars we find to be rapidly rotating (Patton et al. 2024) and/or in a binary system (Price-Whelan et al. 2020) which can change the observed surface abundance of carbon and nitrogen (Bufanda et al. 2023), making our [C/N]-age correlation assumptions invalid for those stars. Comparison with APOKASC3 results suggests that [C/N]-based ages are consistent with asterosiesmic ages to 10% for 98.2% of all giants compared, as shown in Figure 2.7.

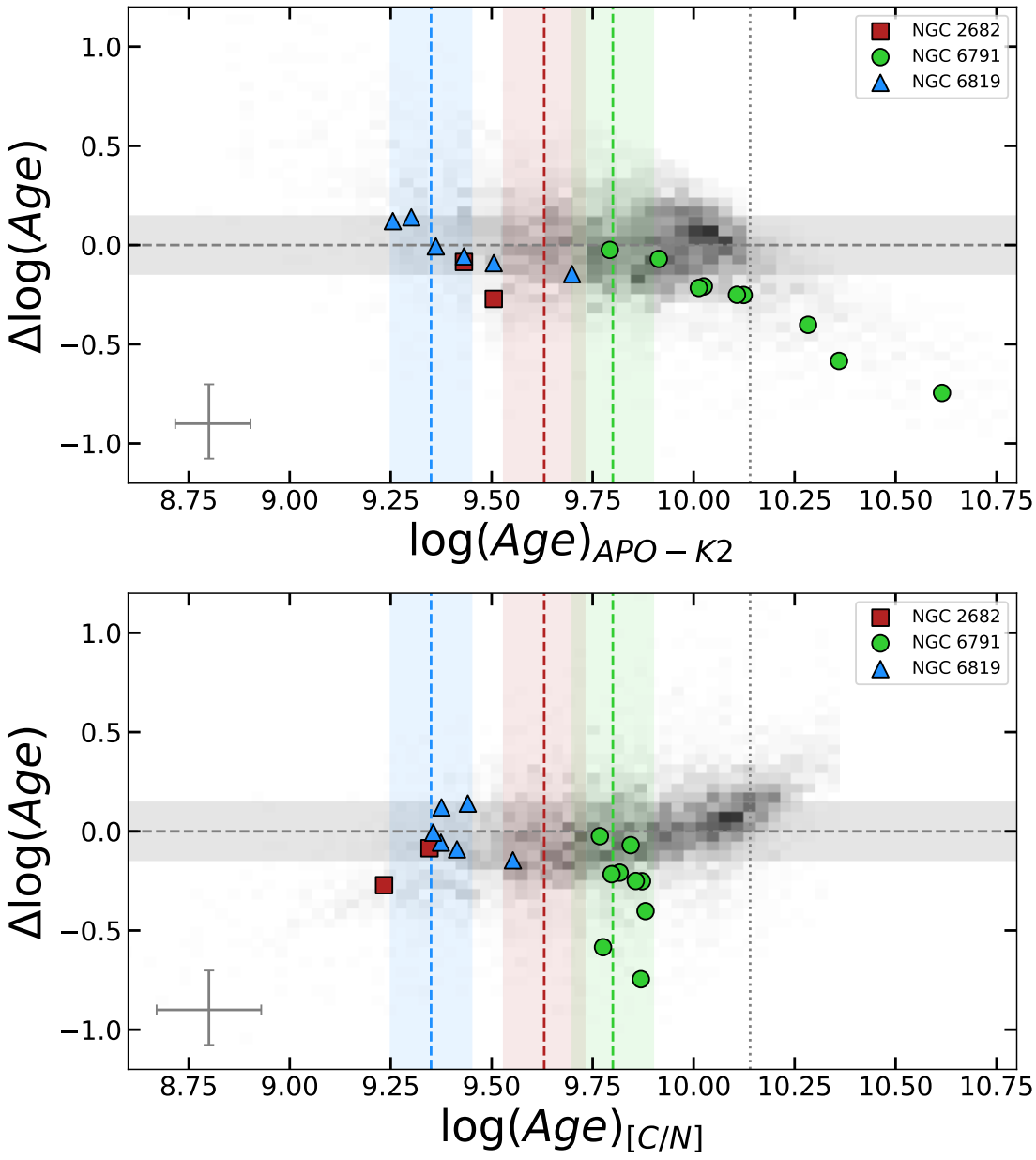

Figure 2.8: $\Delta \log[Age(yr)]$ as a function of APO-K2 log[Age (yr)] (*top*) and [C/N]-based log[Age (yr)] (*bottom*). The grey-gradient shaded regions represent bins of field stars; darker bins imply more stars. The red squares, green circles, and blue triangles represent cluster member RGB stars common to both samples NGC 2682 (M 67), NGC 6791, and NGC 6819, respectively. The vertical dashed lines are the Cantat-Gaudin et al. (2020) determined ages for each cluster and the respective shaded regions shows the error in cluster age. The horizontal grey-dashed line is where $\Delta \log[Age(yr)] = 0$ with the surrounding grey region representing a delta of -0.1 and $+0.1$. The vertical grey-dotted line shows the accepted age of the Universe. Median representative error bars are shown in each panel.

2.6.2 APO-K2

Our sample shares 7120 stars in common with APO-K2 survey, including 10 open clusters (but no globular clusters). APO-K2 combined K2 asteroseismology, APOGEE spectroscopy, and Gaia astrometry, and produced a catalog of 7672 evolved stars (either Red Giant Branch or Red Clump), that have precise asteroseismic ages, masses, radii, abundance values, and kinematic parameters. Ages for APO-K2 were derived in the second catalog release in Warfield et al. (2024). After our membership comparison, we find three open clusters where we are able to compare ages on a star-by-star basis.

For this further asteroseismic age comparison, we apply our calibrations to open clusters that are also in the APO-K2 sample, NGC 2682 (M 67) and the APO-K2 recalibrated APOKASC2 sample, NGC 6791 and NGC 6819, as shown in Figure 2.8. We find that our calculated ages are more consistent with the ages determined in Cantat-Gaudin et al. (2020) for two of the three clusters than determined with APO-K2. For both, APO-K2 and this work, the ages of stars within NGC 2682 (M 67) are under estimated relative to the Cantat-Gaudin et al. (2020) age. From Figure 2.6, the cluster NGC 2682 is further off the linear fit than the other APO-K2 cluster used in our comparison and explains why we see a discrepancy between our derived ages and the Cantat-Gaudin et al. (2020) ages used in our calibration. This discrepancy could be due to either additional effects in the APOGEE measurement of [C/N] (most NGC 2682 stars are significantly higher S/N which many reveal weaker lines) or there may be a systematic error in the isochrone fitting age determination of NGC 2682 by Cantat-Gaudin et al. (2020), similar to as is seen in Figure 6 of Hunt & Reffert (2023) where blue stragglers affect the main sequence

turn off location for older clusters from their work as well as Cantat-Gaudin et al. (2020) and Kharchenko et al. (2013).

In this comparison to APO-K2, we find that stars that are calculated to be older than the Universe now comprise 9% of our sample, where a third of those stars we find to be in a binary system (Price-Whelan et al. 2020) which could change the observed surface abundance of carbon and nitrogen (Bufanda et al. 2023). The stars determined to be "older than the Universe" as determined by the APO-K2 catalog, were checked for binarity in common proper motion (using Gaia DR3) and assessed for unresolved binaries using astrometric errors and markers (via priv. comm. regarding Schonhut-Stasik in prep.). Similarly, the spread in the [C/N]-calibration ages is due to the uncertainty of [C/N] in the individual cluster members, but such a spread is expected because our calibration is based on the average [C/N] abundance of the cluster, with representative error shown. Comparison with APO-K2 results suggests that [C/N] based ages are consistent with asterosiesmic ages to 10% for 99.6% of giants, as shown in Figure 2.8.

Chapter 3

The Effects of Atomic Diffusion on Measured Stellar Abundances

3.1 Atomic Diffusion Sample Selection

For this work, we utilized cluster membership probabilities from the Open Cluster Chemical Analysis and Mapping survey (OCCAM, Frinchaboy et al. 2013, Cunha et al. 2015, Donor et al. 2018; 2020, Myers et al. 2022). Specifically, we used OCCAM the proper motion and radial velocity membership probabilities from the Myers et al. (2022) DR17 VAC[1] to select for cluster membership. As we investigated for the potential change in abundances, we specifically did not use the metallicity-based probability. This selection ensurers we do not remove stars with potential signatures for atomic diffusion since the Fe-surface abundance would change at and around the main sequence turn off (MSTO)

[1]https://www.sdss.org/dr17/data_access/value-added-catalogs/?vac_id=open-cluster-chemical-abundances-and-mapping-catalog.

phase. The APOGEE DR17 measured surface abundance variations can be seen in Figure 3.1 for color-magnitude diagrams (CMD) of clusters NGC 752, Ruprecht 147, and M 67 with proper motion and radial velocity determined members colored by [Fe/H] and non-member stars are colored in grey.

3.2 MIST Stellar Evolution Models

In order to investigate the significance of any diffusion effects, we need to compare to stellar models. In this work, we have selected the MESA Isochrones & Stellar Tracks (MIST; Dotter 2016, Choi et al. 2016) models that utilizes the stellar evolution code Modules for experiments in Stellar Astrophysics (MESA; Paxton et al. 2011; 2013; 2015), which also included the effects of atomic diffusion. These models cover an age range of $5 \leq \ log[Age(yr)] \leq 10.3$ and metallicity range of $-4 \leq [Fe/H] \leq +0.5$ as well as report surface abundances for 19 isotopes of 17 elements from hydrogen to iron. Stellar evolutionary tracks were computed with and without radiative acceleration to gauge its influence. Each element is treated separately for ionization, monochromatic opacity, and radiative acceleration, except for titanium since there is no Opacity Project data available. Due to the lack of available data titanium is grouped with calcium as a single class. All isochrones used in this study were generated using the MIST Isochrone Interpolation tool[2].

[2]https://waps.cfa.harvard.edu/MIST/interp_isos.html

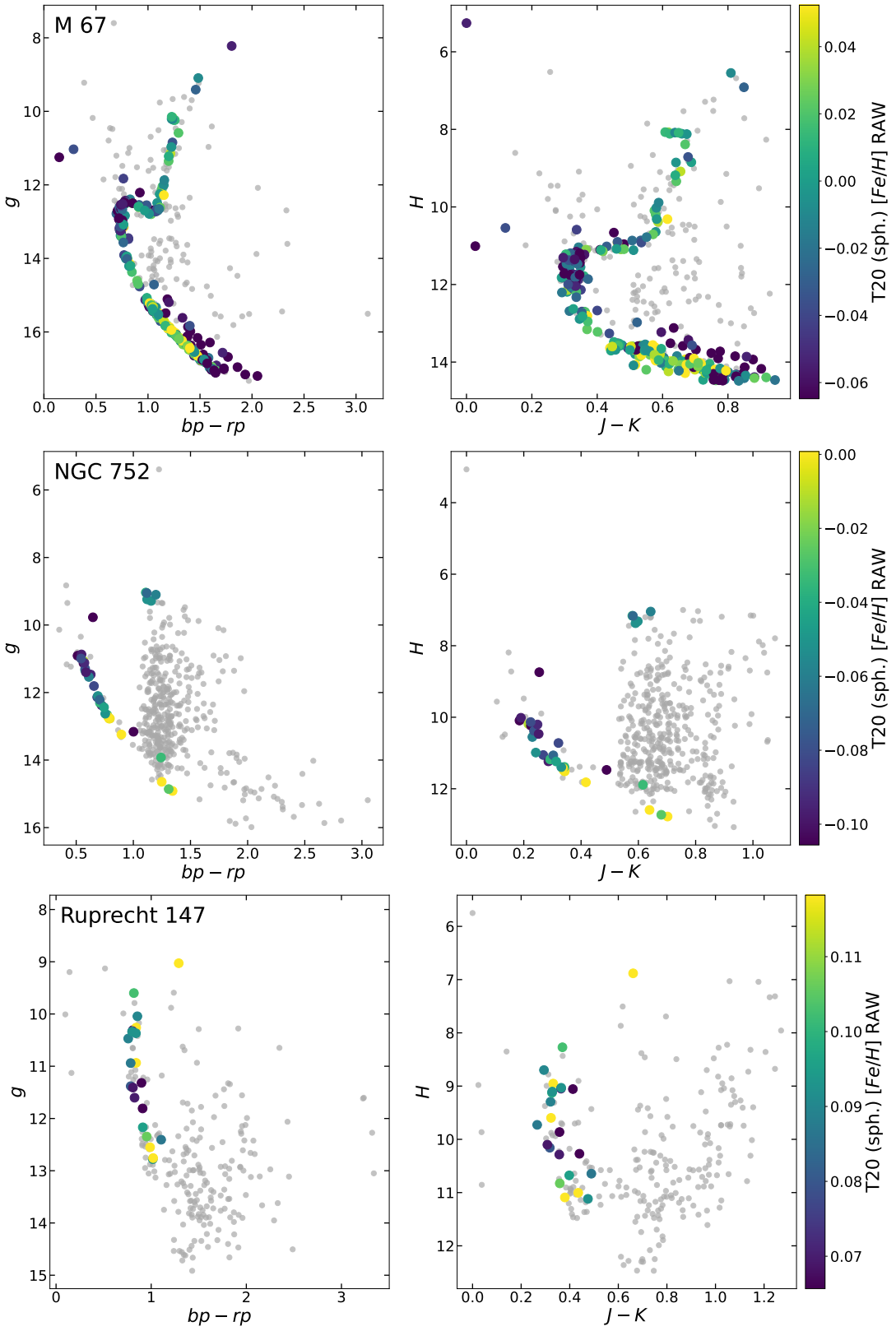

Figure 3.1: CMDs of M 67 (top), NGC 752 (middle), and Ruprecht 147 (bottom) with PM and RV determined cluster members colored by [Fe/H] and non-members are shown in grey. Note stellar data quality selection criteria has already been applied to these member stars. Note the magnitude errors are smaller than the markers.

3.3 SDSS/APOGEE Survey

In this work, we use data from the Apache Point Observatory Galactic Evolution Experiment surveys (APOGEE-1 & -2; Majewski et al. 2017, Majewski et al., *in prep*), which are part of the SDSS-III & -IV projects (Eisenstein et al. 2011, Blanton et al. 2017). Spectroscopic data were observed in both hemispheres with 2.5m telescopes (Gunn et al. 2006, Bowen & Vaughan 1973) at APO (Apache Point Observatory, New Mexico, USA) and LCO (Las Campanas Observatory, La Serena, Chile), the using the APOGEE-N and -S spectrographs (Wilson et al. 2019), respectively. The targeting selection for APOGEE is described in Zasowski et al. (2013; 2017), Beaton et al. (2021), and Santana et al. (2021), with targeting for open clusters being further described in Frinchaboy et al. (2013) and Donor et al. (2018).

3.3.1 SDSS/APOGEE Survey DR17

In order to reliably detect and characterize the effects of diffusion in stars in clusters, we need a large uniform data set of spectroscopic abundances. In this work, our stellar data are taken from the final data release of the APOGEE-2 survey (DR17; Abdurro'uf et al. 2022). A full description of the APOGEE DR17 data quality and parameter limitations is presented in Abdurro'uf et al. (2022) and Holtzman et al. (*in prep*). Furthermore, unlike previous releases, DR17 has provided supplementary alternate libraries that were constructed with different underlying physical assumptions, and have been been made available as a part of the APOGEE DR17 release[3]. In this work, we investigate the

[3]The alternate DR17 libraries and links to the data are found at: https://www.sdss4.org/dr17/irspec/apogee-libraries/

"primary" DR17 library based on Synspec and one alternate library using Turbospectrum 20 that utilizes spherical geometry for giant stars ($logg \leq 3$), similar to previous data releases (i.e., APOGEE DR14 and APOGEE DR16[4]).

3.3.2 APOGEE Spectral Library Selection

The primary release for APOGEE DR17 updated the ASPCAP analysis code compared to previous data releases, as the library of synthetic spectra were calculated using Synspec code, which allows for Non-Local Thermodynamic Equilibrium (NLTE) line formation in a plane parallel geometry. However, unlike previous releases, DR17 has provided supplementary alternate libraries that were constructed with different underlying physical assumptions, and have been been made available as a part of the APOGEE DR17 release. One alternate library that is of interest to this work creates spectral libraries using Turbospectrum 20 that utilizes spherical geometry for giant stars ($logg \leq 3$), similar to previous data releases (i.e., APOGEE DR14 and APOGEE DR16). For our results, we have chosen the spectral libraries created from Turbospectrum 20 LTE, with spherical geometry included, to be consistent with previous works (Souto et al. 2018).

We provide the comparative analysis between the Synspec NLTE and Turbospectrum 20 LTE libraries, in regards to the resulting effect on the atomic diffusion signature, in supplemental results (see Appendix B). We also, in Appendix B, provide the results of our analysis conducted with the primary Synspec NLTE DR17 spectral library.

[4]https://data.sdss.org/sas/dr17/apogee/spectro/speclib/synth/ turbospec/marcs/

3.3.2.1 Selected Clusters Detailed Spectral Analysis

To enhance precision and validate ASPCAP DR17 abundance results, we conducted a detailed manual analysis for a small fraction (seven stars from Rup 147 and nine from NGC 752) of stars from our main sample. This involved comparing observed spectral lines to their best synthetic fits, with abundance determinations derived from the visual best fit in conjunction with the minimum chi-square (χ^2) criterion. This manual analysis provides independent results for a smaller sample that can be cross-referenced with the automated ASPCAP results.

To generate the spectral synthesis, we adopted $T_{\mathrm{eff's}}$ from the DR17 (assuming results from MARCS models and Turbospectrum) and also from photometric calibration of González Hernández & Bonifacio (2009). We adopted the color indexes where photometric bands J, H, K_s are from 2MASS survey (Cutri et al. 2003). We adopted reddening of $A_V = 0.06$ for Rup 147 and $A_V = 0.07$ for NGC 752, as determined by Cantat-Gaudin et al. (2020).

The surface gravities derived are from physical relations assuming stellar mass and bolometric magnitudes from MIST isochrones (with the respective age and metallicity for each cluster). For microturbulence velocity, we adopted the values using the same procedure as in Souto et al. (2016, or Smith et al. 2013). We also adopted the same spectral lines as Souto et al. (2018) to determine individual abundances for each element.

It is important to note that for specific elements, such as Na, Ca, Ti, V, Cr, and Ni, their atomic lines became smaller as the effective temperature increased, particularly for turnoff stars. This made determining precise individual abundances more challenging or

even impossible for some stars. The abundance values for Fe, C, Mg, Si, Ca, and Ti deteremined by out "by-hand" detail analysis for the individual stars within NGC 752 and Ruprecht 147 can be found in Table 3.1.

Table 3.1: Detail Analysis Abundances

2MASS ID	[Fe/H] (dex)	[C/H] (dex)	[Mg/H] (dex)	[Si/H] (dex)	[Ca/H] (dex)	[Ti/H] (dex)
			NGC 752			
2M01563867+3654342	-0.11 ± 0.046	-0.17 ± 0.022	-0.03 ± 0.099	-0.13 ± 0.055	—	—
2M01561109+3745114	-0.18 ± 0.046	-0.18 ± 0.022	-0.08 ± 0.099	-0.17 ± 0.055	—	—
2M01575517+3752461	-0.10 ± 0.046	-0.21 ± 0.022	+0.02 ± 0.099	-0.15 ± 0.055	—	—
2M01582759+3735222	-0.01 ± 0.046	-0.20 ± 0.022	-0.03 ± 0.099	0.0 ± 0.055	—	—
2M01571048+3802065	-0.05 ± 0.046	-0.13 ± 0.022	-0.06 ± 0.099	0.0 ± 0.055	-0.15 ± 0.041	—
2M01541251+3823562	+0.05 ± 0.046	-0.09 ± 0.022	+0.11 ± 0.099	0.03 ± 0.055	0.14 ± 0.041	0.07 ± 0.046
2M01554062+3749375	+0.02 ± 0.046	—	-0.03 ± 0.099	-0.01 ± 0.055	0.01 ± 0.041	-0.14 ± 0.046
2M01551528+3750312	-0.01 ± 0.069	-0.26 ± 0.062	-0.06 ± 0.06	0.05 ± 0.062	0.1 ± 0.061	-0.18 ± 0.14
2M01562163+3736084	-0.04 ± 0.069	-0.25 ± 0.062	-0.11 ± 0.06	-0.04 ± 0.062	0.01 ± 0.061	-0.16 ± 0.14
			Ruprecht 147			
2M19170433-1623185	0.12 ± 0.046	-0.12 ± 0.022	0.09 ± 0.099	0.15 ± 0.055	0.15 ± 0.041	—
2M19131541-1616123	0.12 ± 0.046	-0.08 ± 0.022	0.16 ± 0.099	0.2 ± 0.055	0.08 ± 0.041	—
2M19164922-1613222	0.16 ± 0.046	-0.1 ± 0.022	0.15 ± 0.099	0.19 ± 0.055	0.16 ± 0.041	—
2M19152406-1621519	0.09 ± 0.046	-0.12 ± 0.022	0.13 ± 0.099	0.14 ± 0.055	0.14 ± 0.041	—
2M19134126-1610201	0.12 ± 0.046	-0.12 ± 0.022	0.15 ± 0.099	0.13 ± 0.055	0.32 ± 0.041	0.28 ± 0.046
2M19142816-1620023	0.15 ± 0.046	-0.1 ± 0.022	0.15 ± 0.099	0.09 ± 0.055	0.15 ± 0.041	0.02 ± 0.046
2M19164574-1635226	0.11 ± 0.069	-0.05 ± 0.062	0.06 ± 0.06	0.13 ± 0.062	0.13 ± 0.022	0.02 ± 0.14

3.4 Analysis

3.4.1 Cluster Membership

For this work, we are using the SDSS/APOGEE survey as it provides sufficient stars in the open clusters M67, NGC 752, and Ruprecht 147. We utilized cluster membership probabilities from the Open Cluster Chemical Analysis and Mapping survey (OCCAM, Frinchaboy et al. 2013, Cunha et al. 2015, Donor et al. 2018; 2020, Myers et al. 2022), for these selected clusters. Specifically, we used OCCAM the proper motion and radial velocity membership probabilities from the Myers et al. (2022) DR17 VAC[5] to select for cluster membership, where proper motion probabilities were greater than 0.01 and radial velocity probabilities were greater than 0.01. As stated previously in §3.1, we did not use the metallicity-based probability as it would remove stars with potential signatures for atomic diffusion since the Fe-surface abundance would change at and around the turn off phase. The surface variation for clusters NGC 752, Ruprecht 147, and M 67 can be seen in Figure 3.1.

3.4.2 Selecting Useful Abundances from SDSS/APOGEE DR17

We selected stars with reliable elemental measurements by applying ASPCAP quality bitwise flags (fully described in Jönsson et al. (2020) and Holtzman et al, *in prep*) as well as requiring a signal-to-noise ratio (S/N) greater than or equal to 100. To remove possible binaries from our sample, we applied a VSCATTER cut to be less than 1 km s^{-1}. A sum-

[5]https://www.sdss.org/dr17/data_access/value-added-catalogs/?vac_id=open-cluster-chemical-abundances-and-mapping-catalog.

mary of our sample selection criteria adopted are listed in Table 3.2. Note STARFLAG and ASPCAP bit-wise flags are described in: https://www.sdss.org/dr17/irspec/apogee-bitmasks/ .

After applying this criteria, we are able to use open clusters NGC 752 (35 stars) and Ruprecht 147 (23 stars) for our investigation, in addition to comparing to the previously studied M67 (Souto et al. 2018), as these clusters have at least one star in the main sequence (MS), turn-off (TO), and red giant branch (RGB) evolutionary phase. Having at least one star in each of these phases is crucial for our investigation as it allows us to see surface abundance variation that are tied to atomic diffusion.

Table 3.2: Stellar Data Quality Selection Criteria

Source	Parameter	Selection
	Data Quality Cuts	
APOGEE/DR17	STARFLAG - Stellar Parameters	$! = 16$
APOGEE/DR17	ASPCAP Flag - Chemistry	$! = 23$
APOGEE/DR17	VSCATTER (km s^{-1})	< 1
APOGEE/DR17	SNREV	> 100
	Membership Cuts	
(Myers et al. 2022)	RV_PROB	> 0.3
(Myers et al. 2022)	PM_PROB	> 0.3

3.5 Results & Discussion

In this section, we present our results as well as compare abundances derived from the APOGEE pipeline and derived from our by-hand analysis with MIST models for open clusters NGC 752 and Ruprecht 147. The cluster NGC 752 is comprised of 20 main

sequence, 9 turn-off, 1 sub-giant, and 5 red giant stars. While the cluster Ruprecht 147 is comprised of 13 main sequence, 9 turn-off, and 1 red giant stars. The six elements (Fe, C, Mg, Si, Ca, and Ti) we have chosen to investigate are those in common between the uncalibrated (or raw) APOGEE pipeline, by-hand analysis, and MIST models. The raw APOGEE parameters and elemental abundance can be found in FPARAM and FELEM, respectively. For ease, the uncalibrated surface gravity and effective temperature can be found with LOGG_SPEC and TEFF_SPEC, respectively.

The criteria we use to identify whether changes in surface abundances are significant or not is as follows: We find the mean and standard deviation of the [X/H] abundance observed in the stars considered members in NGC 752 and Ruprecht 147. Next, we compare the standard deviation to the standard errors found Souto et al. (2018) as these errors were larger than those assumed for the APOGEE DR17 pipeline from Jönsson et al. (2020). If the difference of those values were larger than 1σ, where σ is equal to the standard error, the measured change in abundance is significant while differences less than 1σ were considered not significant. This method was applied to M 67, a cluster that have been confirmed to have surface abundance variations determined to be signatures of atomic diffusion in Souto et al. (2019; 2018), Liu et al. (2019), Bertelli Motta et al. (2018), Gao et al. (2018), Önehag et al. (2014), and found this method to be a useful indicator of significant surface abundance changes.

3.5.1 Abundance Trends

In our investigation, we look at abundance trends for six elements: Fe, C, Mg, Si, Ca, and Ti for both open cluster NGC 752 and Ruprecht 147. (Na was also investigated as a potential element affected by diffusion; however, the determined uncertainties in our measurements were too large to obtain any significant insight, therefore this element was removed from this work.)

In Figure 3.2, metallicity is plotted as a function of effective temperature for both NGC 752 (*left*) and Ruprecht 147 (*right*). Markers shown with a blue 'x' are raw APOGEE DR17 assuming Turbospectrum and MARCS models, while markers shown with a yellow square and red circles represent by-hand analysis assuming uncalibrated effective temperature and physical surface gravity and photometrically calibrated effective temperature and physical surface gravity, respectively. The MIST model used in our comparison is shown in a solid black line. Figures 3.3 and 3.4, shows our six elements as a function of effective temperature for NGC 752 and Ruprecht 147, respectively. These plots follow a similar marking scheme as Figure 3.2.

3.5.1.1 Iron

Cluster NGC 752 has mean metallicity just below solar $\langle$[Fe/H]$\rangle = -0.03$ dex with a standard deviation of 0.32 dex. When comparing the standard deviation to the stand error for [Fe/H], we find the difference to be greater than 3σ implying there is a change in the surface Fe-abundance supporting stellar evolutionary process is causing the change. While in cluster Ruprecht 147 has $\langle$[Fe/H]$\rangle = 0.05$ dex with a standard deviation of 0.12

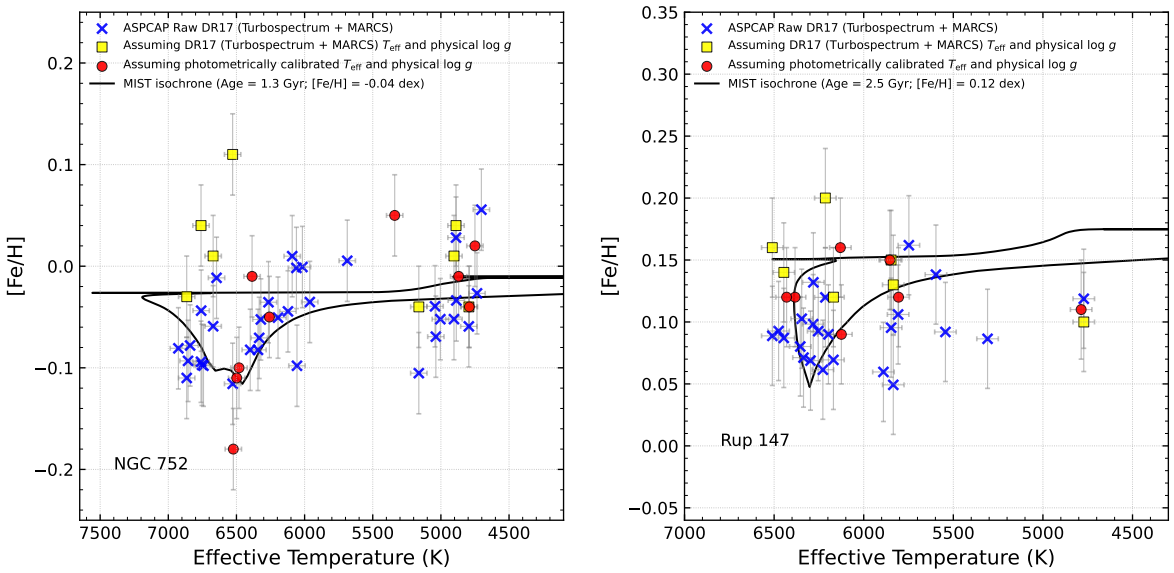

Figure 3.2: $[Fe/H]$-T_{eff} using TurboSpectrum and MARCS for clusters NGC 752 (*left*) and Ruprecht 147 (*right*). The blue 'x' markers represent the raw APOGEE pipeline values using Turbospectrum with spherical geometry and MARC models. The yellow squares represent by hand analysis where the raw T_{eff} from APOGEE and physical $\log g$ were used to determine abundances. The red circles represent by hand analysis where photometrically calibrated T_{eff} and physical $\log g$ were assumed to determine abundance. The MIST model we compare to is represented by a solid black line.

dex and when compared to the standard error for [Fe/H], we find the difference to be 0.73σ. For Ruprecht 147, within our uncertanties we do not find a signifficant change in the surface Fe-abundance, however atomic diffusion could still affect star in this cluster.

For NGC 752, there is an apparent trend in metallicity in the raw APOGEE values and a stronger trend in the by-hand analysis that assumes photometrically calibrated effective temperature and physical surface gravity which follows the MIST model determined metallicity. Where for Ruprecht 147 the Fe-abundance does not show a strong variation in the raw APOGEE determined abundances, but the by-hand analysis that assumes photometrically calibrated effective temperature and physical surface gravity determined abundances seem to follow the MIST model.

3.5.1.2 Carbon

For our study of carbon, Figure 3.3, we find that stars in NGC 752 overlap with the model suggesting they show significant diffusion signatures plus additional abundance variations from mixing due to the first dredge up (FDU). The raw APOGEE mean [C/H] for NGC 752 is -0.10 dex with a standard deviation to be 0.32 dex. When comparing the standard error for carbon to the standard deviation we find the difference to be about 6σ which shows a significant change in the surface C-abundance. This supports stellar evolutionary change in the surface abundance like first dredge up, which carbon is know to be affected by this stellar mixing, and potentially atomic diffusion.

For Ruprecht 147, we find there is not a strong trend with both the raw APOGEE values and the by-hand values, the trend looks to have a shallow linear trend. The raw APOGEE mean [C/H] abundance for Ruprecht 147 is 0.13 dex with a standard deviation to be 0.29 dex. Comparing the standard deviation to the standard error we find the error to be about 4σ. Having this large of change suggested that the change in the surface C-abundance is significant supporting stellar mixing impacting the amount of carbon in the surface, e.g., the first dredge up and potentially atomic diffusion.

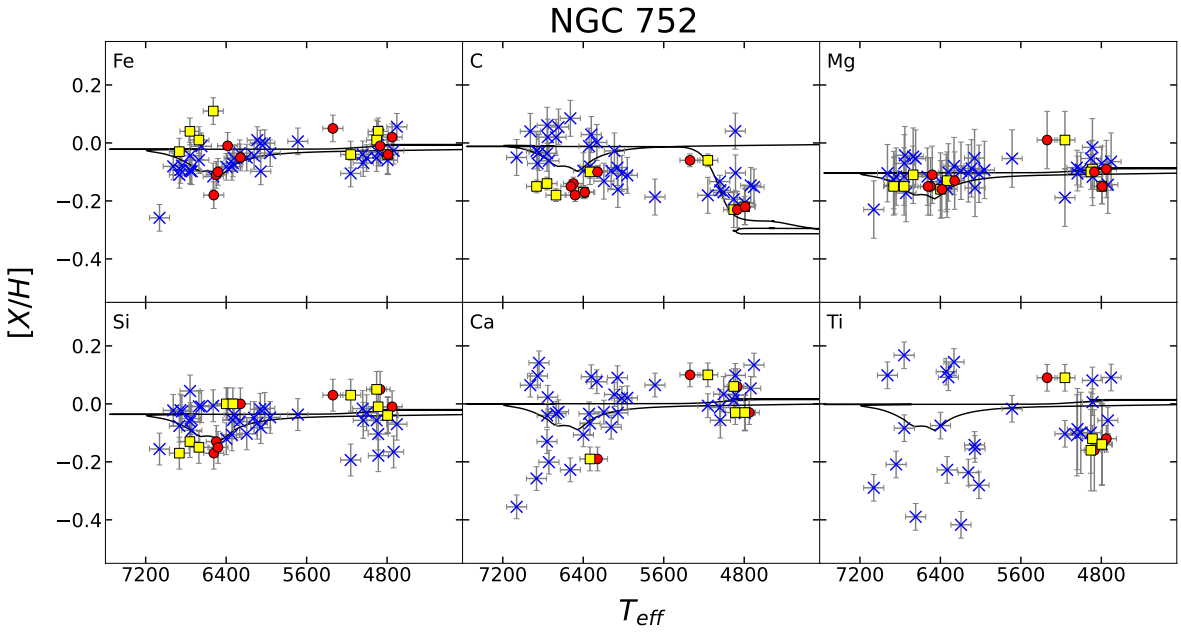

Figure 3.3: $[X/H]$-T_{eff} using TurboSpectrum and MARCS for clusters NGC 752. Similar markings as Figure 3.2 for the six element in our investigation.

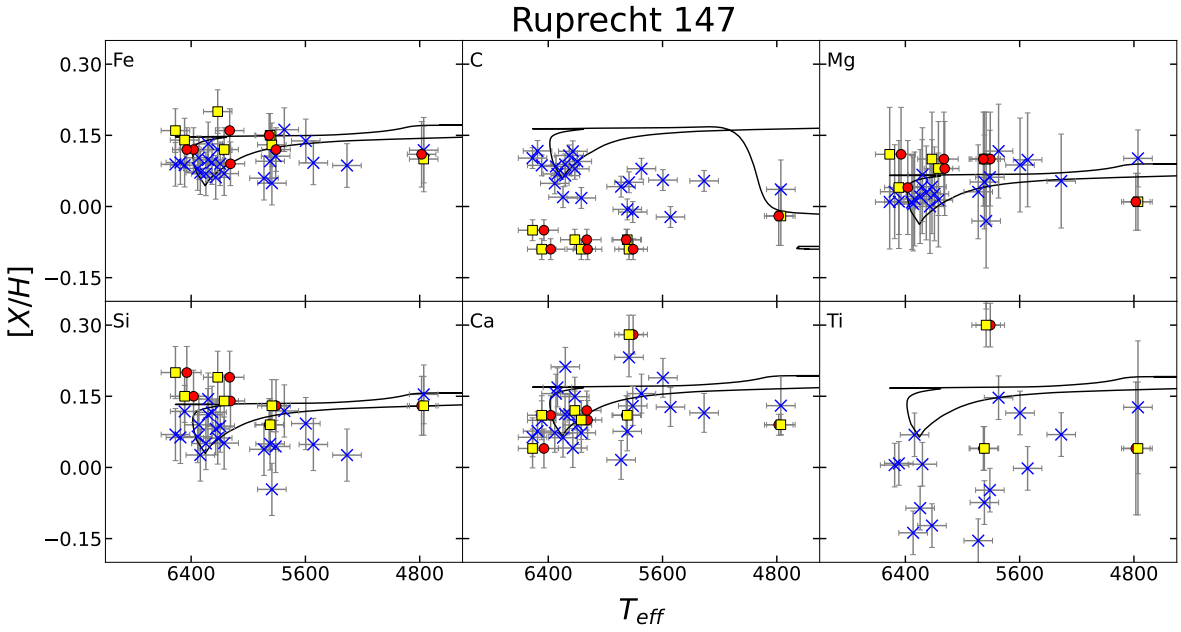

Figure 3.4: $[X/H]$-T_{eff} using TurboSpectrum and MARCS for clusters Ruprecht 147. Similar markings as Figure 3.2 for the six element in our investigation.

3.5.1.3 Magnesium

For cluster NGC 752, we find the raw APOGEE $\langle$[Mg/H]$\rangle = -0.01$ dex with a standard deviation of 0.58 dex. After comparing the standard deviation to the Mg standard error, we find a significant effect from diffusion, with a difference of almost 9σ. This supports this idea that atomic settling impacts the change in magnesium. The by-hand result follow a similar trend as the raw APOGEE values suggesting a significant change is measure with alternative analysis. This suggests that atomic diffusion could be a process causing this change.

For cluster Ruprecht 147, we find the APOGEE raw $\langle$[Mg/H]$\rangle = 0.09$ dex with a standard deviation to be 0.25 dex. When comparing the standard deviation to the standard error, we find the difference to be about 3σ. This implies the change in surface Mg-abundance to be significant and suggests that atomic diffusion could be the cause. Although this difference is significant it is not as large as what is found in NGC 752, which is almost 3 times larger than that observed in Ruprecht 147.

For Ruprecht 147, the raw APOGEE values follow a shallow, almost flat, linear trend implying a constant surface Mg-abundance. While for the by-hand analysis there is a slight increase in Mg turn-off, but as the error bars overlap this suggests the is not a significant increase of Mg.

3.5.1.4 Silicon

NGC 752 shows signs of atomic diffusion where the Si abundance decreases at the turn-off and the Si-abundance increases as the stars evolve into their RGB phase with the

by-hand analysis. The raw APOGEE values seem to follow the same trend. For NGC 752, the raw APOGEE mean $\langle$[Si/H]$\rangle = -0.09$ dex with a standard deviation of 0.53 dex. After comparing the spread to the standard error, we found a difference of 7.5σ; this implies a significant change in surface Si-abundance and supports that stellar mixing could be causing the change.

While for Ruprecht 147, the Si-abundance actually increases at the turn-off instead of decreasing with the by-hand analysis. For the raw APOGEE values, the trend is not as strong of a signature. For Ruprecht 147, the raw APOGEE $\langle$[Si/H]$\rangle = 0.14$ dex with a spread of 0.22 dex. When comparing the spread to the standard error, we find a difference of 2.5σ. This shows a significant change in surface Si-abundance in Ruprecht 147, but this change is three times less than the change found in NGC 752.

3.5.1.5 Calcium

NGC 752 the raw APOGEE values follow the atomic diffusion trend, though the values decrease much lower than the model predicts. The by-hand analysis follows a similar trend where the Ca-abundance decreases at the turn-off and increase as the star evolves. We find the raw APOGEE $\langle$[Ca/H]$\rangle = -0.10$ dex with a standard deviation of 0.35 dex. After comparing the spread to the standard error for silicon, we found a difference to be almost 5σ. This shows a significant change in the surface Ca-abundance and supports stellar mixing, such as atomic diffusion, as a potential source of the observed abundance change.

For Ruprecht 147, we found a raw APOGEE $\langle$[Ca/H]$\rangle = 0.05$ dex with a standard deviation of 0.27 dex. Comparing the spread and the standard error, we found a difference

of almost 3.5σ which shows a significant change in the measure surface Ca-abundance. Supporting stellar mixing to be the reason for surface changes. The by-hand analysis also follows this similar trend, when the change in abundance is significant (see Figure 3.4).

3.5.1.6 Titanium

For NGC 752, we found the raw APOGEE $\langle$[Ti/H]$\rangle = -0.07$ dex with a spread of 0.47 dex and found the difference between the spread and the standard error to be about 2σ. This would suggest a significant change in the surface Ti-abundance. For Ruprecht 147, we found the raw APOGEE $\langle$[Ti/H]$\rangle = 0.14$ dex with a spread of 0.23 dex and found the difference between the spread an standard error to be about 0.7σ. Since the difference is less than 1σ this suggest the change in surface Ti-abundance is not significant. For stellar abundance determined by the by-hand analysis, we could not determine abundances at the turnoff for NGC 752 because their spectral lines became small or blended by other lines. Therefore, we can not conclude the full extent of potential diffusion signatures.

3.5.2 Minimized Chi-Squared Comparison

We did a quantitative comparison between the derived [Fe/H] abundance values, assuming photometrically calibrated effective temperature and physical surface gravities, and the MIST diffusion models using a minimized chi-squared comparison for NGC 752 and Ruprecht 147. Our comparison is shown in Figures 3.5 and 3.6 for NGC 752 and Ruprecht 147, respectively. The diffusion models used to compare to NGC 752 are in the top panel of Figure 3.5 for ages 800 Myr, 1.0 Gyr, 1.3 Gyr, 1.6 Gyr, and 2.0 Gyr. As for diffusion models used to compare to Ruprecht 147, they are in the top panel of Figure 3.6 for ages 1.6 Gyr, 2.0 Gyr, 2.5 Gyr, 3.2 Gyr, and 4.0 Gyr. The reliable diffusion model stellar parameter values used in our comparison were selected based on their closest effective temperature, surface gravity, and metallicity to the derived observed stellar quantaties. Note, selecting the model star without these three parameters will give you vastly different χ^2-value as it will select the wrong stellar evolutionary phase to compare the observed star, i.e., the giant phase and main sequence phase could be confused as these phases have similar effective temperatures [Fe/H] as seen in Figure 3.2. The dashed horizontal grey line represents the χ^2-value for a constant mean [Fe/H] abundance value for NGC 752 and Ruprecht 147 as [Fe/H] $= -0.04$ and [Fe/H] $= 0.12$ dex, respectively. Constant mean [Fe/H] abundance model assumes the [Fe/H] of each evolutionary phase does not change. To do this type of comparison, and it be valid, the metallicities had to be taken out of log-space.

NGC 752 MIST models fit better as the χ^2-values are lower than the χ^2-value for assuming constant [Fe/H] abundance indicating the abundance variation is significant

and suggests that the cluster has atomic diffusion signatures. Furthermore, in Ruprecht 147 the χ^2-value for assuming a constant [Fe/H] and the χ^2-values for the MIST models are similar. This suggests there is a weak abundance variation in Ruprecht 147 and hence, it is inconclusive if the cluster has atomic diffusion signatures.

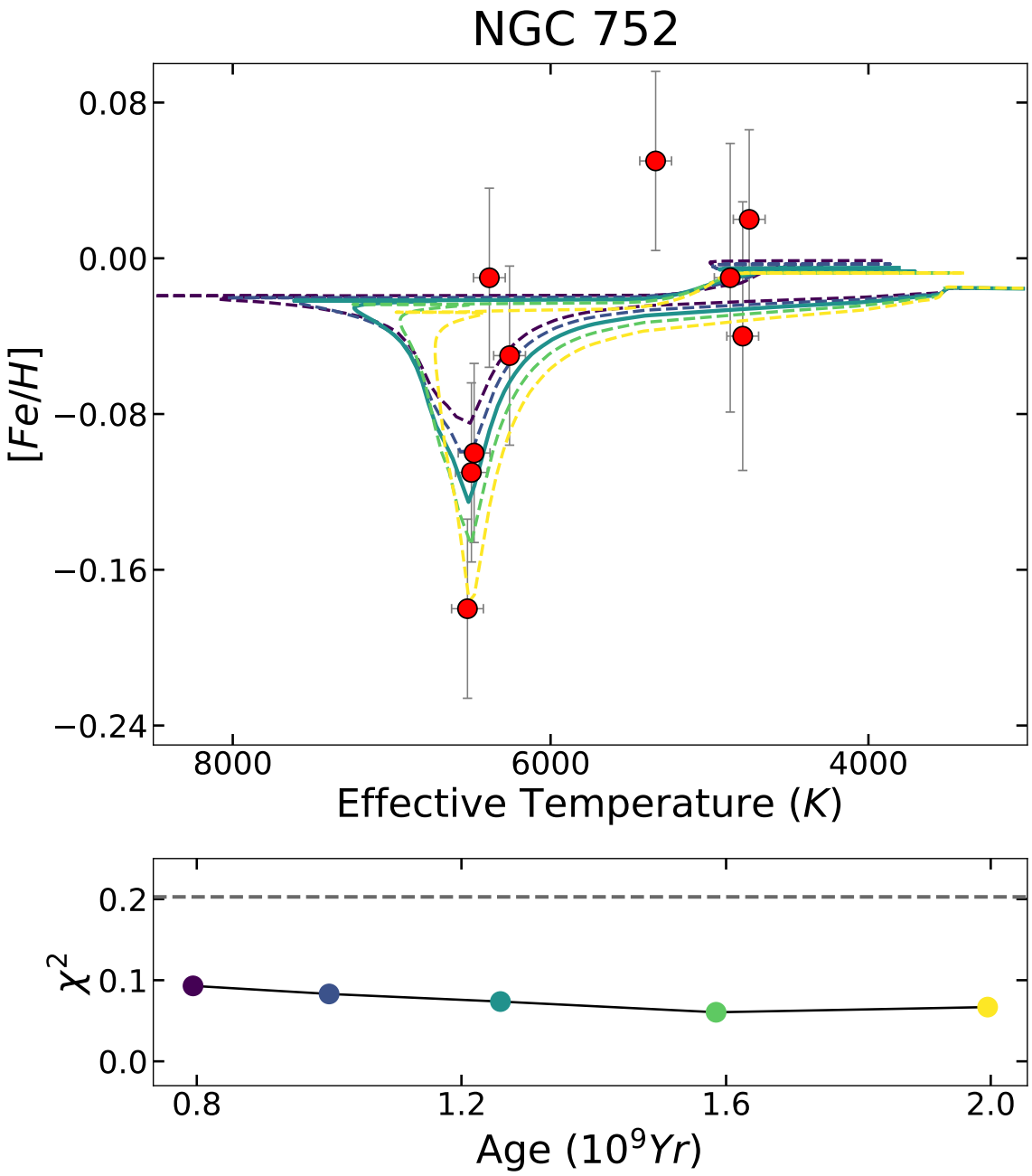

Figure 3.5: (*Top*): Shows metallicity as a function of effective temperature for NGC 752. The solid and dashed lines represent MIST isochrones assuming [Fe/H]=-0.04 and ages = 0.8, 1.0, 1.3, 1.6, 2.0 Gyrs. (*Bottom*): A chi-squared minimization comparing the derived metallicities with MIST isochrones. The grey dashed line is a chi-squared comparison assuming the mean metallicity is constant. The color of the circle markers correspond to the five models shown above to calculate their chi-squared value.

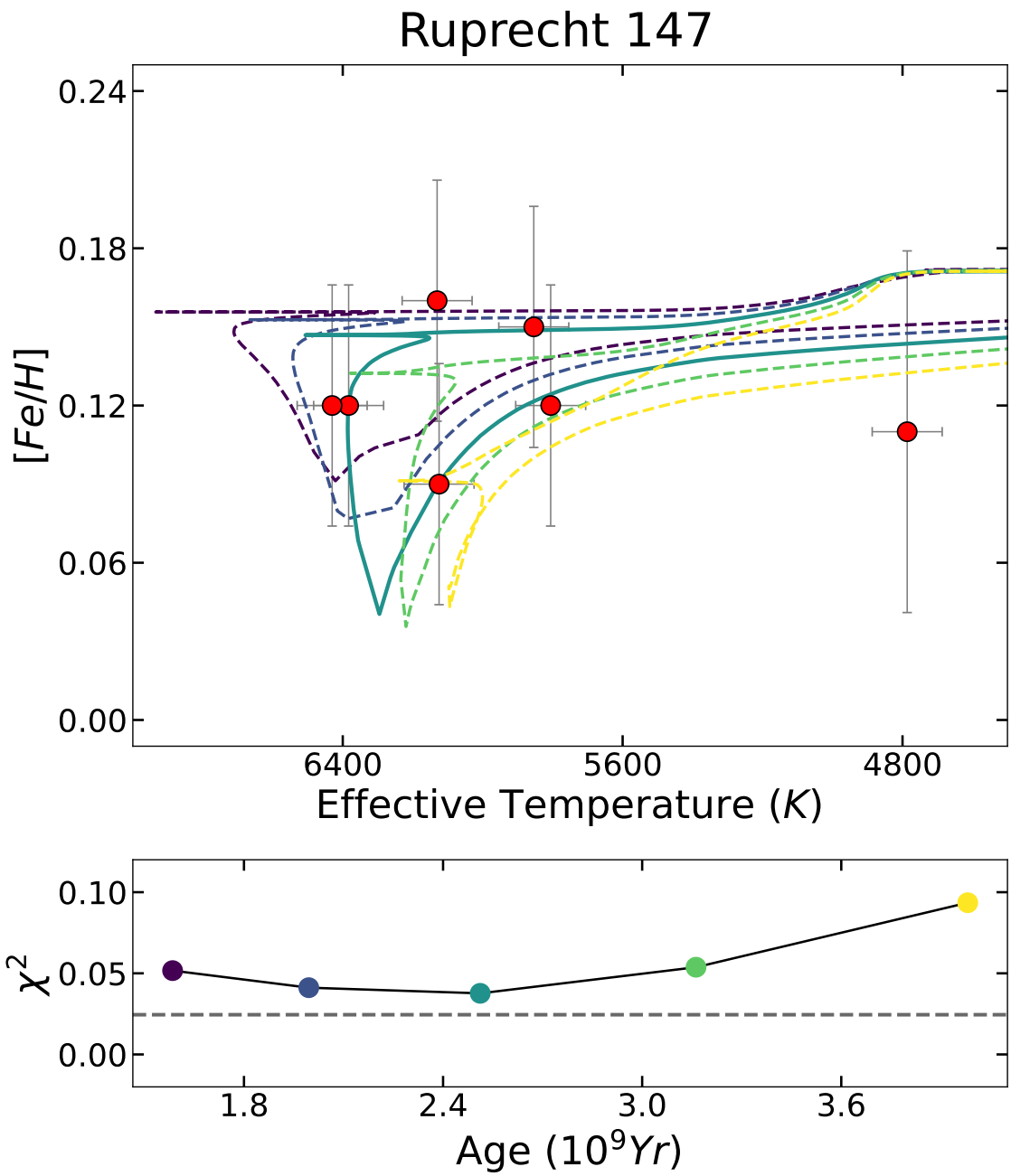

Figure 3.6: Similar to Figure 3.5 for Ruprecht 147, where the MIST isochrones assume [Fe/H]=0.12 and ages = 1.6, 2.0, 2.5, 3.2, 4.0 Gyrs.

3.5.3 Implications

With this work and the work of Souto et al. (2018), we find that atomic diffusion can and does have a significant effect on the measured abundances of star at the MSTO and sub-giant branch for stars older than ~ 1 Gyr. While our work cannot full characterize this effect, this work does allow us to state the following:

- We do caution about using observed metallicities of turnoff stars without accounting for diffusion, this will lead to selection of isochrones too metal-poor for the birth abundance of the star, yielding a wrong age determination. Our results drive us to echo the finding of VandenBerg et al. (2002), who showed that atomic diffusion could impact age determination by 10% as we find more clusters with indications of atomic diffusion. This is something to consider when modeling as well as age dating star within the field. Dotter et al. (2017) states assuming the incorrect constant-metallicity for an isochrone can lead to age estimates being over estimated by about 20% compared to isochrones that variable-metallicity assumptions. Not accounting for diffusion yields a systematic offset to the true ages which will effect analysis of mapping Galactic history.

Our findings show that atomic diffusion is an issue for age determination of MSTO and SGB stars, but at this point we do not have enough data to fully characterize the changes observed in order to identify the correct birth-metallicity isochrone.

While our current study is insufficient to map the effect of diffusion to enable one to recover the abundance from formation, we hope further high-precision abundance mapping of star on clusters covering a range of age and metallicity will enable this in

future work. We note that these studies will require high-S/N abundance data from more clusters covering a wider range of ages, including sufficient converge of MS, MSTO, SGB, *and* RGB within the cluster to measure the change in surface abundances due to atomic diffusion.

Chapter 4

Conclusion

This dissertation has explored how variations in stellar surface chemistry can be used as a tool to probe the ages of stars, and conversely hinder the accurate ages of stars depending on the evolutionary stage of the star being studied. In this chapter, we present a summary of our findings.

4.1 The Expanded APOGEE [C/N]-Age Calibration for Old Metal-Poor Stars

We have established a new calibration for APOGEE DR17 data that provides the following relation for RGB stars that experience the first dredge-up, but have not experienced extra-mixing (i.e., APOGEE DR17 stars with $\log g < 3.2$ plus applying $\log g$ cut from Shetrone et al. (2019)) as shown by Equation 2.1. This relationship can be applied to the RGB stars within the metallicity range $-1.2 \leq [Fe/H] \leq +0.3$ based on our sample.

Comparison with asteroseismic results of APOKASC and APO-K2 suggests that [C/N] based ages are at least as reliable, if not more reliable for measuring giant star ages in this $\log g$ range. As APOKASC results suggest that [C/N] based ages are consistent within 10% for 99.77% of giants and APO-K2 results suggest that [C/N] based ages are consistent within 10% for 99.92% of giants.

We find that the majority of stars that are found to be "older than the Universe" are either (1) rapidly rotating, (2) in a binary system, or (3) a combination of the two. As this relationship is being applied to a greater sample one should try to exclude binaries and rapidly rotating stars to build a reliable sample.

With this new calibration, we can now age-date over 45% of all SDSS/APOGEE DR17 sample, 300,000+ stars. This will allow us to gain a better insight into more regions of the Galaxy, as we are no longer restricted to the metal-rich disk, and will allow us to paint a more coherent picture of our Galaxy's evolution, that will be explored in Otto et al. *in prep.*

4.2 The Impact of Atomic Diffusion on Stellar Abundance Measurements

Atomic diffusion is a process that has long been ignored, as it has previously been determined to be negligible as a surface abundance variation. However, as surveys become more accurate and precise, we find that this stellar process should be no longer be neglected. In this work, we have investigated atomic diffusion signatures within two open

clusters: NGC 752 and Ruprecht 147. We found that NGC 752 has significant signatures of atomic diffusion while Ruprecht 147 is inconclusive with current data quality. With ESA *Gaia* allowing us to accurately measure absolute magnitudes for stars at and around the turnoff, where the affect of atomic diffusion is maximum, neglecting atomic diffusion will result in systematically incorrect metallicities resulting in incorrect age determinations. As large scale spectroscopic surveys start to use these stars (e.g., GALAH; Hayden et al. 2022), the impact of neglecting the effect of atomic diffusion will introduce systematics that will affect the interpretation of Galactic evolution. There needs to be an increase sample of clusters with full coverage of the cluster to calibrate the change in surface abundance, which we hope to address in future work.

Appendix A

[C/N]-Age Linear Fit

In this appendix, we present, for completeness, a linear fit to the cluster sample, which we chose not to use due producing numerous stars that would be deemed older than the age of the Universe.

A.1 Linear Fit Results

After application of these additional membership and cluster age cuts the sample used for our [C/N]-age calibration (Figure 2.6) is comprised of the 49 clusters (530 stars) from Spoo et al. (2022) plus four globular clusters: 47 TUC, M 71, M 4, and M 5 (31 stars). The full sample covers an age range of $8.62 \leq \log[Age(\mathrm{yr})] \leq 10.13$ and a metallicity range of $-1.2 \leq [\mathrm{Fe/H}] \leq +0.3$. The individual globular cluster stars used in the calibration extension are shown in Table 2.2.

A.1.1 The Extended DR17 [C/N] Abundance/Age Calibration

In log-log space the relationship between stellar age and [C/N] appears to be linear; our best fit is given by

$$\log[Age(\mathrm{yr})]_{\mathrm{DR17}} = 10.23\,(\pm 0.08) + 2.48\,(\pm 0.20)\,[\mathrm{C/N}] \tag{A.1}$$

and yields a Pearson coefficient of $R = 0.86$. The linear fit given by Equation 2.1 and shown in Figure 2.6 uses an Orthogonal Distance Regression (ODR) method, from the `scipy` package ODR, to ensure errors in [C/N] and log[Age (yr)] were both equally considered in our fit.

A.2 Comparison to Asteroseismic Ages

A natural comparison can be done to asterosiesmic-based ages. For this work we compared to the APOKASC 3 survey (Pinsonneault et al. 2018, Pinsonneault et al. *in prep.*) and the recently released APO-K2 (Schonhut-Stasik et al. 2024). The APOKASC 3 survey uses a combination of APOGEE and Kelper data to obtain stellar ages while APOK-K2 uses a combination of APOGEE and K2 data (Warfield et al. 2024). Warfield et al. (2024) also recalculated ages for the the APOKASC2 stars with their age determined method. The following sections details our comparison to the two surveys and our verification of our [C/N]-ages.

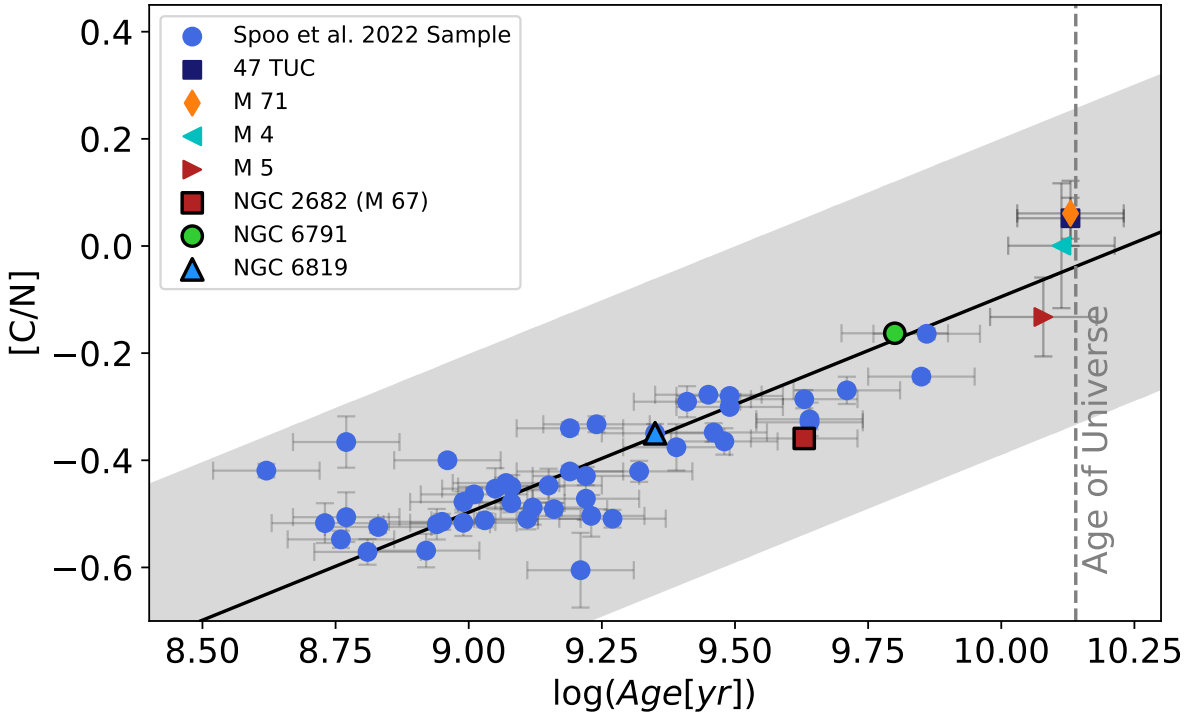

Figure A.1: The [C/N] versus log(*Age*[yr]) distribution for the final sample, composed of Spoo et al. (2022) open cluster sample and globular clusters: 47 TUC, M 71, M 4, and M 5. Clusters represented by blue circles are from the final calibration sample of Spoo et al. (2022). Globular clusters 47 TUC, M 71, M 4, M 5, are represented with an indigo square, an orange thin-diamond, a cyan left-triangle, and a red right-triangle, respectively. Our new linear fit is shown as a solid black line, and the fit's error envelope is shown with the grey region. The accepted age of the Universe is shown as a vertical grey-dashed line. The open clusters used in our asteroseismic age comparison are NGC 1817, NGC 2682 (M 67), NGC 6791, NGC 6811, and NGC 6819 and are shown in black outlined orange diamond, red square, green circle, red diamond, and blue triangle, respectively.

A.2.1 APOKASC 3

There are 6004 stars in our sample that is also in APOKASC 3. There are four open clusters and no globular clusters that are common between our sample and APOKASC 3, but only three open clusters were found to have reliable cluster membership based on OCCAM probabilities, hence we compare only these three clusters were compared on a

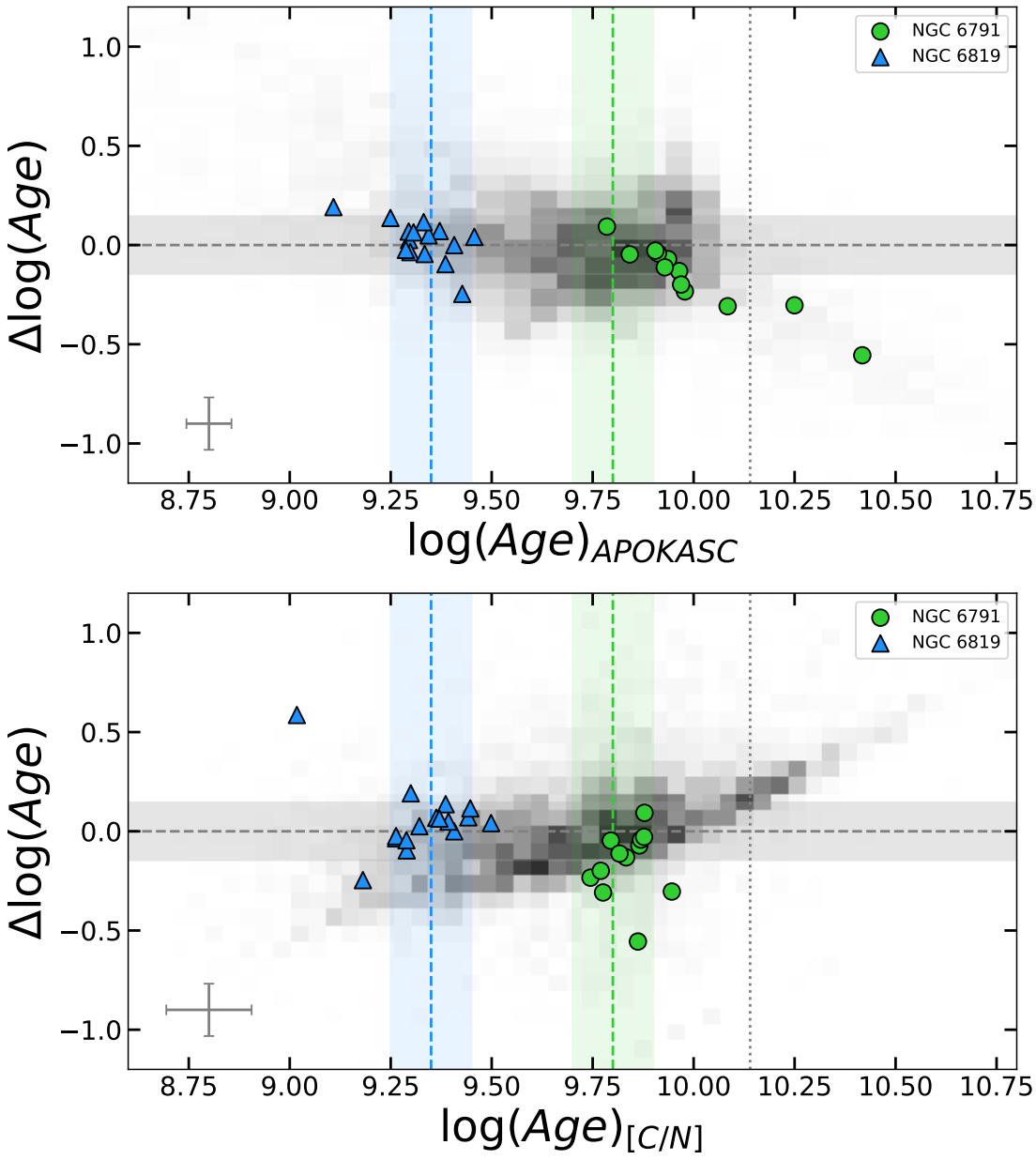

Figure A.2: $\Delta \log[Age(yr)]$ as a function of APOKASC3 log[Age (yr)] (*top*) and [C/N]-based log[Age (yr)] (*bottom*). The grey-gradient shaded regions represent bins of field stars; darker bins imply more stars. The green circles and blue triangles represent cluster member stars common to both samples NGC 6791 and NGC 6819, respectively. The vertical dashed lines are the Cantat-Gaudin et al. (2020) determined ages for each cluster and the respective shaded regions shows the error in cluster age. The horizontal grey-dashed line is where $\Delta \log[Age(yr)] = 0$ with the surrounding grey region representing a delta of -0.1 and $+0.1$. The vertical grey-dotted line shows the accepted age of the Universe. Median representative error bars are shown in each panel.

star-by-star basis.

For further verification, we apply our calibrations to open clusters that are also in the APOKASC sample: NGC 6791 and NGC 6819, shown in Figure 2.7. We find that our calculated ages from the DR17 calibration are consistent to the ages determined in Cantat-Gaudin et al. (2020) for all three clusters. The spread in the [C/N]-calibration ages within the cluster is due to the uncertainty of [C/N] in the individual cluster members, but such a spread is expected because our calibration is based on the average [C/N] abundance of the cluster.

The outlier stars from NGC 6791 that are older than the Universe, shown with green circles that are between the vertical grey dotted line and $\log[Age(yr)] = 10.50$ in the bottom panel of Figure A.2, both are found to be in binary systems by Price-Whelan et al. (2020) while only one is found to be rapidly rotating by Patton et al. (2024). The one found to be rapidly rotating is the green circle around $\log[Age(yr)] = 10.25$ and just to the right of the vertical grey dotted line that represents the accepted age of the Universe. Since the star is rapidly rotating, this usually indicates that mass transfer or tidal interactions has occurred, so the determined mass may not indicate age as well as potentially changing the surface abundance of carbon and nitrogen. Another thing to note for the rapidly rotating stars, the APOGEE DR17 pipeline assumes giants are not significantly rotating and the broadening effects that are not accounted for will change the observed carbon and nitrogen abundance.

Stars that are calculated to be older than the Universe only make up 4% of our sample, where about third of those stars we find them to be rapidly rotating (Patton et al. 2024) and/or in a binary system (Price-Whelan et al. 2020) which could change the

observed surface abundance of carbon and nitrogen (Bufanda et al. 2023). Comparison with APOKASC results suggests that [C/N] based ages can be trusted to 10% for 98.1% of giants.

A.2.2 APO-K2

There are 6881 stars in our sample that are also in APO-K2. There are 10 open clusters and no globular clusters that are common between our sample and APO-K2, but only three open clusters were found to have reliable cluster membership based on OCCAM probabilities, hence we compare only these three clusters were compared on a star-by-star basis.

For further verification, we apply our calibrations to open clusters that are also in the APO-K2 sample, NGC 2682 (M 67), and the APO-K2 recalibrated APOKASC 2 sample, NGC 6791 and NGC 6819, as shown in Figure A.3. We find that our calculated ages from the DR17 calibration are more consistent with the ages determined in Cantat-Gaudin et al. (2020) for three of the four clusters than APO-K2. For both, APO-K2 and this work, the ages of stars within NGC 2682 (M 67) are under estimated. From Figure A.1, the cluster NGC 2682 is further off the linear fit than the other APO-K2 cluster used in our comparison and explains why we show a discrepancy between our derived ages and the Cantat-Gaudin et al. (2020) ages used in our calibration. This discrepancy could be due to either additional effects in the APOGEE measurement of [C/N] (most NGC 2682 stars are significantly higher S/N which many reveal weaker lines) or there may be a systematic in the isochrone fitting age determination of NGC 2682 by Cantat-Gaudin

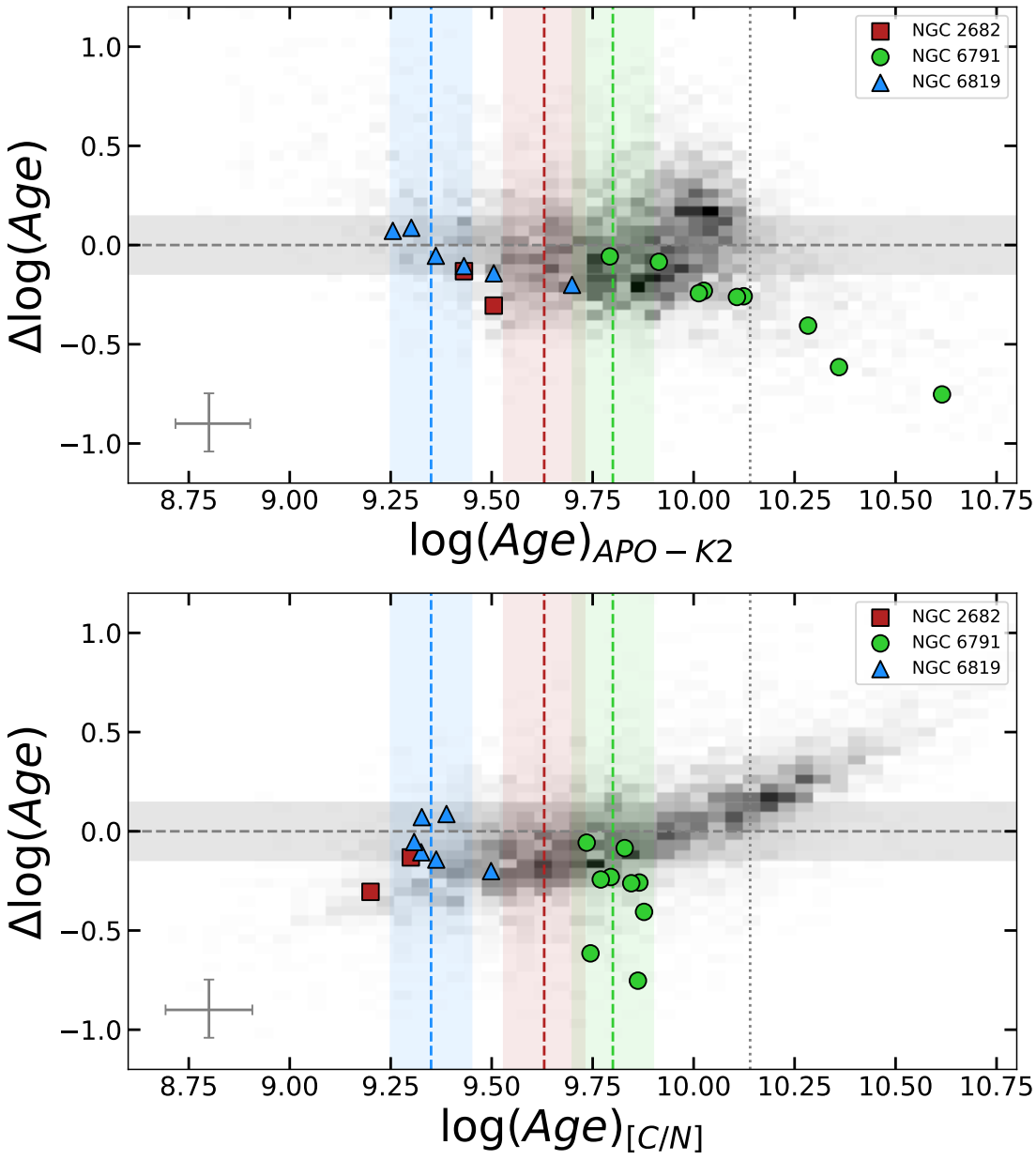

Figure A.3: $\Delta \log[Age(yr)]$ as a function of APO-K2 log[Age (yr)] (*top*) and [C/N]-based log[Age (yr)] (*bottom*). The grey-gradient shaded regions represent bins of field stars; darker bins imply more stars. The red squares, green circles, and blue triangles represent cluster member stars common to both samples NGC 2682 (M 67), NGC 6791, and NGC 6819, respectively. The vertical dashed lines are the Cantat-Gaudin et al. (2020) determined ages for each cluster and the respective shaded regions shows the error in cluster age. The horizontal grey-dashed line is where $\Delta \log[Age(yr)] = 0$ with the surrounding grey region representing a delta of -0.1 and $+0.1$. The vertical grey-dotted line shows the accepted age of the Universe. Median representative error bars are shown in each panel.

et al. (2020), similar to as is seen in Figure 6. of Hunt & Reffert (2023) where blue stragglers affect the main sequence turn off location for older clusters from their work as well as Cantat-Gaudin et al. (2020) and Kharchenko et al. (2013). Stars that are calculated to be older than the Universe only make up 20% of our sample, where a third of those stars we find to be in a binary system (Price-Whelan et al. 2020) which could change the observed surface abundance of carbon and nitrogen (Bufanda et al. 2023). Stars older than the Universe that were present in the APO-K2 catalog, were checked for binarity in common proper motion (using Gaia DR3) and assess for unresolved binaries using astrometric errors and markers (via priv. comm. regarding Schonhut-Stasik in prep.). Similarly, the spread in the [C/N]-calibration ages is due to the uncertainty of [C/N] in the individual cluster members, but such a spread is expected because our calibration is based on the average [C/N] abundance of the cluster. Comparison with APO-K2 results suggests that [C/N] based ages can be trusted to 10% for 99.5% of giants, as shown in Figure A.3.

Appendix B

Alternative SDSS/APOGEE DR17 Pipeline Comparison

In this appendix, we present our work on the effects of atomic diffusion within NGC 752 and Ruprecht 147, where we did a quick comparison of two versions of the ASPCAP pipelines (Turbospectrum 20 & SynSpec NLTE).

The first comparison we did was compare the uncalibrated (raw) effective temperature, as shown in Figure B.1. The top portion of Figure B.1 is the one-to-one plot, where the two raw effective temperatures are plotted against each other and majority of the OCCAM sample follow one-to-one trend. The two pipelines begin to diverge around 6000 K, where the pipeline using the Turbospectrum 20 spectral library determined T_{eff} hotter than the pipeline using the SynSpec NLTE spectral library, this is shown in more detail in the bottom portion of Figure B.1.

It appears cluster NGC752 is affected the most by which pipeline is being used to

determine T_{eff}. Also, M 67 seems to also shown to be affected by this as well but not as drastically. In particular, stars at the turnoff seem to be determined hotter with Turbospectrum 20 than with SynSpec NLTE.

We also did a comparison of raw effective temperature to the uncalibrated abundances of [Fe/H], [Mg/H], and [Si/H], as shown in Figures B.2, B.3, and B.4, respectively. The stars within these plots are colored by their uncalibrated surface gravityy (raw logg). Here, we can see giant stars (those in dark blue-purple) and parts of the MS (those in yellow) agree well between the two pipelines. As we approach the turn off, the pipeline disagree more. For NGC 752, we think it might be an effect of where grid edges are based on Figure 2 in the DR16 analysis paper (Holtzman et al. 2018, priv. conv. with Chris Hayes). Note the changes between the pipeline for Mg is inconclusive as Mg is an element that is affect by NLTE effects.

We compared the raw abundances of Fe, C, Mg, Si, Ca, and Ti to MIST models for both pipelines. In Figures B.5, B.6, and B.7, there is a shift in the abundances depending on which pipeline you use. In particular, the NGC 752 plot of Figure B.5 shows the pipeline using SynSpec NLTE shows greater variation in [Fe/H] near the turnoff than the pipeline using Turbospectrum 20, this can be seen as the same star between the two pipelines are connected.

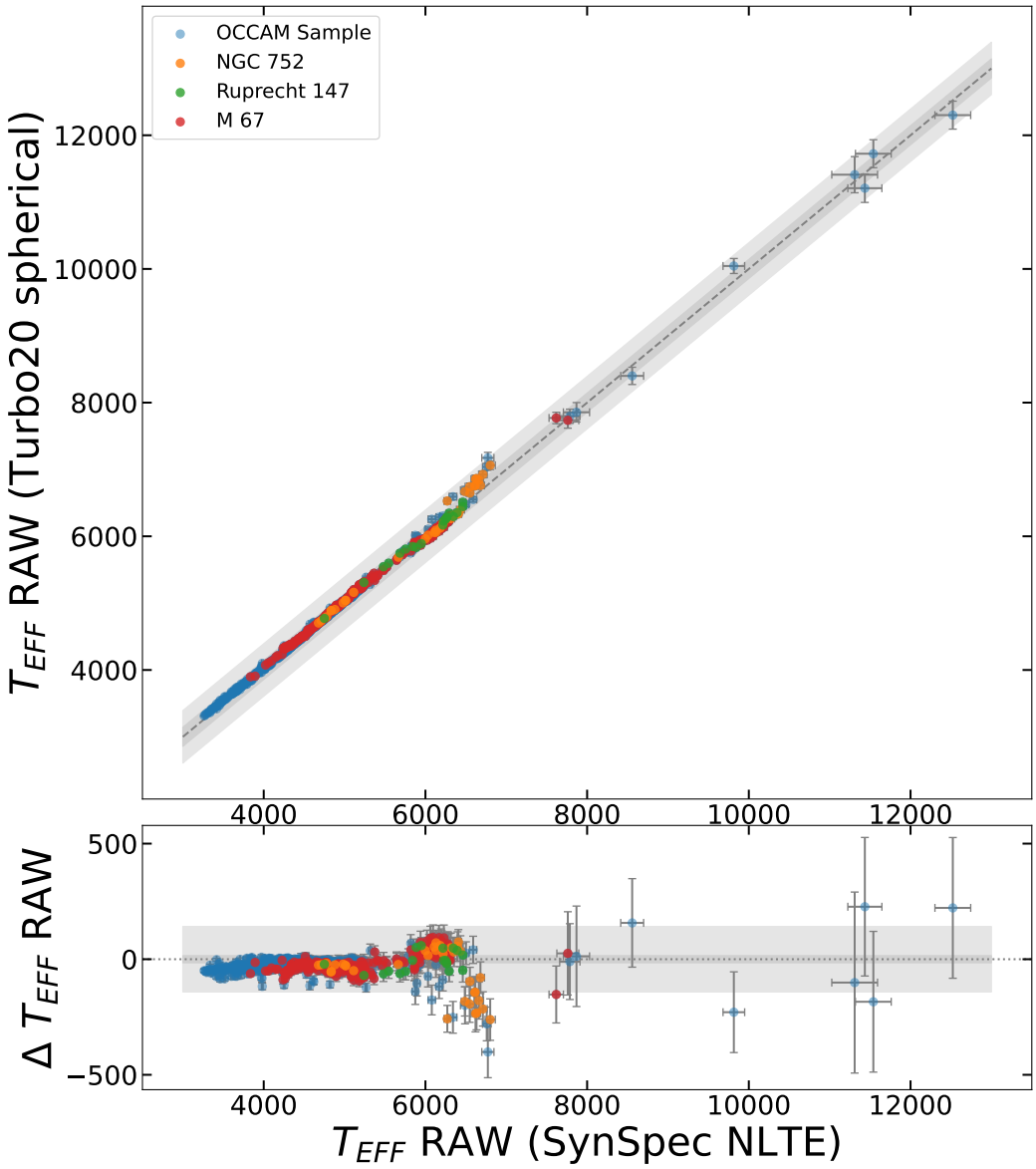

Figure B.1: This plot is comparing the calibrated T_{eff} between the alternative pipelines. The top portion is a one-one plot, while the lower portion is a delta plot, where $\Delta T_{eff} = (SSNLTE\ T_{eff}) - (Turbo20\ T_{eff})$, as a function of calibrated T_{eff} using SynSpec NLTE. The darker grey region represents median error and the larger lighter grey region represents the assumed 100K uncertianty for all the stars.

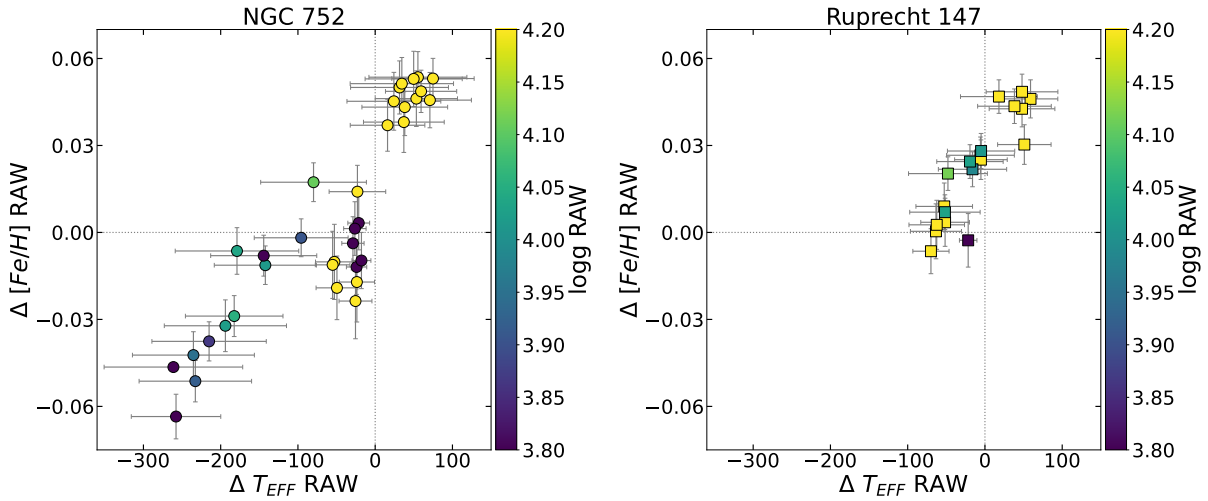

Figure B.2: $\Delta[Fe/H]$ raw values as a function of ΔT_{eff} raw values, where delta is defined as $SSNLTE - Turbo20(Sph.)$. The grey dashed vertical and horizontal lines represents where $\Delta = 0$ for both $[Fe/H]$ and T_{eff}. The markers are colored by their uncalibrated surface gravity outputted by FERRE.

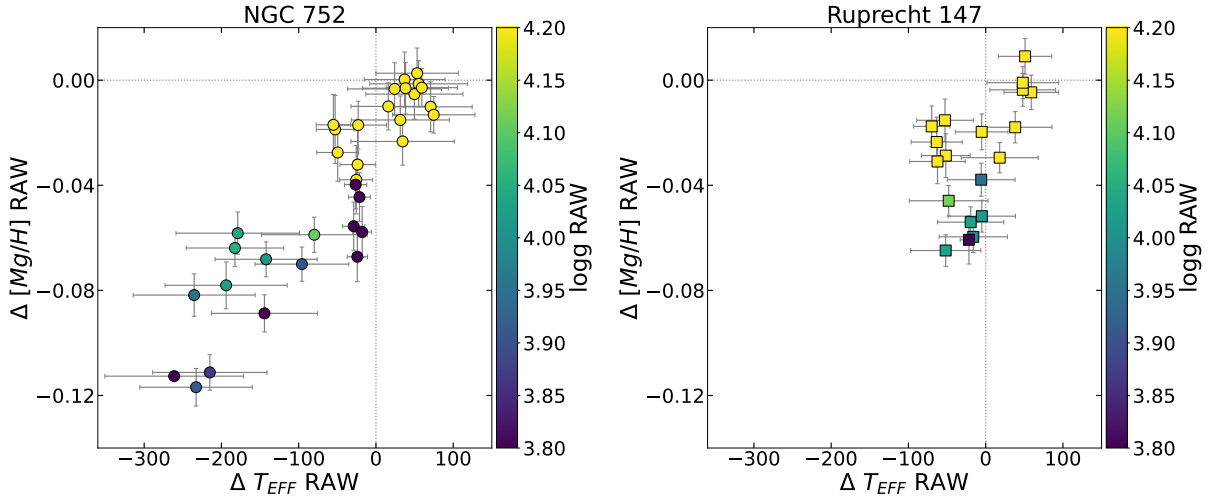

Figure B.3: $\Delta[Mg/H]$ raw valuse as a function of ΔT_{eff} raw values. Similar markings are Figure B.2.

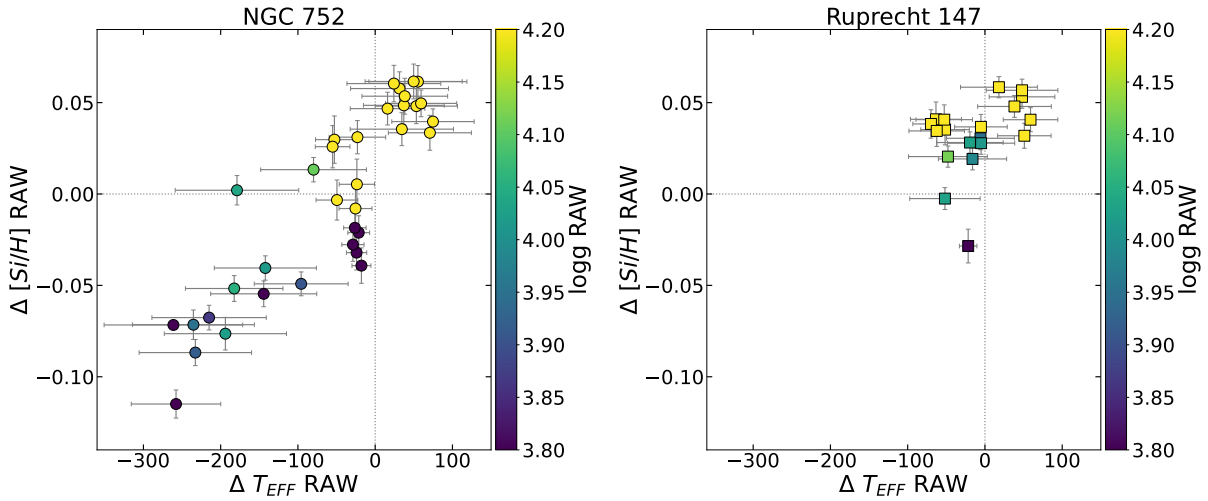

Figure B.4: $\Delta[Si/H]$ raw valuse as a function of ΔT_{eff} raw values. Similar markings are Figure B.2.

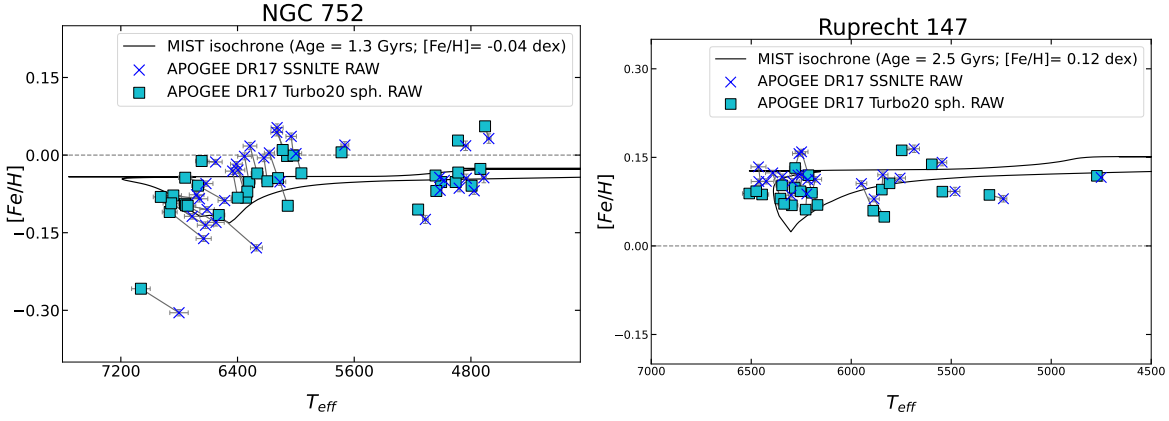

Figure B.5: This is a plot is comparing the two pipeline and see how the values change in Teff-[Fe/H] space. There is a line connecting the same star between data set.

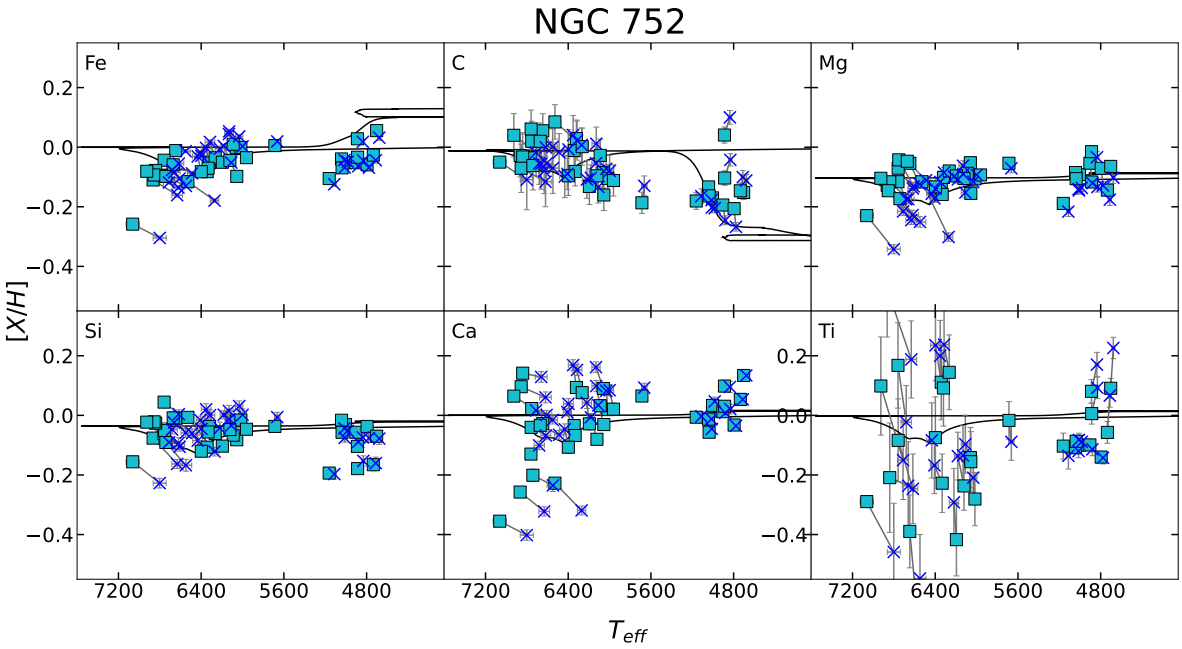

Figure B.6: Similar to Figure B.5 but for all six elements in Teff-[X/H] space.

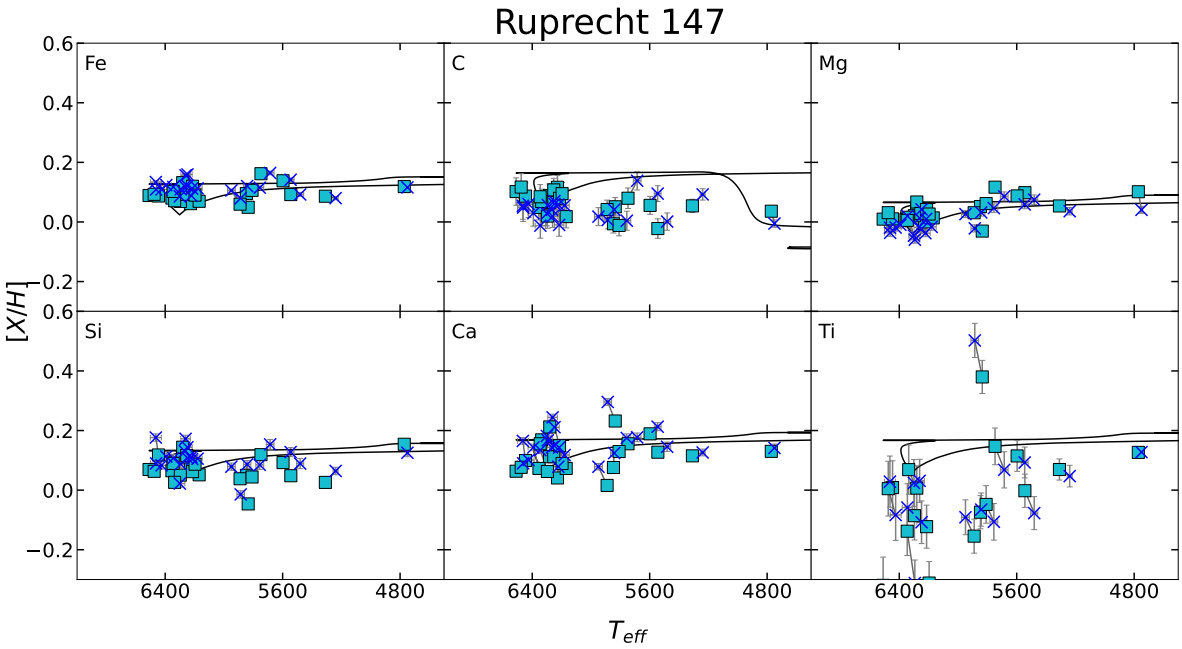

Figure B.7: Similar to Figure B.6

Appendix C

Globular Cluster & OCCAM DR17

Sample Calibration sample

Table C.1: Calibration Globular Cluster Sample Stellar Data from APOGEE DR17.

Cluster name	2MASS ID	T_{eff} (K)	log(g) (dex)	[Fe/H] (dex)	[C/N] (dex)	Red Clump
		Globular Cluster Stars				
47 TUC	2M00204027−7201425	4753 ± 12	2.46 ± 0.04	-0.69 ± 0.01	0.16 ± 0.13	N
47 TUC	2M00215813−7158147	4809 ± 15	2.46 ± 0.04	-0.71 ± 0.01	0.16 ± 0.11	N
47 TUC	2M00231815−7211516	4814 ± 16	2.39 ± 0.04	-0.76 ± 0.01	0.13 ± 0.15	N
47 TUC	2M00251382−7159103	4813 ± 15	2.37 ± 0.04	-0.79 ± 0.01	0.17 ± 0.12	N
47 TUC	2M00233065−7150017	4756 ± 12	2.36 ± 0.03	-0.70 ± 0.01	0.16 ± 0.11	N
47 TUC	2M00235608−7141488	4811 ± 15	2.39 ± 0.04	-0.75 ± 0.01	0.25 ± 0.20	N
M 71	2M19533271+1841101	4825 ± 15	2.73 ± 0.04	-0.70 ± 0.01	0.10 ± 0.07	N
M 71	2M19533114+1845204	4858 ± 16	2.63 ± 0.04	-0.71 ± 0.01	0.09 ± 0.07	N
M 71	2M19533428+1846550	4854 ± 11	2.47 ± 0.03	-0.68 ± 0.01	0.18 ± 0.13	N
M 71	2M19533989+1844229	4858 ± 10	2.45 ± 0.03	-0.72 ± 0.01	0.22 ± 0.16	N
M 71	2M19534992+1841255	4914 ± 19	2.94 ± 0.04	-0.71 ± 0.01	0.13 ± 0.09	N
M 71	2M19535769+1844567	4866 ± 16	2.61 ± 0.04	-0.68 ± 0.01	-0.22 ± 0.20	N
M 71	2M19535018+1845525	4751 ± 13	2.38 ± 0.04	-0.73 ± 0.01	0.01 ± 0.03	N
M 71	2M19540228+1842447	4772 ± 15	2.37 ± 0.04	-0.76 ± 0.01	0.07 ± 0.05	N
M 71	2M19533593+1847564	4757 ± 10	2.40 ± 0.03	-0.75 ± 0.01	-0.04 ± 0.12	N
M 4	2M16223348−2631308	5050 ± 13	2.82 ± 0.04	-1.08 ± 0.01	0.37 ± 0.26	N
M 4	2M16225050−2642162	5291 ± 16	2.28 ± 0.04	-1.22 ± 0.01	0.00 ± 0.18	N

Continued on next page

Table C.1 – Continued

Cluster name	2MASS ID	T_{eff} (K)	log(g) (dex)	[Fe/H] (dex)	[C/N] (dex) Clump	Red
M 4	2M16231475−2645281	5063 ± 14	2.98 ± 0.04	-1.05 ± 0.01	0.51 ± 0.37	N
M 4	2M16232148−2638354	5272 ± 16	2.23 ± 0.04	-1.20 ± 0.01	-0.37 ± 0.27	N
M 4	2M16233193−2631314	5397 ± 39	2.23 ± 0.06	-1.22 ± 0.02	-0.25 ± 0.47	N
M 4	2M16233236−2629222	4932 ± 12	2.62 ± 0.04	-1.05 ± 0.01	0.18 ± 0.18	N
M 4	2M16233621−2640002	4982 ± 17	2.62 ± 0.04	-1.08 ± 0.01	-0.22 ± 0.22	N
M 5	2M15175206+0159462	4994 ± 14	2.45 ± 0.04	-1.21 ± 0.01	0.22 ± 0.26	N
M 5	2M15175554+0217164	4991 ± 17	2.35 ± 0.04	-1.12 ± 0.01	-0.13 ± 0.10	N
M 5	2M15181619+0205358	5001 ± 14	2.29 ± 0.04	-1.15 ± 0.01	-0.28 ± 0.23	N
M 5	2M15182846+0159283	4866 ± 16	2.22 ± 0.05	-1.29 ± 0.01	0.16 ± 0.22	N
M 5	2M15182917+0159269	4908 ± 17	2.17 ± 0.05	-1.23 ± 0.01	-0.45 ± 0.33	N
M 5	2M15183720+0208197	4887 ± 29	2.16 ± 0.07	-1.26 ± 0.02	-0.24 ± 0.21	N
M 5	2M15183873+0208200	4890 ± 14	2.20 ± 0.04	-1.16 ± 0.01	-0.13 ± 0.09	N
M 5	2M15183915+0205301	4940 ± 19	2.37 ± 0.05	-1.23 ± 0.01	0.17 ± 0.13	N
M 5	2M15183975+0212333	4992 ± 19	2.39 ± 0.05	-1.23 ± 0.01	-0.24 ± 0.35	N
Open Cluster Stars from Spoo et al. (2022)						
Berkeley 17	2M05195385+3035095	4665 ± 9	2.60 ± 0.03	-0.12 ± 0.01	-0.23 ± 0.02	N
Berkeley 17	2M05202118+3035544	4799 ± 9	2.47 ± 0.02	-0.15 ± 0.01	-0.16 ± 0.02	N
Berkeley 17	2M05202905+3032414	4783 ± 13	2.84 ± 0.03	-0.20 ± 0.01	-0.18 ± 0.03	N
Berkeley 17	2M05203121+3035067	4820 ± 9	2.49 ± 0.02	-0.19 ± 0.01	-0.14 ± 0.02	N
Berkeley 17	2M05203650+3030351	4444 ± 6	1.98 ± 0.02	-0.17 ± 0.01	-0.15 ± 0.02	N
Berkeley 17	2M05203799+3034414	4307 ± 6	1.93 ± 0.02	-0.18 ± 0.01	-0.16 ± 0.02	N
Berkeley 17	2M05204143+3036042	4824 ± 9	2.49 ± 0.03	-0.22 ± 0.01	-0.14 ± 0.02	Y
Berkeley 17	2M05204488+3038020	4807 ± 8	2.43 ± 0.02	-0.21 ± 0.01	-0.21 ± 0.02	Y
Berkeley 18	2M05211671+4533170	4220 ± 6	1.43 ± 0.02	-0.40 ± 0.01	-0.32 ± 0.02	N
Berkeley 18	2M05214927+4525225	5126 ± 19	2.65 ± 0.04	-0.33 ± 0.01	-0.26 ± 0.05	Y
Berkeley 18	2M05215476+4526226	4309 ± 6	1.56 ± 0.03	-0.40 ± 0.01	-0.35 ± 0.02	N
Berkeley 18	2M05215704+4521220	4941 ± 17	2.38 ± 0.04	-0.38 ± 0.01	-0.57 ± 0.04	N
Berkeley 18	2M05220607+4520585	4524 ± 9	1.88 ± 0.03	-0.36 ± 0.01	-0.33 ± 0.03	N
Berkeley 18	2M05220741+4525388	4675 ± 12	2.13 ± 0.03	-0.34 ± 0.01	-0.29 ± 0.03	N
Berkeley 18	2M05221065+4528494	4425 ± 7	1.77 ± 0.03	-0.40 ± 0.01	-0.33 ± 0.02	N
Berkeley 18	2M05221426+4527000	4901 ± 15	2.20 ± 0.04	-0.41 ± 0.01	-0.27 ± 0.04	Y
Berkeley 18	2M05221874+4525191	4656 ± 12	2.08 ± 0.03	-0.36 ± 0.01	-0.33 ± 0.03	N
Berkeley 18	2M05221919+4529451	4136 ± 5	1.27 ± 0.02	-0.42 ± 0.01	-0.37 ± 0.02	N
Berkeley 18	2M05222413+4522021	4620 ± 9	1.92 ± 0.03	-0.40 ± 0.01	-0.32 ± 0.03	N
Berkeley 18	2M05222556+4525370	4686 ± 12	2.10 ± 0.03	-0.39 ± 0.01	-0.30 ± 0.03	Y
Berkeley 18	2M05222722+4520061	4961 ± 17	2.45 ± 0.04	-0.36 ± 0.01	-0.33 ± 0.05	N
Berkeley 18	2M05222848+4523173	4392 ± 6	1.72 ± 0.03	-0.38 ± 0.01	-0.35 ± 0.02	N
Berkeley 18	2M05222878+4527249	4188 ± 5	1.39 ± 0.02	-0.40 ± 0.01	-0.34 ± 0.02	N
Berkeley 18	2M05223696+4524397	4875 ± 15	2.24 ± 0.04	-0.37 ± 0.01	-0.34 ± 0.04	N
Berkeley 18	2M05224064+4523367	4189 ± 5	1.35 ± 0.03	-0.43 ± 0.01	-0.34 ± 0.02	N
Berkeley 18	2M05225704+4529067	4606 ± 13	2.01 ± 0.04	-0.35 ± 0.01	-0.36 ± 0.04	N
Berkeley 2	2M00250565+6021271	5135 ± 18	2.69 ± 0.03	-0.21 ± 0.01	-0.22 ± 0.04	Y
Berkeley 2	2M00250674+6024147	4931 ± 9	2.27 ± 0.02	-0.21 ± 0.01	-0.53 ± 0.02	N
Berkeley 2	2M00251546+6022048	4335 ± 6	1.55 ± 0.02	-0.24 ± 0.01	-0.53 ± 0.02	N
Berkeley 2	2M00251645+6021452	5083 ± 15	2.89 ± 0.03	-0.17 ± 0.01	-0.37 ± 0.04	N

Continued on next page

Table C.1 – Continued

Cluster name	2MASS ID	T_{eff} (K)	log(g) (dex)	[Fe/H] (dex)	[C/N] (dex)	Clump	Red
Berkeley 2	2M00251819+6023338	5152 ± 18	2.68 ± 0.03	-0.22 ± 0.01	-0.36 ± 0.04		N
Berkeley 2	2M00252162+6023369	5157 ± 18	2.78 ± 0.03	-0.19 ± 0.01	-0.28 ± 0.04		N
Berkeley 21	2M05513844+2147196	4534 ± 10	1.90 ± 0.03	-0.27 ± 0.01	-0.36 ± 0.03		N
Berkeley 21	2M05514277+2149599	4528 ± 11	1.94 ± 0.03	-0.26 ± 0.01	-0.36 ± 0.03		N
Berkeley 21	2M05514944+2146597	4521 ± 12	1.90 ± 0.04	-0.29 ± 0.01	-0.33 ± 0.03		Y
Berkeley 22	2M05582594+0746114	4417 ± 11	1.80 ± 0.03	-0.34 ± 0.01	-0.38 ± 0.03		N
Berkeley 22	2M05583171+0745185	4895 ± 15	2.28 ± 0.03	-0.26 ± 0.01	-1.03 ± 0.04		Y
Berkeley 22	2M05583211+0747091	4637 ± 11	2.12 ± 0.03	-0.36 ± 0.01	-0.37 ± 0.03		N
Berkeley 22	2M05583458+0744390	4898 ± 16	2.54 ± 0.04	-0.32 ± 0.01	-0.40 ± 0.04		Y
Berkeley 22	2M05583818+0745527	4133 ± 5	1.27 ± 0.02	-0.38 ± 0.01	-0.39 ± 0.02		N
Berkeley 29	2M06530386+1655157	4099 ± 8	1.19 ± 0.03	-0.51 ± 0.01	-0.29 ± 0.03		N
Berkeley 29	2M06530436+1655541	3982 ± 5	0.99 ± 0.03	-0.55 ± 0.01	-0.27 ± 0.02		N
Berkeley 31	2M06573113+0816069	3914 ± 4	0.95 ± 0.02	-0.45 ± 0.01	-0.28 ± 0.02		N
Berkeley 31	2M06573740+0815591	4629 ± 12	1.91 ± 0.03	-0.41 ± 0.01	-0.28 ± 0.03		N
Berkeley 53	2M20554232+5106153	4735 ± 7	2.32 ± 0.02	-0.09 ± 0.01	-0.47 ± 0.02		N
Berkeley 53	2M20554936+5106545	4442 ± 6	1.88 ± 0.02	-0.12 ± 0.01	-0.46 ± 0.02		N
Berkeley 53	2M20554998+5102175	4709 ± 10	2.25 ± 0.03	-0.13 ± 0.01	-0.59 ± 0.03		N
Berkeley 53	2M20555767+5103206	4933 ± 9	2.49 ± 0.02	-0.15 ± 0.01	-0.44 ± 0.02		N
Berkeley 53	2M20555959+5100466	4920 ± 16	2.56 ± 0.03	-0.15 ± 0.01	-0.56 ± 0.04		N
Berkeley 53	2M20561018+5102389	4851 ± 8	2.37 ± 0.02	-0.09 ± 0.01	-0.57 ± 0.02		N
Berkeley 66	2M03040371+5844017	4926 ± 15	2.48 ± 0.03	-0.22 ± 0.01	-0.27 ± 0.04		Y
Berkeley 66	2M03041010+5845484	4516 ± 9	2.04 ± 0.03	-0.24 ± 0.01	-0.31 ± 0.03		N
Berkeley 66	2M03041368+5843387	4925 ± 15	2.51 ± 0.03	-0.20 ± 0.01	-0.32 ± 0.04		Y
Berkeley 66	2M03042113+5845433	4118 ± 5	1.39 ± 0.02	-0.24 ± 0.01	-0.30 ± 0.02		N
Berkeley 66	2M03043163+5844477	4440 ± 10	1.93 ± 0.03	-0.21 ± 0.01	-0.30 ± 0.03		N
Berkeley 71	2M05404312+3217303	5210 ± 11	3.10 ± 0.02	-0.23 ± 0.01	-0.48 ± 0.03		N
Berkeley 71	2M05405442+3217298	5183 ± 11	2.75 ± 0.02	-0.23 ± 0.01	-0.52 ± 0.03		N
Berkeley 71	2M05405484+3215567	5231 ± 15	2.81 ± 0.03	-0.24 ± 0.01	-0.66 ± 0.04		N
Berkeley 71	2M05405503+3214099	5212 ± 12	2.86 ± 0.03	-0.24 ± 0.01	-0.55 ± 0.03		N
Berkeley 71	2M05405956+3215182	5187 ± 14	2.88 ± 0.03	-0.22 ± 0.01	-0.49 ± 0.03		N
Berkeley 75	2M06485504−2359271	4376 ± 7	1.58 ± 0.03	-0.42 ± 0.01	-0.43 ± 0.02		N
Berkeley 75	2M06490297−2359294	5010 ± 17	2.41 ± 0.04	-0.39 ± 0.01	-0.50 ± 0.05		N
Berkeley 75	2M06491539−2359187	4979 ± 17	2.39 ± 0.04	-0.41 ± 0.01	-0.59 ± 0.05		Y
Berkeley 85	2M20183476+3740565	4380 ± 5	1.91 ± 0.02	0.09 ± 0.01	-0.42 ± 0.01		N
Berkeley 85	2M20183785+3743009	4336 ± 5	1.87 ± 0.02	0.12 ± 0.01	-0.42 ± 0.01		N
Berkeley 85	2M20184444+3747447	4822 ± 9	2.70 ± 0.02	0.01 ± 0.01	-0.43 ± 0.02		Y
Berkeley 85	2M20184497+3744174	4262 ± 5	1.77 ± 0.02	0.09 ± 0.01	-0.38 ± 0.01		N
Berkeley 85	2M20184563+3742464	4834 ± 8	3.05 ± 0.02	-0.02 ± 0.01	-0.42 ± 0.02		N
Berkeley 85	2M20184620+3744194	4449 ± 6	2.00 ± 0.02	0.11 ± 0.01	-0.46 ± 0.01		N
Berkeley 85	2M20185346+3745129	4174 ± 8	1.54 ± 0.03	0.04 ± 0.01	-0.36 ± 0.02		N
Berkeley 85	2M20185602+3740479	4853 ± 8	2.77 ± 0.02	-0.01 ± 0.01	-0.40 ± 0.02		Y
Berkeley 85	2M20185677+3747580	4891 ± 8	3.08 ± 0.02	0.01 ± 0.01	-0.40 ± 0.02		N
Berkeley 85	2M20190397+3745002	4411 ± 6	1.99 ± 0.02	0.09 ± 0.01	-0.43 ± 0.01		N
Berkeley 98	2M22423380+5226576	4652 ± 12	2.41 ± 0.03	-0.07 ± 0.01	-0.38 ± 0.03		Y
Berkeley 98	2M22423502+5222084	4577 ± 10	2.38 ± 0.03	-0.03 ± 0.01	-0.38 ± 0.02		N

Continued on next page

Table C.1 – Continued

Cluster name	2MASS ID	T_{eff} (K)	log(g) (dex)	[Fe/H] (dex)	[C/N] (dex)	Red Clump
Berkeley 98	2M22424107+5225224	5014 ± 13	2.65 ± 0.03	-0.04 ± 0.01	-0.53 ± 0.03	N
Berkeley 98	2M22425469+5227482	4837 ± 11	2.63 ± 0.03	-0.04 ± 0.01	-0.26 ± 0.03	Y
Berkeley 98	2M22430145+5226205	4839 ± 12	2.64 ± 0.03	-0.05 ± 0.01	-0.26 ± 0.03	N
Czernik 20	2M05201330+3931005	5108 ± 17	2.83 ± 0.03	-0.18 ± 0.01	-0.40 ± 0.04	N
Czernik 20	2M05202738+3930571	5129 ± 15	2.97 ± 0.03	-0.16 ± 0.01	-0.32 ± 0.04	N
Czernik 20	2M05202775+3932378	5123 ± 18	3.05 ± 0.03	-0.18 ± 0.01	-0.40 ± 0.04	N
Czernik 20	2M05204153+3934173	5099 ± 16	2.84 ± 0.03	-0.19 ± 0.01	-0.59 ± 0.04	N
Czernik 21	2M05263726+3600404	5012 ± 12	2.68 ± 0.03	-0.32 ± 0.01	-0.27 ± 0.03	N
Czernik 21	2M05264047+3602191	4920 ± 14	2.58 ± 0.03	-0.33 ± 0.01	-0.29 ± 0.04	N
Czernik 30	2M07310830−0956359	4419 ± 7	1.76 ± 0.03	-0.39 ± 0.01	-0.37 ± 0.02	N
Czernik 30	2M07311590−0955415	4580 ± 11	2.06 ± 0.03	-0.39 ± 0.01	-0.32 ± 0.03	N
ESO 211 03	2M08512078−5017501	5140 ± 18	2.90 ± 0.03	-0.14 ± 0.01	-0.52 ± 0.04	N
ESO 211 03	2M08512256−5016382	5164 ± 16	2.84 ± 0.03	-0.14 ± 0.01	-0.50 ± 0.04	N
ESO 211 03	2M08512262−5014009	5156 ± 15	2.74 ± 0.03	-0.18 ± 0.01	-0.55 ± 0.04	N
ESO 211 03	2M08512802−5013308	5124 ± 15	2.89 ± 0.03	-0.21 ± 0.01	-0.37 ± 0.04	N
ESO 211 03	2M08513338−5016060	5188 ± 16	2.88 ± 0.03	-0.11 ± 0.01	-0.51 ± 0.04	Y
ESO 211 03	2M08513366−5014516	5202 ± 17	2.92 ± 0.03	-0.16 ± 0.01	-0.71 ± 0.04	N
ESO 211 03	2M08513535−5012106	5058 ± 12	2.62 ± 0.03	-0.15 ± 0.01	-0.56 ± 0.03	Y
ESO 211 03	2M08513726−5013252	5096 ± 14	2.64 ± 0.03	-0.17 ± 0.01	-0.50 ± 0.03	N
ESO 211 03	2M08513967−5011330	5188 ± 17	2.93 ± 0.03	-0.14 ± 0.01	-0.47 ± 0.04	Y
ESO 211 03	2M08513973−5015079	5150 ± 14	2.73 ± 0.03	-0.17 ± 0.01	-0.60 ± 0.03	Y
ESO 211 03	2M08514065−5016095	5160 ± 15	2.77 ± 0.03	-0.18 ± 0.01	-0.60 ± 0.04	N
ESO 211 03	2M08514067−5017226	5137 ± 17	2.82 ± 0.03	-0.20 ± 0.01	-0.49 ± 0.04	Y
ESO 211 03	2M08514660−5016233	5119 ± 14	2.73 ± 0.03	-0.20 ± 0.01	-0.54 ± 0.03	Y
ESO 211 03	2M08515153−5017362	5177 ± 16	2.90 ± 0.03	-0.16 ± 0.01	-0.50 ± 0.04	N
ESO 211 03	2M08515806−5015416	5166 ± 17	2.83 ± 0.03	-0.18 ± 0.01	-0.43 ± 0.04	Y
ESO 518 03	2M16464504−2558201	4162 ± 5	1.65 ± 0.02	0.05 ± 0.01	-0.36 ± 0.01	N
ESO 518 03	2M16465144−2546306	4773 ± 7	2.57 ± 0.02	0.17 ± 0.01	-0.45 ± 0.02	N
ESO 518 03	2M16470166−2547374	4805 ± 8	2.71 ± 0.02	0.09 ± 0.01	-0.44 ± 0.02	N
ESO 518 03	2M16472991−2544594	4786 ± 8	2.55 ± 0.02	0.12 ± 0.01	-0.53 ± 0.02	N
FSR 0494	2M00253373+6345239	5070 ± 16	2.85 ± 0.03	-0.02 ± 0.01	-0.55 ± 0.04	N
FSR 0494	2M00253400+6346574	5090 ± 17	2.83 ± 0.03	-0.02 ± 0.01	-0.51 ± 0.04	Y
FSR 0494	2M00253826+6344101	5125 ± 17	3.00 ± 0.03	-0.01 ± 0.01	-0.52 ± 0.04	Y
FSR 0494	2M00255011+6343565	5120 ± 17	2.92 ± 0.03	0.03 ± 0.01	-0.51 ± 0.04	Y
FSR 0494	2M00260027+6343287	5101 ± 18	2.91 ± 0.03	-0.04 ± 0.01	-0.45 ± 0.04	Y
FSR 0937	2M06133791+1500575	4242 ± 6	1.30 ± 0.02	-0.39 ± 0.01	-0.48 ± 0.02	N
FSR 0937	2M06135003+1502266	5087 ± 15	2.68 ± 0.03	-0.35 ± 0.01	-0.39 ± 0.04	N
IC 166	2M01514975+6150556	5167 ± 18	2.97 ± 0.03	-0.08 ± 0.01	-0.55 ± 0.04	N
IC 166	2M01515473+6148552	5145 ± 18	2.93 ± 0.03	-0.09 ± 0.01	-0.51 ± 0.04	N
IC 166	2M01520006+6153008	5151 ± 17	2.95 ± 0.03	-0.03 ± 0.01	-0.44 ± 0.04	N
IC 166	2M01521509+6151407	5113 ± 16	2.85 ± 0.03	-0.08 ± 0.01	-0.57 ± 0.04	Y
IC 166	2M01522060+6150364	5184 ± 20	3.06 ± 0.03	-0.06 ± 0.01	-0.44 ± 0.04	N
IC 166	2M01522077+6153186	5341 ± 20	2.95 ± 0.03	-0.09 ± 0.01	-0.78 ± 0.04	N
IC 166	2M01522357+6154011	5152 ± 19	2.91 ± 0.03	-0.10 ± 0.01	-0.49 ± 0.04	N
IC 166	2M01522953+6151427	4851 ± 11	2.53 ± 0.03	-0.10 ± 0.01	-0.33 ± 0.03	N

Continued on next page

Table C.1 – Continued

Cluster name	2MASS ID	T_{eff} (K)	log(g) (dex)	[Fe/H] (dex)	[C/N] (dex)	Clump	Red
IC 166	2M01523324+6152050	5200 ± 20	3.00 ± 0.03	-0.10 ± 0.01	-0.49 ± 0.04		N
IC 166	2M01523513+6154318	5162 ± 16	2.94 ± 0.03	-0.11 ± 0.01	-0.62 ± 0.04		N
IC 166	2M01524136+6151507	5166 ± 20	3.00 ± 0.03	-0.08 ± 0.01	-0.49 ± 0.04		N
IC 166	2M01524515+6153369	5141 ± 16	3.00 ± 0.03	-0.12 ± 0.01	-0.24 ± 0.04		N
IC 166	2M01525543+6148504	5049 ± 15	2.71 ± 0.03	-0.10 ± 0.01	-0.33 ± 0.04		N
King 5	2M03140915+5237511	5125 ± 11	2.89 ± 0.02	-0.14 ± 0.01	-0.44 ± 0.03		N
King 5	2M03142548+5247355	4306 ± 6	1.62 ± 0.02	-0.18 ± 0.01	-0.47 ± 0.02		N
King 5	2M03142784+5242408	5075 ± 10	2.75 ± 0.02	-0.14 ± 0.01	-0.51 ± 0.02		N
King 5	2M03154012+5242565	5063 ± 13	3.01 ± 0.03	-0.18 ± 0.01	-0.46 ± 0.03		N
Melotte 71	2M07372210−1205264	5129 ± 10	3.11 ± 0.02	-0.15 ± 0.01	-0.44 ± 0.03		N
Melotte 71	2M07373589−1205094	5068 ± 10	2.75 ± 0.02	-0.17 ± 0.01	-0.48 ± 0.02		N
Melotte 71	2M07374269−1207058	5115 ± 10	2.81 ± 0.02	-0.13 ± 0.01	-0.52 ± 0.02		N
NGC 1193	2M03060593+4421203	4740 ± 12	2.37 ± 0.03	-0.34 ± 0.01	-0.18 ± 0.03		Y
NGC 1193	2M03060785+4425167	3954 ± 4	1.08 ± 0.02	-0.37 ± 0.01	-0.28 ± 0.02		N
NGC 1193	2M03060808+4423347	4779 ± 14	2.53 ± 0.04	-0.34 ± 0.01	-0.25 ± 0.04		N
NGC 1245	2M03135098+4722010	5124 ± 13	2.89 ± 0.03	-0.05 ± 0.01	-0.49 ± 0.03		N
NGC 1245	2M03140839+4716330	5153 ± 15	2.97 ± 0.03	-0.09 ± 0.01	-0.47 ± 0.03		N
NGC 1245	2M03141134+4709173	4575 ± 7	2.02 ± 0.02	-0.16 ± 0.01	-0.48 ± 0.02		Y
NGC 1245	2M03141268+4717315	5146 ± 12	2.89 ± 0.03	-0.11 ± 0.01	-0.55 ± 0.03		N
NGC 1245	2M03142464+4711327	5155 ± 14	2.99 ± 0.03	-0.10 ± 0.01	-0.49 ± 0.03		N
NGC 1245	2M03143100+4714204	5148 ± 13	2.93 ± 0.03	-0.08 ± 0.01	-0.59 ± 0.03		N
NGC 1245	2M03143256+4716277	5156 ± 13	2.93 ± 0.03	-0.10 ± 0.01	-0.41 ± 0.03		N
NGC 1245	2M03143819+4720444	5116 ± 10	2.87 ± 0.02	-0.08 ± 0.01	-0.48 ± 0.02		N
NGC 1245	2M03143888+4718202	5150 ± 14	2.96 ± 0.03	-0.10 ± 0.01	-0.30 ± 0.03		N
NGC 1245	2M03143977+4714400	5103 ± 12	2.86 ± 0.03	-0.09 ± 0.01	-0.57 ± 0.03		N
NGC 1245	2M03144021+4715280	5135 ± 12	2.93 ± 0.02	-0.08 ± 0.01	-0.43 ± 0.03		N
NGC 1245	2M03144698+4711579	5143 ± 13	3.02 ± 0.03	-0.10 ± 0.01	-0.29 ± 0.03		N
NGC 1245	2M03145265+4719245	5144 ± 13	2.91 ± 0.03	-0.12 ± 0.01	-0.36 ± 0.03		N
NGC 1245	2M03145273+4714033	5177 ± 12	2.97 ± 0.03	-0.07 ± 0.01	-0.48 ± 0.03		N
NGC 1245	2M03145518+4712146	5153 ± 12	2.97 ± 0.02	-0.06 ± 0.01	-0.44 ± 0.03		N
NGC 1245	2M03145841+4708245	5170 ± 13	2.96 ± 0.03	-0.12 ± 0.01	-0.55 ± 0.03		N
NGC 1245	2M03145950+4721138	5124 ± 12	2.98 ± 0.03	-0.04 ± 0.01	-0.40 ± 0.03		N
NGC 1245	2M03150241+4719582	5144 ± 14	2.96 ± 0.03	-0.09 ± 0.01	-0.59 ± 0.03		N
NGC 1245	2M03150510+4714411	5144 ± 14	3.00 ± 0.03	-0.06 ± 0.01	-0.36 ± 0.03		N
NGC 1245	2M03150614+4716352	5110 ± 12	2.94 ± 0.03	-0.10 ± 0.01	-0.58 ± 0.03		N
NGC 1245	2M03151244+4708556	5151 ± 13	2.97 ± 0.03	-0.08 ± 0.01	-0.57 ± 0.03		N
NGC 1245	2M03151253+4717291	5139 ± 12	2.96 ± 0.03	-0.06 ± 0.01	-0.43 ± 0.03		N
NGC 1245	2M03151560+4714338	5138 ± 12	2.88 ± 0.03	-0.13 ± 0.01	-0.55 ± 0.03		N
NGC 1245	2M03151881+4712051	5148 ± 12	2.93 ± 0.03	-0.09 ± 0.01	-0.53 ± 0.03		N
NGC 1245	2M03151975+4713477	5131 ± 12	2.88 ± 0.02	-0.08 ± 0.01	-0.42 ± 0.03		Y
NGC 1798	2M05112383+4742003	4840 ± 13	2.36 ± 0.03	-0.28 ± 0.01	-0.38 ± 0.03		Y
NGC 1798	2M05112446+4740027	4517 ± 7	1.86 ± 0.03	-0.30 ± 0.01	-0.44 ± 0.02		N
NGC 1798	2M05113450+4741177	5105 ± 17	2.76 ± 0.03	-0.26 ± 0.01	-0.36 ± 0.04		N
NGC 1798	2M05113666+4741482	4733 ± 9	2.13 ± 0.03	-0.29 ± 0.01	-0.47 ± 0.02		Y
NGC 1798	2M05113768+4742329	4812 ± 11	2.31 ± 0.03	-0.29 ± 0.01	-0.29 ± 0.03		Y

Continued on next page

Table C.1 – Continued

Cluster name	2MASS ID	T_{eff} (K)	log(g) (dex)	[Fe/H] (dex)	[C/N] (dex)	Clump	Red
NGC 1798	2M05114006+4739238	4742 ± 8	2.16 ± 0.02	-0.27 ± 0.01	-0.46 ± 0.02		N
NGC 1798	2M05114134+4740406	4856 ± 13	2.43 ± 0.03	-0.27 ± 0.01	-0.35 ± 0.03		N
NGC 1798	2M05114422+4741517	5125 ± 18	2.81 ± 0.04	-0.25 ± 0.01	-0.43 ± 0.04		N
NGC 1798	2M05114626+4743422	4691 ± 9	2.16 ± 0.03	-0.28 ± 0.01	-0.44 ± 0.02		N
NGC 1798	2M05114795+4740258	3991 ± 5	1.01 ± 0.02	-0.35 ± 0.01	-0.42 ± 0.02		N
NGC 1817	2M05114991+1650417	5134 ± 10	2.85 ± 0.02	-0.16 ± 0.01	-0.60 ± 0.03		N
NGC 1817	2M05122932+1635549	5150 ± 16	3.15 ± 0.03	-0.12 ± 0.01	-0.32 ± 0.04		N
NGC 1817	2M05125364+1649336	5088 ± 10	2.82 ± 0.02	-0.14 ± 0.01	-0.51 ± 0.02		N
NGC 1817	2M05130181+1641144	4760 ± 12	2.38 ± 0.03	-0.18 ± 0.01	-0.38 ± 0.03		Y
NGC 1817	2M05134177+1643290	5096 ± 10	2.78 ± 0.02	-0.17 ± 0.01	-0.40 ± 0.03		N
NGC 188	2M00320079+8511465	4506 ± 6	2.42 ± 0.02	0.07 ± 0.01	-0.19 ± 0.02		N
NGC 188	2M00350924+8517169	4672 ± 7	2.38 ± 0.02	0.05 ± 0.01	-0.25 ± 0.02		Y
NGC 188	2M00411980+8501269	4723 ± 7	2.85 ± 0.02	0.08 ± 0.01	-0.26 ± 0.02		N
NGC 188	2M00415197+8527070	4660 ± 7	2.40 ± 0.02	0.08 ± 0.01	-0.26 ± 0.02		Y
NGC 188	2M00420095+8516249	4876 ± 10	3.29 ± 0.02	0.11 ± 0.01	-0.24 ± 0.02		N
NGC 188	2M00422316+8520336	4868 ± 10	3.18 ± 0.02	0.04 ± 0.01	-0.20 ± 0.02		N
NGC 188	2M00422570+8516219	4634 ± 7	2.67 ± 0.02	0.05 ± 0.01	-0.25 ± 0.02		N
NGC 188	2M00441241+8509312	4058 ± 4	1.56 ± 0.02	-0.01 ± 0.01	-0.17 ± 0.01		N
NGC 188	2M00444460+8532163	4809 ± 7	3.11 ± 0.02	0.13 ± 0.01	-0.19 ± 0.02		N
NGC 188	2M00445253+8514055	4437 ± 6	2.22 ± 0.02	0.04 ± 0.01	-0.21 ± 0.01		N
NGC 188	2M00453697+8515084	4762 ± 7	2.94 ± 0.02	0.07 ± 0.01	-0.27 ± 0.02		N
NGC 188	2M00455119+8518082	4461 ± 6	2.31 ± 0.02	0.05 ± 0.01	-0.19 ± 0.01		N
NGC 188	2M00463004+8511518	4845 ± 8	3.23 ± 0.02	0.07 ± 0.01	-0.22 ± 0.02		N
NGC 188	2M00463374+8514342	4795 ± 7	3.10 ± 0.02	0.11 ± 0.01	-0.28 ± 0.02		N
NGC 188	2M00463920+8523336	4387 ± 6	2.12 ± 0.02	0.04 ± 0.01	-0.43 ± 0.01		N
NGC 188	2M00465966+8513157	4650 ± 7	2.38 ± 0.02	0.04 ± 0.01	-0.23 ± 0.02		Y
NGC 188	2M00471847+8519456	4594 ± 6	2.54 ± 0.02	0.05 ± 0.01	-0.27 ± 0.02		N
NGC 188	2M00472975+8524140	4701 ± 7	2.67 ± 0.02	0.11 ± 0.01	-0.43 ± 0.02		N
NGC 188	2M00473222+8511024	4860 ± 9	3.20 ± 0.02	0.10 ± 0.01	-0.21 ± 0.02		N
NGC 188	2M00485910+8512294	4763 ± 7	2.98 ± 0.02	0.08 ± 0.01	-0.26 ± 0.02		N
NGC 188	2M00490560+8526077	4533 ± 6	2.44 ± 0.02	0.06 ± 0.01	-0.21 ± 0.02		N
NGC 188	2M00512176+8512377	4705 ± 7	2.76 ± 0.02	0.06 ± 0.01	-0.29 ± 0.02		N
NGC 188	2M00533497+8511145	4705 ± 7	2.80 ± 0.02	0.04 ± 0.01	-0.25 ± 0.02		N
NGC 188	2M00533572+8520583	4587 ± 6	2.58 ± 0.02	0.08 ± 0.01	-0.30 ± 0.02		N
NGC 188	2M00541152+8515231	4673 ± 7	2.41 ± 0.02	0.06 ± 0.01	-0.21 ± 0.02		Y
NGC 188	2M00542287+8455398	4830 ± 8	3.12 ± 0.02	0.05 ± 0.01	-0.25 ± 0.02		N
NGC 188	2M00543664+8501152	4680 ± 7	2.39 ± 0.02	0.08 ± 0.01	-0.28 ± 0.02		Y
NGC 188	2M00571844+8510288	4631 ± 7	2.41 ± 0.02	0.09 ± 0.01	-0.24 ± 0.02		Y
NGC 188	2M00581691+8540183	4662 ± 7	2.44 ± 0.02	0.10 ± 0.01	-0.23 ± 0.02		Y
NGC 188	2M01003483+8503198	4837 ± 8	3.15 ± 0.02	0.08 ± 0.01	-0.26 ± 0.02		N
NGC 188	2M01015206+8506329	4099 ± 4	1.65 ± 0.02	0.05 ± 0.01	-0.19 ± 0.01		N
NGC 188	2M01025280+8517563	4512 ± 6	2.37 ± 0.02	0.03 ± 0.01	-0.22 ± 0.02		N
NGC 1907	2M05274905+3520101	5095 ± 10	2.89 ± 0.02	-0.13 ± 0.01	-0.51 ± 0.02		N
NGC 1907	2M05280420+3519163	4948 ± 9	2.49 ± 0.02	-0.13 ± 0.01	-0.64 ± 0.02		N
NGC 1907	2M05281205+3520195	5128 ± 10	2.98 ± 0.02	-0.12 ± 0.01	-0.44 ± 0.02		N

Continued on next page

Table C.1 – Continued

Cluster name	2MASS ID	T_{eff} (K)	log(g) (dex)	[Fe/H] (dex)	[C/N] (dex)	Clump	Red
NGC 2158	2M06070510+2404469	4668 ± 8	2.11 ± 0.02	-0.26 ± 0.01	-0.42 ± 0.02		Y
NGC 2158	2M06071310+2405474	5022 ± 15	2.61 ± 0.03	-0.25 ± 0.01	-0.28 ± 0.04		N
NGC 2158	2M06071407+2406547	4429 ± 6	1.68 ± 0.02	-0.29 ± 0.01	-0.50 ± 0.02		N
NGC 2158	2M06071494+2407517	4569 ± 8	2.06 ± 0.03	-0.24 ± 0.01	-0.36 ± 0.02		N
NGC 2158	2M06071553+2409479	5117 ± 16	3.00 ± 0.03	-0.25 ± 0.01	-0.26 ± 0.04		Y
NGC 2158	2M06071664+2405284	4537 ± 9	1.96 ± 0.03	-0.25 ± 0.01	-0.40 ± 0.03		N
NGC 2158	2M06071696+2402007	4949 ± 16	2.58 ± 0.04	-0.20 ± 0.01	-0.21 ± 0.04		Y
NGC 2158	2M06071764+2410276	5070 ± 16	2.58 ± 0.03	-0.27 ± 0.01	-0.42 ± 0.04		Y
NGC 2158	2M06071787+2405542	4447 ± 6	1.90 ± 0.02	-0.23 ± 0.01	-0.36 ± 0.02		N
NGC 2158	2M06071884+2401400	5176 ± 19	3.08 ± 0.04	-0.24 ± 0.01	-0.24 ± 0.05		N
NGC 2158	2M06072149+2404559	4755 ± 12	2.35 ± 0.03	-0.25 ± 0.01	-0.38 ± 0.03		N
NGC 2158	2M06072194+2404169	5182 ± 16	2.97 ± 0.03	-0.25 ± 0.01	-0.35 ± 0.04		N
NGC 2158	2M06072254+2407093	4970 ± 12	2.53 ± 0.03	-0.27 ± 0.01	-0.33 ± 0.03		N
NGC 2158	2M06072333+2402417	4876 ± 16	2.69 ± 0.04	-0.20 ± 0.01	-0.30 ± 0.04		N
NGC 2158	2M06072443+2400524	4906 ± 15	2.55 ± 0.03	-0.26 ± 0.01	-0.34 ± 0.04		Y
NGC 2158	2M06072582+2407472	5013 ± 17	2.71 ± 0.04	-0.29 ± 0.01	-0.14 ± 0.04		N
NGC 2158	2M06072594+2402252	4796 ± 12	2.44 ± 0.03	-0.23 ± 0.01	-0.26 ± 0.03		Y
NGC 2158	2M06072597+2406079	5132 ± 18	3.27 ± 0.04	-0.25 ± 0.01	-0.13 ± 0.05		N
NGC 2158	2M06072624+2409568	4997 ± 16	2.73 ± 0.03	-0.23 ± 0.01	-0.19 ± 0.04		N
NGC 2158	2M06072676+2404394	5018 ± 16	2.95 ± 0.03	-0.21 ± 0.01	-0.30 ± 0.04		N
NGC 2158	2M06072822+2408020	5078 ± 14	2.74 ± 0.03	-0.24 ± 0.01	-0.40 ± 0.04		N
NGC 2158	2M06072907+2402151	4945 ± 13	2.60 ± 0.03	-0.20 ± 0.01	-0.42 ± 0.03		Y
NGC 2158	2M06072918+2408185	4993 ± 13	2.60 ± 0.03	-0.24 ± 0.01	-0.44 ± 0.03		N
NGC 2158	2M06072940+2408441	5017 ± 15	2.73 ± 0.03	-0.19 ± 0.01	-0.29 ± 0.04		N
NGC 2158	2M06073032+2407227	4928 ± 12	2.49 ± 0.03	-0.28 ± 0.01	-0.48 ± 0.03		Y
NGC 2158	2M06073145+2403076	4991 ± 17	2.97 ± 0.04	-0.24 ± 0.01	-0.28 ± 0.04		N
NGC 2158	2M06073211+2409457	4823 ± 12	2.52 ± 0.03	-0.26 ± 0.01	-0.30 ± 0.03		Y
NGC 2158	2M06073232+2404361	5101 ± 17	2.98 ± 0.03	-0.25 ± 0.01	-0.34 ± 0.04		N
NGC 2158	2M06073636+2405001	4986 ± 15	2.68 ± 0.03	-0.23 ± 0.01	-0.36 ± 0.04		Y
NGC 2158	2M06073638+2403137	4986 ± 14	2.53 ± 0.03	-0.27 ± 0.01	-0.42 ± 0.04		N
NGC 2158	2M06073652+2407000	5008 ± 16	2.57 ± 0.03	-0.26 ± 0.01	-0.36 ± 0.04		N
NGC 2158	2M06073794+2403315	5003 ± 16	2.59 ± 0.03	-0.24 ± 0.01	-0.30 ± 0.04		N
NGC 2158	2M06073917+2409098	4982 ± 15	2.57 ± 0.03	-0.21 ± 0.01	-0.38 ± 0.04		N
NGC 2158	2M06073998+2403546	4961 ± 14	2.59 ± 0.03	-0.26 ± 0.01	-0.39 ± 0.04		Y
NGC 2158	2M06074028+2408430	5172 ± 19	3.18 ± 0.04	-0.22 ± 0.01	-0.29 ± 0.05		N
NGC 2158	2M06074162+2405540	4905 ± 14	2.54 ± 0.03	-0.25 ± 0.01	-0.32 ± 0.04		Y
NGC 2158	2M06074219+2403305	4943 ± 14	2.49 ± 0.03	-0.22 ± 0.01	-0.39 ± 0.04		N
NGC 2158	2M06074272+2402514	4993 ± 15	2.60 ± 0.03	-0.29 ± 0.01	-0.35 ± 0.04		N
NGC 2158	2M06074437+2405053	5002 ± 14	2.86 ± 0.03	-0.24 ± 0.01	-0.27 ± 0.04		N
NGC 2158	2M06074629+2406533	5013 ± 14	2.72 ± 0.03	-0.22 ± 0.01	-0.27 ± 0.04		Y
NGC 2158	2M06074904+2404398	4787 ± 11	2.34 ± 0.03	-0.28 ± 0.01	-0.32 ± 0.03		Y
NGC 2204	2M06145122−1842463	4933 ± 16	2.62 ± 0.04	-0.25 ± 0.01	-0.48 ± 0.04		Y
NGC 2204	2M06145845−1838429	4285 ± 6	1.44 ± 0.02	-0.32 ± 0.01	-0.47 ± 0.02		N
NGC 2204	2M06150387−1841076	4965 ± 13	2.55 ± 0.03	-0.28 ± 0.01	-0.37 ± 0.03		N
NGC 2204	2M06151360−1841498	4941 ± 12	2.41 ± 0.03	-0.30 ± 0.01	-0.44 ± 0.03		Y

Continued on next page

Table C.1 – Continued

Cluster name	2MASS ID	T_{eff} (K)	log(g) (dex)	[Fe/H] (dex)	[C/N] (dex)	Red Clump
NGC 2204	2M06152020−1837581	5024 ± 15	2.65 ± 0.03	-0.27 ± 0.01	-0.41 ± 0.04	N
NGC 2204	2M06152142−1835512	4712 ± 8	2.09 ± 0.02	-0.26 ± 0.01	-0.58 ± 0.02	Y
NGC 2204	2M06152617−1831462	4996 ± 13	2.56 ± 0.03	-0.25 ± 0.01	-0.41 ± 0.03	N
NGC 2204	2M06153043−1838239	4764 ± 9	2.31 ± 0.03	-0.28 ± 0.01	-0.42 ± 0.02	N
NGC 2204	2M06153140−1842562	4073 ± 5	1.14 ± 0.02	-0.33 ± 0.01	-0.43 ± 0.02	N
NGC 2204	2M06153192−1839369	4533 ± 7	1.79 ± 0.02	-0.31 ± 0.01	-0.48 ± 0.02	N
NGC 2204	2M06153393−1837216	4714 ± 8	2.12 ± 0.02	-0.28 ± 0.01	-0.45 ± 0.02	N
NGC 2204	2M06153589−1841098	4765 ± 12	2.31 ± 0.03	-0.27 ± 0.01	-0.36 ± 0.03	N
NGC 2204	2M06153666−1846527	3904 ± 4	0.87 ± 0.02	-0.36 ± 0.01	-0.37 ± 0.02	N
NGC 2204	2M06153696−1836091	4989 ± 13	2.52 ± 0.03	-0.29 ± 0.01	-0.42 ± 0.03	N
NGC 2204	2M06154038−1846370	4498 ± 7	1.84 ± 0.02	-0.30 ± 0.01	-0.46 ± 0.02	N
NGC 2204	2M06154536−1843351	4986 ± 12	2.53 ± 0.03	-0.25 ± 0.01	-0.61 ± 0.03	N
NGC 2204	2M06154970−1837393	4577 ± 7	1.88 ± 0.02	-0.30 ± 0.01	-0.49 ± 0.02	N
NGC 2204	2M06155099−1834182	4956 ± 12	2.57 ± 0.03	-0.26 ± 0.01	-0.36 ± 0.03	Y
NGC 2204	2M06160212−1838467	4929 ± 11	2.38 ± 0.03	-0.31 ± 0.01	-0.14 ± 0.03	Y
NGC 2204	2M06161325−1844156	5007 ± 12	2.54 ± 0.03	-0.27 ± 0.01	-0.40 ± 0.03	Y
NGC 2243	2M06292939−3115459	5043 ± 14	2.51 ± 0.03	-0.44 ± 0.01	-0.32 ± 0.04	Y
NGC 2243	2M06293009−3116587	4693 ± 8	1.97 ± 0.03	-0.53 ± 0.01	-0.35 ± 0.03	N
NGC 2243	2M06293565−3117110	5088 ± 17	2.62 ± 0.04	-0.42 ± 0.01	-0.53 ± 0.05	Y
NGC 2243	2M06294150−3114360	4772 ± 11	2.30 ± 0.03	-0.46 ± 0.01	-0.25 ± 0.03	N
NGC 2243	2M06294583−3115382	5030 ± 14	2.48 ± 0.03	-0.46 ± 0.01	-0.39 ± 0.04	Y
NGC 2243	2M06295100−3114428	4930 ± 17	2.59 ± 0.04	-0.50 ± 0.01	-0.28 ± 0.05	Y
NGC 2304	2M06550345+1759521	4814 ± 8	2.43 ± 0.02	-0.16 ± 0.01	-0.39 ± 0.02	Y
NGC 2304	2M06551430+1759075	5199 ± 17	3.09 ± 0.03	-0.13 ± 0.01	-0.41 ± 0.04	N
NGC 2324	2M07035166+0106381	4920 ± 9	2.41 ± 0.02	-0.23 ± 0.01	-0.48 ± 0.02	N
NGC 2324	2M07040031+0058168	4533 ± 7	1.80 ± 0.02	-0.19 ± 0.01	-0.64 ± 0.02	N
NGC 2324	2M07040114+0106040	5226 ± 11	2.90 ± 0.02	-0.22 ± 0.01	-0.55 ± 0.03	N
NGC 2324	2M07041353+0102051	5216 ± 11	3.01 ± 0.02	-0.22 ± 0.01	-0.45 ± 0.03	N
NGC 2420	2M07380545+2136507	4866 ± 9	2.70 ± 0.02	-0.21 ± 0.01	-0.30 ± 0.02	Y
NGC 2420	2M07380627+2136542	4768 ± 8	2.45 ± 0.02	-0.24 ± 0.01	-0.30 ± 0.02	N
NGC 2420	2M07381507+2134589	4193 ± 5	1.48 ± 0.02	-0.27 ± 0.01	-0.33 ± 0.02	N
NGC 2420	2M07381549+2138015	4923 ± 9	2.59 ± 0.02	-0.22 ± 0.01	-0.32 ± 0.02	Y
NGC 2420	2M07381822+2132062	4936 ± 9	2.57 ± 0.02	-0.18 ± 0.01	-0.38 ± 0.02	N
NGC 2420	2M07382114+2131418	5099 ± 12	2.87 ± 0.03	-0.19 ± 0.01	-0.50 ± 0.03	Y
NGC 2420	2M07382148+2135050	4911 ± 9	2.75 ± 0.02	-0.18 ± 0.01	-0.33 ± 0.02	Y
NGC 2420	2M07382166+2133514	4559 ± 7	1.97 ± 0.02	-0.25 ± 0.01	-0.38 ± 0.02	N
NGC 2420	2M07382195+2135508	4903 ± 9	2.59 ± 0.02	-0.17 ± 0.01	-0.34 ± 0.02	N
NGC 2420	2M07382208+2136432	4940 ± 9	2.52 ± 0.02	-0.21 ± 0.01	-0.35 ± 0.02	Y
NGC 2420	2M07382406+2132148	4934 ± 9	2.53 ± 0.02	-0.23 ± 0.01	-0.35 ± 0.02	N
NGC 2420	2M07382670+2128514	4923 ± 10	2.62 ± 0.03	-0.18 ± 0.01	-0.36 ± 0.03	N
NGC 2420	2M07382696+2138244	4867 ± 9	2.47 ± 0.02	-0.19 ± 0.01	-0.34 ± 0.02	Y
NGC 2420	2M07382724+2133166	4970 ± 9	2.95 ± 0.02	-0.18 ± 0.01	-0.28 ± 0.02	N
NGC 2420	2M07382984+2134509	4821 ± 8	2.70 ± 0.02	-0.21 ± 0.01	-0.32 ± 0.02	N
NGC 2420	2M07383760+2134119	4942 ± 9	2.64 ± 0.02	-0.20 ± 0.01	-0.28 ± 0.02	Y
NGC 2447	2M07441988−2352345	5082 ± 10	2.75 ± 0.02	-0.11 ± 0.01	-0.55 ± 0.02	N

Continued on next page

Table C.1 – Continued

Cluster name	2MASS ID	T_{eff} (K)	log(g) (dex)	[Fe/H] (dex)	[C/N] (dex)	Clump	Red
NGC 2447	2M07442573−2349529	5077 ± 10	2.74 ± 0.02	-0.11 ± 0.01	-0.52 ± 0.02		N
NGC 2447	2M07443366−2351422	5092 ± 10	2.75 ± 0.02	-0.09 ± 0.01	-0.59 ± 0.02		N
NGC 2682	2M08501230+1151246	3987 ± 5	1.43 ± 0.02	-0.05 ± 0.01	-0.27 ± 0.02		N
NGC 2682	2M08504964+1135089	4772 ± 7	2.73 ± 0.02	0.00 ± 0.01	-0.38 ± 0.02		N
NGC 2682	2M08510839+1147121	4957 ± 9	3.28 ± 0.02	0.02 ± 0.01	-0.25 ± 0.02		N
NGC 2682	2M08511269+1152423	4773 ± 8	2.50 ± 0.02	-0.01 ± 0.01	-0.33 ± 0.02		Y
NGC 2682	2M08511704+1150464	4750 ± 7	2.68 ± 0.02	-0.05 ± 0.01	-0.38 ± 0.02		N
NGC 2682	2M08511710+1148160	4449 ± 6	2.14 ± 0.02	-0.00 ± 0.01	-0.34 ± 0.02		N
NGC 2682	2M08511897+1158110	4959 ± 9	3.21 ± 0.02	0.01 ± 0.01	-0.35 ± 0.02		N
NGC 2682	2M08512156+1146061	4778 ± 7	2.79 ± 0.02	0.03 ± 0.01	-0.42 ± 0.02		Y
NGC 2682	2M08512280+1148016	4760 ± 7	2.46 ± 0.02	0.02 ± 0.01	-0.41 ± 0.02		Y
NGC 2682	2M08512618+1153520	4784 ± 8	2.47 ± 0.02	-0.01 ± 0.01	-0.39 ± 0.02		Y
NGC 2682	2M08512898+1150330	4738 ± 7	2.43 ± 0.02	0.00 ± 0.01	-0.37 ± 0.02		Y
NGC 2682	2M08513577+1153347	4952 ± 9	3.19 ± 0.02	-0.01 ± 0.01	-0.30 ± 0.02		N
NGC 2682	2M08513938+1151456	4913 ± 8	3.12 ± 0.02	0.01 ± 0.01	-0.31 ± 0.02		N
NGC 2682	2M08514234+1150076	4811 ± 8	2.94 ± 0.02	0.02 ± 0.01	-0.34 ± 0.02		N
NGC 2682	2M08514235+1151230	4768 ± 7	2.71 ± 0.02	-0.01 ± 0.01	-0.39 ± 0.02		N
NGC 2682	2M08514388+1156425	4783 ± 8	2.47 ± 0.02	0.00 ± 0.01	-0.41 ± 0.02		N
NGC 2682	2M08514507+1147459	4817 ± 8	2.84 ± 0.02	-0.00 ± 0.01	-0.38 ± 0.02		N
NGC 2682	2M08515952+1155049	4784 ± 8	2.46 ± 0.02	-0.02 ± 0.01	-0.38 ± 0.02		Y
NGC 2682	2M08521856+1144263	4763 ± 10	2.49 ± 0.03	0.00 ± 0.01	-0.35 ± 0.02		N
NGC 4337	2M12235244−5806564	4887 ± 8	2.75 ± 0.02	0.24 ± 0.01	-0.55 ± 0.02		Y
NGC 4337	2M12235611−5806378	4894 ± 11	2.87 ± 0.02	0.24 ± 0.01	-0.49 ± 0.02		N
NGC 4337	2M12235665−5807252	4861 ± 9	2.81 ± 0.02	0.25 ± 0.01	-0.49 ± 0.02		N
NGC 4337	2M12240101−5807554	4339 ± 5	1.91 ± 0.02	0.21 ± 0.01	-0.48 ± 0.01		N
NGC 4337	2M12240586−5807152	4907 ± 10	2.75 ± 0.02	0.21 ± 0.01	-0.54 ± 0.02		N
NGC 4337	2M12241575−5808502	4882 ± 8	2.79 ± 0.02	0.21 ± 0.01	-0.49 ± 0.02		N
NGC 6791	2M19202447+3746139	4417 ± 8	2.46 ± 0.02	0.31 ± 0.01	-0.19 ± 0.02		N
NGC 6791	2M19203005+3750191	4487 ± 10	2.44 ± 0.03	0.32 ± 0.01	-0.17 ± 0.02		N
NGC 6791	2M19203266+3746221	4297 ± 8	2.28 ± 0.02	0.34 ± 0.01	-0.16 ± 0.02		N
NGC 6791	2M19203519+3748579	3925 ± 6	1.53 ± 0.02	0.27 ± 0.01	-0.14 ± 0.02		N
NGC 6791	2M19203585+3746520	4364 ± 8	2.35 ± 0.02	0.34 ± 0.01	-0.17 ± 0.02		N
NGC 6791	2M19203922+3744372	4541 ± 8	2.23 ± 0.02	0.35 ± 0.01	0.04 ± 0.02		N
NGC 6791	2M19203934+3748048	4259 ± 8	2.21 ± 0.03	0.27 ± 0.01	-0.15 ± 0.02		N
NGC 6791	2M19204197+3747541	4498 ± 8	2.44 ± 0.02	0.30 ± 0.01	-0.17 ± 0.02		N
NGC 6791	2M19204228+3745548	4490 ± 8	2.40 ± 0.02	0.34 ± 0.01	-0.14 ± 0.02		N
NGC 6791	2M19204356+3747019	4299 ± 8	2.14 ± 0.03	0.29 ± 0.01	-0.19 ± 0.02		N
NGC 6791	2M19204367+3746416	4343 ± 6	2.35 ± 0.02	0.34 ± 0.01	-0.18 ± 0.01		N
NGC 6791	2M19204485+3746215	4021 ± 7	1.72 ± 0.03	0.29 ± 0.01	-0.15 ± 0.02		N
NGC 6791	2M19204532+3747179	4519 ± 8	2.38 ± 0.02	0.30 ± 0.01	-0.14 ± 0.02		Y
NGC 6791	2M19204557+3739509	4488 ± 9	2.42 ± 0.02	0.41 ± 0.01	-0.22 ± 0.02		Y
NGC 6791	2M19204570+3754354	4479 ± 8	2.38 ± 0.02	0.34 ± 0.01	-0.12 ± 0.02		Y
NGC 6791	2M19204635+3750228	3867 ± 4	1.40 ± 0.02	0.28 ± 0.01	-0.17 ± 0.01		N
NGC 6791	2M19204965+3744077	4491 ± 9	2.33 ± 0.03	0.32 ± 0.01	-0.16 ± 0.02		N
NGC 6791	2M19204971+3743426	3515 ± 3	0.82 ± 0.02	0.24 ± 0.01	-0.08 ± 0.01		N

Continued on next page

Table C.1 – Continued

Cluster name	2MASS ID	T_{eff} (K)	log(g) (dex)	[Fe/H] (dex)	[C/N] (dex)	Clump	Red
NGC 6791	2M19205243+3747152	4580 ± 8	2.78 ± 0.02	0.31 ± 0.01	-0.20 ± 0.02		N
NGC 6791	2M19205247+3750154	4459 ± 10	2.55 ± 0.03	0.24 ± 0.01	0.01 ± 0.02		N
NGC 6791	2M19205259+3744281	4020 ± 7	1.71 ± 0.03	0.29 ± 0.01	-0.14 ± 0.02		N
NGC 6791	2M19205338+3748282	4006 ± 4	1.61 ± 0.02	0.32 ± 0.01	-0.18 ± 0.01		N
NGC 6791	2M19205499+3745410	4501 ± 7	2.61 ± 0.02	0.31 ± 0.01	-0.19 ± 0.02		N
NGC 6791	2M19205510+3747162	3897 ± 4	1.44 ± 0.02	0.28 ± 0.01	-0.20 ± 0.01		N
NGC 6791	2M19205530+3743152	4242 ± 7	2.19 ± 0.02	0.30 ± 0.01	-0.18 ± 0.02		N
NGC 6791	2M19205770+3749012	4491 ± 8	2.64 ± 0.02	0.36 ± 0.01	-0.19 ± 0.02		N
NGC 6791	2M19205784+3747067	4533 ± 10	2.66 ± 0.03	0.32 ± 0.01	-0.16 ± 0.02		N
NGC 6791	2M19205874+3743130	4486 ± 9	2.36 ± 0.02	0.35 ± 0.01	-0.16 ± 0.02		Y
NGC 6791	2M19210052+3750188	4458 ± 10	2.64 ± 0.03	0.23 ± 0.01	-0.08 ± 0.02		N
NGC 6791	2M19210086+3746396	4493 ± 10	2.31 ± 0.03	0.33 ± 0.01	-0.15 ± 0.02		Y
NGC 6791	2M19210094+3741101	4477 ± 9	2.63 ± 0.02	0.36 ± 0.01	-0.14 ± 0.02		N
NGC 6791	2M19210145+3748051	4594 ± 8	2.85 ± 0.02	0.35 ± 0.01	-0.20 ± 0.02		N
NGC 6791	2M19210417+3746226	4589 ± 8	2.78 ± 0.02	0.33 ± 0.01	-0.19 ± 0.02		N
NGC 6791	2M19210426+3747187	4107 ± 5	1.78 ± 0.02	0.31 ± 0.01	-0.15 ± 0.01		N
NGC 6791	2M19210483+3741036	4487 ± 9	2.45 ± 0.03	0.31 ± 0.01	-0.12 ± 0.02		N
NGC 6791	2M19210604+3752049	4519 ± 10	2.69 ± 0.03	0.30 ± 0.01	-0.20 ± 0.02		N
NGC 6791	2M19210807+3749084	4537 ± 8	2.67 ± 0.02	0.32 ± 0.01	-0.20 ± 0.02		N
NGC 6791	2M19211007+3750008	4456 ± 8	2.54 ± 0.02	0.28 ± 0.01	-0.19 ± 0.02		N
NGC 6791	2M19211164+3750483	4519 ± 8	2.69 ± 0.02	0.34 ± 0.01	-0.17 ± 0.02		N
NGC 6791	2M19211606+3746462	3527 ± 3	0.76 ± 0.02	0.23 ± 0.01	-0.11 ± 0.01		N
NGC 6791	2M19211725+3743187	4422 ± 8	2.17 ± 0.02	0.39 ± 0.01	0.07 ± 0.02		Y
NGC 6811	2M19365580+4627376	5096 ± 10	3.01 ± 0.02	-0.06 ± 0.01	-0.51 ± 0.02		N
NGC 6811	2M19365712+4622425	5113 ± 10	2.97 ± 0.02	-0.08 ± 0.01	-0.50 ± 0.02		N
NGC 6811	2M19370267+4623130	5097 ± 10	3.01 ± 0.02	-0.06 ± 0.01	-0.58 ± 0.02		N
NGC 6811	2M19372208+4632505	5056 ± 10	2.90 ± 0.02	-0.04 ± 0.01	-0.49 ± 0.02		N
NGC 6811	2M19373462+4624098	4948 ± 9	2.67 ± 0.02	-0.04 ± 0.01	-0.53 ± 0.02		Y
NGC 6811	2M19375017+4607465	5112 ± 10	2.96 ± 0.02	-0.05 ± 0.01	-0.53 ± 0.02		N
NGC 6819	2M19403684+4015172	4901 ± 14	3.04 ± 0.03	0.10 ± 0.01	-0.32 ± 0.03		N
NGC 6819	2M19404803+4008085	4577 ± 6	2.26 ± 0.02	-0.01 ± 0.01	-0.38 ± 0.02		Y
NGC 6819	2M19404965+4014313	4726 ± 9	2.62 ± 0.02	0.04 ± 0.01	-0.33 ± 0.02		N
NGC 6819	2M19405020+4013109	4765 ± 8	2.59 ± 0.02	0.09 ± 0.01	-0.32 ± 0.02		N
NGC 6819	2M19405601+4013395	4885 ± 12	2.92 ± 0.03	0.04 ± 0.01	-0.34 ± 0.03		N
NGC 6819	2M19405797+4008174	4835 ± 8	2.56 ± 0.02	0.06 ± 0.01	-0.53 ± 0.02		Y
NGC 6819	2M19410524+4014042	4793 ± 10	2.58 ± 0.03	0.06 ± 0.01	-0.37 ± 0.02		Y
NGC 6819	2M19410622+4010532	4876 ± 12	2.93 ± 0.03	0.05 ± 0.01	-0.37 ± 0.03		N
NGC 6819	2M19410858+4013299	4780 ± 7	2.53 ± 0.02	0.06 ± 0.01	-0.36 ± 0.02		Y
NGC 6819	2M19410926+4014436	4800 ± 8	2.59 ± 0.02	0.06 ± 0.01	-0.30 ± 0.02		Y
NGC 6819	2M19410991+4015495	4783 ± 10	2.54 ± 0.03	0.00 ± 0.01	-0.34 ± 0.02		Y
NGC 6819	2M19410994+4009056	4973 ± 13	3.07 ± 0.03	-0.05 ± 0.01	-0.30 ± 0.03		N
NGC 6819	2M19411102+4011116	4953 ± 9	2.51 ± 0.02	0.04 ± 0.01	-0.64 ± 0.02		N
NGC 6819	2M19411115+4011422	4661 ± 7	2.25 ± 0.02	0.06 ± 0.01	-0.49 ± 0.02		Y
NGC 6819	2M19411224+4011338	4696 ± 7	2.48 ± 0.02	0.04 ± 0.01	-0.36 ± 0.02		N
NGC 6819	2M19411279+4012238	4792 ± 8	2.52 ± 0.02	0.05 ± 0.01	-0.43 ± 0.02		N

Continued on next page

Table C.1 – Continued

Cluster name	2MASS ID	T_{eff} (K)	log(g) (dex)	[Fe/H] (dex)	[C/N] (dex)	Clump	Red
NGC 6819	2M19411345+4011561	4807 ± 9	2.57 ± 0.02	0.02 ± 0.01	-0.28 ± 0.02		N
NGC 6819	2M19411355+4012205	4830 ± 8	2.55 ± 0.02	0.02 ± 0.01	-0.39 ± 0.02		N
NGC 6819	2M19411367+4003382	4709 ± 8	2.46 ± 0.02	-0.01 ± 0.01	0.15 ± 0.02		N
NGC 6819	2M19411476+4011008	4889 ± 8	2.63 ± 0.02	0.08 ± 0.01	-0.63 ± 0.02		N
NGC 6819	2M19411564+4010105	4774 ± 10	2.58 ± 0.03	0.07 ± 0.01	-0.34 ± 0.02		N
NGC 6819	2M19411631+4005508	4794 ± 8	2.82 ± 0.02	0.00 ± 0.01	-0.32 ± 0.02		N
NGC 6819	2M19411705+4010517	4097 ± 5	1.55 ± 0.02	-0.03 ± 0.01	-0.28 ± 0.01		N
NGC 6819	2M19411776+4009158	4977 ± 9	2.77 ± 0.02	0.05 ± 0.01	-0.70 ± 0.02		N
NGC 6819	2M19411893+4011408	4696 ± 8	2.61 ± 0.02	0.02 ± 0.01	-0.34 ± 0.02		N
NGC 6819	2M19412136+4011002	4651 ± 9	2.50 ± 0.03	0.02 ± 0.01	-0.34 ± 0.02		N
NGC 6819	2M19412147+4013573	4782 ± 7	2.53 ± 0.02	0.07 ± 0.01	-0.38 ± 0.02		N
NGC 6819	2M19412176+4012111	4640 ± 7	2.47 ± 0.02	0.05 ± 0.01	-0.35 ± 0.02		N
NGC 6819	2M19412222+4016442	4676 ± 7	2.50 ± 0.02	0.01 ± 0.01	-0.39 ± 0.02		Y
NGC 6819	2M19412245+4012033	4960 ± 11	2.86 ± 0.03	0.06 ± 0.01	-0.35 ± 0.03		N
NGC 6819	2M19412386+4021444	4819 ± 8	2.61 ± 0.02	0.05 ± 0.01	-0.34 ± 0.02		Y
NGC 6819	2M19412658+4011418	4488 ± 6	2.09 ± 0.02	0.00 ± 0.01	-0.32 ± 0.02		N
NGC 6819	2M19412707+4012283	4595 ± 6	2.42 ± 0.02	0.01 ± 0.01	-0.38 ± 0.02		N
NGC 6819	2M19412915+4013040	4809 ± 8	2.55 ± 0.02	0.05 ± 0.01	-0.34 ± 0.02		Y
NGC 6819	2M19412942+4014199	4713 ± 9	2.62 ± 0.02	0.04 ± 0.01	-0.35 ± 0.02		N
NGC 6819	2M19412953+4012210	4771 ± 7	2.52 ± 0.02	0.06 ± 0.01	-0.35 ± 0.02		N
NGC 6819	2M19413027+4015218	4791 ± 8	2.50 ± 0.02	0.03 ± 0.01	-0.36 ± 0.02		Y
NGC 6819	2M19413330+4012349	4656 ± 7	2.35 ± 0.02	-0.02 ± 0.01	-0.42 ± 0.02		N
NGC 6819	2M19413439+4017482	4182 ± 5	1.67 ± 0.02	0.02 ± 0.01	-0.29 ± 0.01		N
NGC 6819	2M19413444+4008462	4791 ± 8	2.56 ± 0.02	0.04 ± 0.01	-0.37 ± 0.02		N
NGC 6819	2M19414427+4005527	4616 ± 7	2.39 ± 0.02	-0.01 ± 0.01	-0.39 ± 0.02		Y
NGC 6819	2M19415064+4016010	4884 ± 12	2.96 ± 0.03	0.08 ± 0.01	-0.38 ± 0.03		N
NGC 6866	2M20032282+4415502	5096 ± 10	2.95 ± 0.02	0.01 ± 0.01	-0.52 ± 0.02		N
NGC 6866	2M20035516+4408242	5116 ± 10	3.07 ± 0.02	0.00 ± 0.01	-0.61 ± 0.02		N
NGC 752	2M01551261+3750145	5015 ± 9	2.90 ± 0.02	-0.05 ± 0.01	-0.49 ± 0.02		N
NGC 752	2M01551528+3750312	4927 ± 9	2.83 ± 0.02	-0.06 ± 0.01	-0.43 ± 0.02		Y
NGC 752	2M01552765+3759551	5042 ± 9	2.86 ± 0.02	-0.04 ± 0.01	-0.44 ± 0.02		N
NGC 752	2M01562163+3736084	4838 ± 8	2.64 ± 0.02	-0.07 ± 0.01	-0.45 ± 0.02		Y
NGC 752	2M01582981+3751374	5041 ± 10	2.87 ± 0.02	-0.07 ± 0.01	-0.43 ± 0.02		N
NGC 7789	2M23543902+5653346	4932 ± 9	2.66 ± 0.02	-0.03 ± 0.01	-0.42 ± 0.02		Y
NGC 7789	2M23554966+5639180	4512 ± 6	2.07 ± 0.02	-0.02 ± 0.01	-0.44 ± 0.02		N
NGC 7789	2M23555312+5641203	4405 ± 6	1.93 ± 0.02	-0.05 ± 0.01	-0.40 ± 0.02		N
NGC 7789	2M23555428+5646375	5019 ± 9	3.02 ± 0.02	-0.08 ± 0.01	-0.36 ± 0.02		N
NGC 7789	2M23555992+5640286	5009 ± 9	2.84 ± 0.02	-0.04 ± 0.01	-0.42 ± 0.02		N
NGC 7789	2M23560772+5635418	4989 ± 9	2.82 ± 0.02	0.06 ± 0.01	-0.55 ± 0.02		N
NGC 7789	2M23560776+5636057	5011 ± 9	2.82 ± 0.02	0.02 ± 0.01	-0.46 ± 0.02		N
NGC 7789	2M23561401+5648414	4895 ± 8	2.65 ± 0.02	0.02 ± 0.01	-0.47 ± 0.02		Y
NGC 7789	2M23561924+5644479	5009 ± 9	2.80 ± 0.02	-0.03 ± 0.01	-0.42 ± 0.02		N
NGC 7789	2M23562937+5655192	4980 ± 9	2.95 ± 0.02	-0.01 ± 0.01	-0.28 ± 0.02		N
NGC 7789	2M23562953+5648399	4947 ± 9	2.75 ± 0.02	-0.06 ± 0.01	-0.41 ± 0.02		Y
NGC 7789	2M23563201+5632590	4456 ± 6	1.97 ± 0.02	-0.08 ± 0.01	-0.38 ± 0.02		N

Continued on next page

Table C.1 – Continued

Cluster name	2MASS ID	T_{eff} (K)	log(g) (dex)	[Fe/H] (dex)	[C/N] (dex)	Clump	Red
NGC 7789	2M23563632+5645024	5174 ± 14	3.27 ± 0.03	-0.08 ± 0.01	-0.02 ± 0.03		N
NGC 7789	2M23563930+5645242	4965 ± 9	2.75 ± 0.02	-0.02 ± 0.01	-0.45 ± 0.02		Y
NGC 7789	2M23563958+5654443	4915 ± 8	2.69 ± 0.02	0.02 ± 0.01	-0.46 ± 0.02		N
NGC 7789	2M23564304+5650477	4941 ± 9	2.74 ± 0.02	0.01 ± 0.01	-0.40 ± 0.02		Y
NGC 7789	2M23564466+5625293	4945 ± 9	2.65 ± 0.02	-0.05 ± 0.01	-0.44 ± 0.02		N
NGC 7789	2M23564910+5649228	5098 ± 10	2.84 ± 0.02	-0.02 ± 0.01	-0.69 ± 0.02		N
NGC 7789	2M23565053+5649208	4956 ± 9	2.74 ± 0.02	-0.05 ± 0.01	-0.38 ± 0.02		Y
NGC 7789	2M23565473+5648163	4903 ± 8	2.66 ± 0.02	-0.01 ± 0.01	-0.42 ± 0.02		Y
NGC 7789	2M23565527+5638268	5020 ± 9	2.77 ± 0.02	-0.11 ± 0.01	-0.33 ± 0.02		N
NGC 7789	2M23565751+5645272	4606 ± 7	2.30 ± 0.02	-0.03 ± 0.01	-0.41 ± 0.02		N
NGC 7789	2M23570356+5643209	4929 ± 8	2.72 ± 0.02	0.02 ± 0.01	-0.45 ± 0.02		N
NGC 7789	2M23570718+5643112	4792 ± 8	2.60 ± 0.02	-0.02 ± 0.01	-0.44 ± 0.02		N
NGC 7789	2M23570744+5641417	4176 ± 5	1.60 ± 0.02	-0.06 ± 0.01	-0.35 ± 0.01		N
NGC 7789	2M23570895+5648504	4984 ± 9	2.77 ± 0.02	0.02 ± 0.01	-0.47 ± 0.02		Y
NGC 7789	2M23571013+5647167	4915 ± 8	2.66 ± 0.02	-0.03 ± 0.01	-0.35 ± 0.02		Y
NGC 7789	2M23571231+5653500	4811 ± 8	2.52 ± 0.02	-0.05 ± 0.01	-0.19 ± 0.02		N
NGC 7789	2M23571400+5640586	4553 ± 6	2.24 ± 0.02	-0.03 ± 0.01	-0.37 ± 0.02		N
NGC 7789	2M23571416+5655329	4927 ± 9	2.74 ± 0.02	-0.02 ± 0.01	-0.44 ± 0.02		Y
NGC 7789	2M23571728+5645333	4987 ± 11	2.84 ± 0.03	-0.03 ± 0.01	-0.48 ± 0.03		Y
NGC 7789	2M23571847+5650271	4903 ± 8	2.65 ± 0.02	-0.05 ± 0.01	-0.35 ± 0.02		Y
NGC 7789	2M23571902+5656555	5015 ± 9	2.78 ± 0.02	-0.06 ± 0.01	-0.44 ± 0.02		N
NGC 7789	2M23571911+5635561	4599 ± 7	2.20 ± 0.02	-0.05 ± 0.01	-0.43 ± 0.02		N
NGC 7789	2M23571920+5640514	4897 ± 8	2.62 ± 0.02	-0.01 ± 0.01	-0.52 ± 0.02		Y
NGC 7789	2M23572492+5646363	5045 ± 9	2.70 ± 0.02	-0.03 ± 0.01	-0.54 ± 0.02		N
NGC 7789	2M23572537+5647567	4977 ± 9	2.77 ± 0.02	-0.02 ± 0.01	-0.40 ± 0.02		N
NGC 7789	2M23572872+5635228	5027 ± 9	2.86 ± 0.02	-0.01 ± 0.01	-0.52 ± 0.02		N
NGC 7789	2M23573079+5646443	4957 ± 9	2.76 ± 0.02	-0.00 ± 0.01	-0.43 ± 0.02		Y
NGC 7789	2M23573184+5641221	4424 ± 6	1.97 ± 0.02	-0.04 ± 0.01	-0.40 ± 0.02		N
NGC 7789	2M23573262+5644057	4981 ± 12	2.81 ± 0.03	-0.03 ± 0.01	-0.43 ± 0.03		N
NGC 7789	2M23573563+5640000	4952 ± 10	2.79 ± 0.02	-0.00 ± 0.01	-0.41 ± 0.02		Y
NGC 7789	2M23573909+5641396	4963 ± 9	2.69 ± 0.02	-0.02 ± 0.01	-0.46 ± 0.02		N
NGC 7789	2M23574179+5643243	4926 ± 9	2.64 ± 0.02	-0.06 ± 0.01	-0.37 ± 0.02		Y
NGC 7789	2M23574480+5645439	4953 ± 9	2.71 ± 0.02	-0.05 ± 0.01	-0.42 ± 0.02		N
NGC 7789	2M23574581+5650413	4948 ± 9	2.72 ± 0.02	-0.03 ± 0.01	-0.42 ± 0.02		N
NGC 7789	2M23574649+5644255	4971 ± 9	2.71 ± 0.02	-0.04 ± 0.01	-0.49 ± 0.02		Y
NGC 7789	2M23574944+5634509	4848 ± 8	2.74 ± 0.02	-0.02 ± 0.01	-0.43 ± 0.02		Y
NGC 7789	2M23575047+5639226	4969 ± 9	2.78 ± 0.02	0.01 ± 0.01	-0.45 ± 0.02		N
NGC 7789	2M23575149+5651040	4353 ± 6	1.88 ± 0.02	-0.04 ± 0.01	-0.39 ± 0.02		N
NGC 7789	2M23575212+5646575	4615 ± 7	2.25 ± 0.02	-0.02 ± 0.01	-0.40 ± 0.02		N
NGC 7789	2M23575438+5647439	5005 ± 9	2.82 ± 0.02	0.00 ± 0.01	-0.50 ± 0.02		Y
NGC 7789	2M23580015+5650125	4445 ± 6	1.99 ± 0.02	-0.08 ± 0.01	-0.38 ± 0.02		N
NGC 7789	2M23580133+5639219	4799 ± 8	2.47 ± 0.02	-0.05 ± 0.01	-0.40 ± 0.02		N
NGC 7789	2M23580197+5645216	4935 ± 9	2.65 ± 0.02	-0.08 ± 0.01	-0.44 ± 0.02		N
NGC 7789	2M23580275+5647208	4764 ± 8	2.59 ± 0.02	-0.06 ± 0.01	-0.41 ± 0.02		N
NGC 7789	2M23580474+5646234	4752 ± 7	2.47 ± 0.02	-0.04 ± 0.01	-0.40 ± 0.02		Y

Continued on next page

Table C.1 – Continued

Cluster name	2MASS ID	T_{eff} (K)	log(g) (dex)	[Fe/H] (dex)	[C/N] (dex)	Clump	Red
NGC 7789	2M23580601+5649598	4966 ± 9	2.77 ± 0.02	-0.02 ± 0.01	-0.38 ± 0.02		N
NGC 7789	2M23580702+5640481	4935 ± 9	2.66 ± 0.02	0.00 ± 0.01	-0.40 ± 0.02		Y
NGC 7789	2M23581471+5651466	4334 ± 5	1.84 ± 0.02	-0.06 ± 0.01	-0.40 ± 0.02		N
NGC 7789	2M23581557+5649124	4891 ± 8	2.55 ± 0.02	-0.06 ± 0.01	-0.49 ± 0.02		Y
NGC 7789	2M23584652+5649526	5023 ± 9	2.89 ± 0.02	-0.02 ± 0.01	-0.59 ± 0.02		N
NGC 7789	2M23585008+5646159	5230 ± 11	3.12 ± 0.02	-0.09 ± 0.01	-0.34 ± 0.03		N
NGC 7789	2M23593820+5650358	4898 ± 8	2.59 ± 0.02	-0.06 ± 0.01	-0.38 ± 0.02		Y
NGC 7789	2M23594217+5649358	4994 ± 9	2.76 ± 0.02	-0.02 ± 0.01	-0.50 ± 0.02		N
Ruprecht 147	19155129−1617591	4805 ± 13	2.61 ± 0.03	0.07 ± 0.01	-0.31 ± 0.03		N
Ruprecht 147	2M19164574−1635226	4800 ± 7	2.84 ± 0.02	0.12 ± 0.01	-0.43 ± 0.02		N
Ruprecht 147	19180978−1616222	4787 ± 13	2.61 ± 0.03	0.16 ± 0.01	-0.40 ± 0.03		N
Teutsch 12	2M06253685+1336564	5111 ± 16	2.59 ± 0.03	-0.20 ± 0.01	-0.67 ± 0.04		N
Teutsch 12	2M06254335+1333557	5167 ± 15	2.74 ± 0.03	-0.22 ± 0.01	-0.50 ± 0.04		N
Teutsch 12	2M06254413+1338021	5229 ± 19	2.89 ± 0.03	-0.20 ± 0.01	-0.58 ± 0.04		N
Teutsch 12	2M06254974+1334302	5218 ± 18	2.88 ± 0.03	-0.19 ± 0.01	-0.55 ± 0.04		N
Teutsch 51	2M05534689+2648234	5184 ± 19	2.68 ± 0.04	-0.32 ± 0.01	-0.53 ± 0.05		N
Teutsch 51	2M05535631+2648351	5211 ± 24	2.76 ± 0.04	-0.36 ± 0.01	-0.52 ± 0.05		N
Teutsch 51	2M05535767+2649296	5078 ± 14	2.53 ± 0.03	-0.33 ± 0.01	-0.49 ± 0.04		N
Tombaugh 2	2M07025973−2049495	4428 ± 7	1.74 ± 0.03	-0.37 ± 0.01	-0.43 ± 0.02		N
Tombaugh 2	2M07030383−2049244	5185 ± 17	2.12 ± 0.03	-0.37 ± 0.01	-0.74 ± 0.04		N
Tombaugh 2	2M07030686−2048282	4644 ± 11	2.00 ± 0.03	-0.36 ± 0.01	-0.49 ± 0.03		N
Tombaugh 2	2M07031249−2049146	5170 ± 17	2.44 ± 0.03	-0.37 ± 0.01	-0.72 ± 0.05		N
Trumpler 20	2M12385807−6030286	4565 ± 6	2.16 ± 0.02	0.07 ± 0.01	-0.46 ± 0.02		N
Trumpler 20	2M12390411−6034001	4544 ± 6	2.11 ± 0.02	0.11 ± 0.01	-0.51 ± 0.02		N
Trumpler 20	2M12390477−6041475	4993 ± 13	2.82 ± 0.03	0.11 ± 0.01	-0.44 ± 0.03		Y
Trumpler 20	2M12391003−6038402	4573 ± 6	2.15 ± 0.02	0.10 ± 0.01	-0.52 ± 0.02		Y
Trumpler 20	2M12391201−6036321	4965 ± 12	2.77 ± 0.03	0.14 ± 0.01	-0.56 ± 0.03		N
Trumpler 20	2M12391577−6034406	4854 ± 11	2.79 ± 0.03	0.10 ± 0.01	-0.44 ± 0.02		N
Trumpler 20	2M12392584−6038279	4977 ± 13	2.80 ± 0.03	0.13 ± 0.01	-0.59 ± 0.03		N
Trumpler 20	2M12392637−6040217	4911 ± 11	2.71 ± 0.03	0.10 ± 0.01	-0.55 ± 0.02		N
Trumpler 20	2M12392699−6036052	4878 ± 10	2.81 ± 0.02	0.11 ± 0.01	-0.41 ± 0.02		N
Trumpler 20	2M12393781−6039051	4949 ± 11	2.72 ± 0.02	0.14 ± 0.01	-0.51 ± 0.02		N
Trumpler 20	2M12394121−6040040	4967 ± 13	2.72 ± 0.03	0.10 ± 0.01	-0.61 ± 0.03		N
Trumpler 20	2M12394387−6033165	4937 ± 11	2.78 ± 0.02	0.07 ± 0.01	-0.43 ± 0.02		N
Trumpler 20	2M12394419−6034410	4982 ± 14	2.76 ± 0.03	0.14 ± 0.01	-0.75 ± 0.03		N
Trumpler 20	2M12394715−6040583	4637 ± 7	2.23 ± 0.02	0.10 ± 0.01	-0.51 ± 0.02		Y
Trumpler 20	2M12394741−6038411	4962 ± 12	2.81 ± 0.03	0.13 ± 0.01	-0.44 ± 0.03		N
Trumpler 20	2M12395555−6037267	4905 ± 10	2.63 ± 0.02	0.11 ± 0.01	-0.60 ± 0.02		N
Trumpler 20	2M12395974−6035072	4902 ± 10	2.72 ± 0.02	0.10 ± 0.01	-0.43 ± 0.02		N
Trumpler 20	2M12400110−6031395	4882 ± 11	2.69 ± 0.03	0.10 ± 0.01	-0.48 ± 0.02		N
Trumpler 20	2M12400260−6039545	4575 ± 6	2.16 ± 0.02	0.11 ± 0.01	-0.53 ± 0.02		Y
Trumpler 20	2M12400278−6041192	4954 ± 12	2.74 ± 0.03	0.13 ± 0.01	-0.63 ± 0.03		N
Trumpler 20	2M12400451−6036566	4439 ± 6	2.07 ± 0.02	0.06 ± 0.01	-0.38 ± 0.01		N
Trumpler 20	2M12400755−6035445	4506 ± 6	2.13 ± 0.02	0.11 ± 0.01	-0.45 ± 0.01		N
Trumpler 20	2M12402228−6037419	4957 ± 11	2.78 ± 0.03	0.11 ± 0.01	-0.44 ± 0.02		N

Continued on next page

Table C.1 – Continued

Cluster name	2MASS ID	T_{eff} (K)	log(g) (dex)	[Fe/H] (dex)	[C/N] (dex)	Clump	Red
Trumpler 20	2M12402480−6043101	4624 ± 7	2.19 ± 0.02	0.07 ± 0.01	-0.53 ± 0.02		N
Trumpler 20	2M12402949−6038518	4591 ± 6	2.27 ± 0.02	0.09 ± 0.01	-0.47 ± 0.02		N
Trumpler 5	2M06353172+0924287	4809 ± 10	2.44 ± 0.03	-0.43 ± 0.01	-0.29 ± 0.03		Y
Trumpler 5	2M06363124+0928109	4741 ± 8	2.25 ± 0.03	-0.47 ± 0.01	-0.26 ± 0.03		N
Trumpler 5	2M06363859+0938525	4854 ± 12	2.49 ± 0.03	-0.44 ± 0.01	-0.28 ± 0.03		Y
Trumpler 5	2M06364193+0928117	5005 ± 13	2.49 ± 0.03	-0.46 ± 0.01	-0.17 ± 0.04		Y
Trumpler 5	2M06364229+0925257	4412 ± 6	1.70 ± 0.03	-0.46 ± 0.01	-0.36 ± 0.02		N
Trumpler 5	2M06364528+0923371	4835 ± 12	2.39 ± 0.03	-0.45 ± 0.01	-0.30 ± 0.03		N
Trumpler 5	2M06364741+0919364	4894 ± 15	2.61 ± 0.04	-0.44 ± 0.01	-0.25 ± 0.04		N
Trumpler 5	2M06364804+0932335	4820 ± 9	2.37 ± 0.03	-0.45 ± 0.01	-0.26 ± 0.03		Y

Bibliography

Abdurro'uf, Accetta, K., Aerts, C., Silva Aguirre, V., Ahumada, R., Ajgaonkar, N., Filiz Ak, N., Alam, S., Allende Prieto, C., Almeida, A., Anders, F., Anderson, S. F., Andrews, B. H., Anguiano, B., Aquino-Ortíz, E., Aragón-Salamanca, A., Argudo-Fernández, M., Ata, M., Aubert, M., Avila-Reese, V., Badenes, C., Barbá, R. H., Barger, K., Barrera-Ballesteros, J. K., Beaton, R. L., Beers, T. C., Belfiore, F., Bender, C. F., Bernardi, M., Bershady, M. A., Beutler, F., Bidin, C. M., Bird, J. C., Bizyaev, D., Blanc, G. A., Blanton, M. R., Boardman, N. F., Bolton, A. S., Boquien, M., Borissova, J., Bovy, J., Brandt, W. N., Brown, J., Brownstein, J. R., Brusa, M., Buchner, J., Bundy, K., Burchett, J. N., Bureau, M., Burgasser, A., Cabang, T. K., Campbell, S., Cappellari, M., Carlberg, J. K., Wanderley, F. C., Carrera, R., Cash, J., Chen, Y.-P., Chen, W.-H., Cherinka, B., Chiappini, C., Choi, P. D., Chojnowski, S. D., Chung, H., Clerc, N., Cohen, R. E., Comerford, J. M., Comparat, J., da Costa, L., Covey, K., Crane, J. D., Cruz-Gonzalez, I., Culhane, C., Cunha, K., Dai, Y. S., Damke, G., Darling, J., Davidson, James W., J., Davies, R., Dawson, K., De Lee, N., Diamond-Stanic, A. M., Cano-Díaz, M., Sánchez, H. D., Donor, J., Duckworth, C., Dwelly, T., Eisenstein, D. J., Elsworth, Y. P., Emsellem, E., Eracleous, M., Escoffier, S., Fan, X., Farr, E., Feng, S., Fernández-Trincado, J. G., Feuillet, D., Filipp, A., Fillingham, S. P., Frinchaboy, P. M., Fromenteau, S., Galbany, L., García, R. A., García-Hernández, D. A., Ge, J., Geisler, D., Gelfand, J., Géron, T., Gibson, B. J., Goddy, J., Godoy-Rivera, D., Grabowski, K., Green, P. J., Greener, M., Grier, C. J., Griffith, E., Guo, H., Guy, J., Hadjara, M., Harding, P., Hasselquist, S., Hayes, C. R., Hearty, F., Hernández, J., Hill, L., Hogg, D. W., Holtzman, J. A., Horta, D., Hsieh, B.-C., Hsu, C.-H., Hsu, Y.-H., Huber, D., Huertas-Company, M., Hutchinson, B., Hwang, H. S., Ibarra-Medel, H. J., Chitham, J. I., Ilha, G. S., Imig, J., Jaekle, W., Jayasinghe, T., Ji, X., Johnson, J. A., Jones, A., Jönsson, H., Katkov, I., Khalatyan, Arman, D., Kinemuchi, K., Kisku, S., Knapen, J. H., Kneib, J.-P., Kollmeier, J. A., Kong, M., Kounkel, M., Kreckel, K., Krishnarao, D., Lacerna, I., Lane, R. R., Langgin, R., Lavender, R., Law, D. R., Lazarz, D., Leung, H. W., Leung, H.-H., Lewis, H. M., Li, C., Li, R., Lian, J., Liang, F.-H., Lin, L., Lin, Y.-T., Lin, S., Lintott, C., Long, D., Longa-Peña, P., López-Cobá, C., Lu, S., Lundgren, B. F., Luo, Y., Mackereth, J. T., de la Macorra, A., Mahadevan, S., Majewski, S. R., Manchado, A., Mandeville, T., Maraston, C., Margalef-Bentabol, B., Masseron, T., Masters, K. L., Mathur, S., McDermid, R. M., Mckay, M., Merloni, A., Merrifield, M., Meszaros, S., Miglio, A., Di Mille, F., Minniti, D., Minsley, R., Monachesi, A., Moon, J., Mosser, B., Mulchaey, J., Muna, D., Muñoz, R. R., Myers, A. D., Myers, N., Nadathur, S., Nair, P., Nandra, K.,

Neumann, J., Newman, J. A., Nidever, D. L., Nikakhtar, F., Nitschelm, C., O'Connell, J. E., Garma-Oehmichen, L., Luan Souza de Oliveira, G., Olney, R., Oravetz, D., Ortigoza-Urdaneta, M., Osorio, Y., Otter, J., Pace, Z. J., Padilla, N., Pan, K., Pan, H.-A., Parikh, T., Parker, J., Peirani, S., Peña Ramírez, K., Penny, S., Percival, W. J., Perez-Fournon, I., Pinsonneault, M., Poidevin, F., Poovelil, V. J., Price-Whelan, A. M., Bárbara de Andrade Queiroz, A., Raddick, M. J., Ray, A., Rembold, S. B., Riddle, N., Riffel, R. A., Riffel, R., Rix, H.-W., Robin, A. C., Rodríguez-Puebla, A., Roman-Lopes, A., Román-Zúñiga, C., Rose, B., Ross, A. J., Rossi, G., Rubin, K. H. R., Salvato, M., Sánchez, S. F., Sánchez-Gallego, J. R., Sanderson, R., Santana Rojas, F. A., Sarceno, E., Sarmiento, R., Sayres, C., Sazonova, E., Schaefer, A. L., Schiavon, R., Schlegel, D. J., Schneider, D. P., Schultheis, M., Schwope, A., Serenelli, A., Serna, J., Shao, Z., Shapiro, G., Sharma, A., Shen, Y., Shetrone, M., Shu, Y., Simon, J. D., Skrutskie, M. F., Smethurst, R., Smith, V., Sobeck, J., Spoo, T., Sprague, D., Stark, D. V., Stassun, K. G., Steinmetz, M., Stello, D., Stone-Martinez, A., Storchi-Bergmann, T., Stringfellow, G. S., Stutz, A., Su, Y.-C., Taghizadeh-Popp, M., Talbot, M. S., Tayar, J., Telles, E., Teske, J., Thakar, A., Theissen, C., Tkachenko, A., Thomas, D., Tojeiro, R., Hernandez Toledo, H., Troup, N. W., Trump, J. R., Trussler, J., Turner, J., Tuttle, S., Unda-Sanzana, E., Vázquez-Mata, J. A., Valentini, M., Valenzuela, O., Vargas-González, J., Vargas-Magaña, M., Alfaro, P. V., Villanova, S., Vincenzo, F., Wake, D., Warfield, J. T., Washington, J. D., Weaver, B. A., Weijmans, A.-M., Weinberg, D. H., Weiss, A., Westfall, K. B., Wild, V., Wilde, M. C., Wilson, J. C., Wilson, R. F., Wilson, M., Wolf, J., Wood-Vasey, W. M., Yan, R., Zamora, O., Zasowski, G., Zhang, K., Zhao, C., Zheng, Z., Zheng, Z., & Zhu, K. 2022, Astrophysical Journal Supplement, 259, 35

Beaton, R. L., Oelkers, R. J., Hayes, C. R., Covey, K. R., Chojnowski, S. D., De Lee, N., Sobeck, J. S., Majewski, S. R., Cohen, R., Fernandez-Trincado, J., Longa-Pena, P., O'Connell, J. E., Santana, F. A., Stringfellow, G. S., Zasowski, G., Aerts, C., Anguiano, B., Bender, C., Canas, C. I., Cunha, K., Fleming, J. D. S. W., Frinchaboy, P. M., Feuillet, D., Harding, P., Hasselquist, S., Holtzman, J., Johnson, J. A., Kollmeier, J. A., Kounkel, M., Mahadevan, S., Price-Whelan, A. M., Rojas-Arriagada, A., Roman-Zuniga, C., Schlafly, E. F., Schultheis, M., Shetrone, M., Simon, J. D., Stassun, K. G., Stutz, A. M., Tayar, J., Teske, J., Tkachenko, A., Troup, N., Albareti, F. D., Bizyaev, D., Bovy, J., Burgasser, A. J., Comparat, J., Downes, J. J., Geisler, D., Inno, L., Manchado, A., Ness, M. K., Pinsonneault, M. H., Prada, F., Roman-Lopes, A., Simonian, G. V. A., Smith, V. V., Yan, R., & Zamora, O. 2021, arXiv e-prints, arXiv:2108.11907

Bertelli Motta, C., Pasquali, A., Richer, J., Michaud, G., Salaris, M., Bragaglia, A., Magrini, L., Randich, S., Grebel, E. K., Adibekyan, V., Blanco-Cuaresma, S., Drazdauskas, A., Fu, X., Martell, S., Tautvaišienė, G., Gilmore, G., Alfaro, E. J., Bensby, T., Flaccomio, E., Koposov, S. E., Korn, A. J., Lanzafame, A. C., Smiljanic, R., Bayo, A., Carraro, G., Casey, A. R., Costado, M. T., Damiani, F., Franciosini, E., Heiter, U., Hourihane, A., Jofré, P., Lardo, C., Lewis, J., Monaco, L., Morbidelli, L., Sacco,

G. G., Sousa, S. G., Worley, C. C., & Zaggia, S. 2018, Monthly Notices of the Royal Astronomical Society, 478, 425

Blanton, M. R., Bershady, M. A., Abolfathi, B., Albareti, F. D., Allende Prieto, C., Almeida, A., Alonso-García, J., Anders, F., Anderson, S. F., Andrews, B., & et al. 2017, The Astronomical Journal, 154, 28

Boesgaard, A. M., Deliyannis, C. P., Stephens, A., & King, J. R. 1998, The Astrophysical Journal, 493, 206

Bouma, L. G., Curtis, J. L., Hartman, J. D., Winn, J. N., & Bakos, G. Á. 2021, The Astronomical Journal, 162, 197

Bovy, J., Nidever, D. L., Rix, H.-W., Girardi, L., Zasowski, G., Chojnowski, S. D., Holtzman, J., Epstein, C., Frinchaboy, P. M., Hayden, M. R., Rodrigues, T. S., Majewski, S. R., Johnson, J. A., Pinsonneault, M. H., Stello, D., Allende Prieto, C., Andrews, B., Basu, S., Beers, T. C., Bizyaev, D., Burton, A., Chaplin, W. J., Cunha, K., Elsworth, Y., García, R. A., García-Herńandez, D. A., García Pérez, A. E., Hearty, F. R., Hekker, S., Kallinger, T., Kinemuchi, K., Koesterke, L., Mészáros, S., Mosser, B., O'Connell, R. W., Oravetz, D., Pan, K., Robin, A. C., Schiavon, R. P., Schneider, D. P., Schultheis, M., Serenelli, A., Shetrone, M., Silva Aguirre, V., Simmons, A., Skrutskie, M., Smith, V. V., Stassun, K., Weinberg, D. H., Wilson, J. C., & Zamora, O. 2014, The Astrophysical Journal, 790, 127

Bowen, I. S. & Vaughan, A. H., J. 1973, Applied Optics, 12, 1430

Bufanda, E., Tayar, J., Huber, D., Hasselquist, S., & Lane, R. R. 2023, The Astrophysical Journal, 959, 123

Cantat-Gaudin, T., Anders, F., Castro-Ginard, A., Jordi, C., Romero-Gomez, M., Soubiran, C., Casamiquela, L., Tarricq, Y., Moitinho, A., Vallenari, A., Bragaglia, A., Krone-Martins, A., & Kounkel, M. 2020, arXiv e-prints, arXiv:2004.07274

Cantat-Gaudin, T., Jordi, C., Vallenari, A., Bragaglia, A., Balaguer-Núñez, L., Soubiran, C., Bossini, D., Moitinho, A., Castro-Ginard, A., Krone-Martins, A., Casamiquela, L., Sordo, R., & Carrera, R. 2018, Astronomy and Astrophysics, 618, A93

Casali, G., Magrini, L., Tognelli, E., Jackson, R., Jeffries, R. D., Lagarde, N., Tautvaišienė, G., Masseron, T., Degl'Innocenti, S., Prada Moroni, P. G., Kordopatis, G., Pancino, E., Randich, S., Feltzing, S., Sahlholdt, C., Spina, L., Friel, E., Roccatagliata, V., Sanna, N., Bragaglia, A., Drazdauskas, A., Mikolaitis, Š., Minkevičiūtė, R., Stonkutė, E., Chorniy, Y., Bagdonas, V., Jimenez-Esteban, F., Martell, S., Van der Swaelmen, M., Gilmore, G., Vallenari, A., Bensby, T., Koposov, S. E., Korn, A., Worley, C., Smiljanic, R., Bergemann, M., Carraro, G., Damiani, F., Prisinzano, L., Bonito, R., Franciosini, E., Gonneau, A., Hourihane, A., Jofre, P., Lewis, J., Morbidelli, L., Sacco, G., Sousa, S. G., Zaggia, S., Lanzafame, A. C., Heiter, U., Frasca, A., & Bayo, A. 2019, Astronomy and Astrophysics, 629, A62

Casali, G., Spina, L., Magrini, L., Karakas, A. I., Kobayashi, C., Casey, A. R., Feltzing, S., Van der Swaelmen, M., Tsantaki, M., Jofré, P., Bragaglia, A., Feuillet, D., Bensby, T., Biazzo, K., Gonneau, A., Tautvaišienė, G., Baratella, M., Roccatagliata, V., Pancino, E., Sousa, S., Adibekyan, V., Martell, S., Bayo, A., Jackson, R. J., Jeffries, R. D., Gilmore, G., Randich, S., Alfaro, E., Koposov, S. E., Korn, A. J., Recio-Blanco, A., Smiljanic, R., Franciosini, E., Hourihane, A., Monaco, L., Morbidelli, L., Sacco, G., Worley, C., & Zaggia, S. 2020, Astronomy and Astrophysics, 639, A127

Chapman, S. 1917a, Monthly Notices of the Royal Astronomical Society, 77, 540

—. 1917b, Monthly Notices of the Royal Astronomical Society, 77, 539

Charbonnel, C. & Lagarde, N. 2010, Astronomy and Astrophysics, 522, A10

Choi, J., Dotter, A., Conroy, C., Cantiello, M., Paxton, B., & Johnson, B. D. 2016, The Astrophysical Journal, 823, 102

Cunha, K., Smith, V. V., Johnson, J. A., Bergemann, M., Mészáros, S., Shetrone, M. D., Souto, D., Allende Prieto, C., Schiavon, R. P., Frinchaboy, P., Zasowski, G., Bizyaev, D., Holtzman, J., García Pérez, A. E., Majewski, S. R., Nidever, D., Beers, T., Carrera, R., Geisler, D., Gunn, J., Hearty, F., Ivans, I., Martell, S., Pinsonneault, M., Schneider, D. P., Sobeck, J., Stello, D., Stassun, K. G., Skrutskie, M., & Wilson, J. C. 2015, The Astrophysical Journal Letters, 798, L41

Cutri, R. M., Skrutskie, M. F., van Dyk, S., Beichman, C. A., Carpenter, J. M., Chester, T., Cambresy, L., Evans, T., Fowler, J., Gizis, J., Howard, E., Huchra, J., Jarrett, T., Kopan, E. L., Kirkpatrick, J. D., Light, R. M., Marsh, K. A., McCallon, H., Schneider, S., Stiening, R., Sykes, M., Weinberg, M., Wheaton, W. A., Wheelock, S., & Zacarias, N. 2003, 2MASS All Sky Catalog of point sources.

Donor, J., Frinchaboy, P. M., Cunha, K., O'Connell, J. E., Allende Prieto, C., Almeida, A., Anders, F., Beaton, R., Bizyaev, D., Brownstein, J. R., Carrera, R., Chiappini, C., Cohen, R., García-Hernández, D. A., Geisler, D., Hasselquist, S., Jönsson, H., Lane, R. R., Majewski, S. R., Minniti, D., Bidin, C. M., Pan, K., Roman-Lopes, A., Sobeck, J. S., & Zasowski, G. 2020, The Astronomical Journal, 159, 199

Donor, J., Frinchaboy, P. M., Cunha, K., Thompson, B., O'Connell, J., Zasowski, G., Jackson, K. M., Meyer McGrath, B., Almeida, A., Bizyaev, D., Carrera, R., García-Hernández, D. A., Nitschelm, C., Pan, K., & Zamora, O. 2018, The Astronomical Journal, 156, 142

Dotter, A. 2016, Astrophysical Journal Supplement, 222, 8

Dotter, A., Conroy, C., Cargile, P., & Asplund, M. 2017, The Astrophysical Journal, 840, 99

Dreyer, J. L. E. 1888, Memoirs of the Royal Astronomical Society, 49, 1

Eisenstein, D. J., Weinberg, D. H., Agol, E., Aihara, H., Allende Prieto, C., Anderson, S. F., Arns, J. A., Aubourg, É., Bailey, S., Balbinot, E., Barkhouser, R., Beers, T. C., Berlind, A. A., Bickerton, S. J., Bizyaev, D., Blanton, M. R., Bochanski, J. J., Bolton, A. S., Bosman, C. T., Bovy, J., Brandt, W. N., Breslauer, B., Brewington, H. J., Brinkmann, J., Brown, P. J., Brownstein, J. R., Burger, D., Busca, N. G., Campbell, H., Cargile, P. A., Carithers, W. C., Carlberg, J. K., Carr, M. A., Chang, L., Chen, Y., Chiappini, C., Comparat, J., Connolly, N., Cortes, M., Croft, R. A. C., Cunha, K., da Costa, L. N., Davenport, J. R. A., Dawson, K., De Lee, N., Porto de Mello, G. F., de Simoni, F., Dean, J., Dhital, S., Ealet, A., Ebelke, G. L., Edmondson, E. M., Eiting, J. M., Escoffier, S., Esposito, M., Evans, M. L., Fan, X., Femenía Castellá, B., Dutra Ferreira, L., Fitzgerald, G., Fleming, S. W., Font-Ribera, A., Ford, E. B., Frinchaboy, P. M., García Pérez, A. E., Gaudi, B. S., Ge, J., Ghezzi, L., Gillespie, B. A., Gilmore, G., Girardi, L., Gott, J. R., Gould, A., Grebel, E. K., Gunn, J. E., Hamilton, J.-C., Harding, P., Harris, D. W., Hawley, S. L., Hearty, F. R., Hennawi, J. F., González Hernández, J. I., Ho, S., Hogg, D. W., Holtzman, J. A., Honscheid, K., Inada, N., Ivans, I. I., Jiang, L., Jiang, P., Johnson, J. A., Jordan, C., Jordan, W. P., Kauffmann, G., Kazin, E., Kirkby, D., Klaene, M. A., Knapp, G. R., Kneib, J.-P., Kochanek, C. S., Koesterke, L., Kollmeier, J. A., Kron, R. G., Lampeitl, H., Lang, D., Lawler, J. E., Le Goff, J.-M., Lee, B. L., Lee, Y. S., Leisenring, J. M., Lin, Y.-T., Liu, J., Long, D. C., Loomis, C. P., Lucatello, S., Lundgren, B., Lupton, R. H., Ma, B., Ma, Z., MacDonald, N., Mack, C., Mahadevan, S., Maia, M. A. G., Majewski, S. R., Makler, M., Malanushenko, E., Malanushenko, V., Mandelbaum, R., Maraston, C., Margala, D., Maseman, P., Masters, K. L., McBride, C. K., McDonald, P., McGreer, I. D., McMahon, R. G., Mena Requejo, O., Ménard, B., Miralda-Escudé, J., Morrison, H. L., Mullally, F., Muna, D., Murayama, H., Myers, A. D., Naugle, T., Neto, A. F., Nguyen, D. C., Nichol, R. C., Nidever, D. L., O'Connell, R. W., Ogando, R. L. C., Olmstead, M. D., Oravetz, D. J., Padmanabhan, N., Paegert, M., Palanque-Delabrouille, N., Pan, K., Pandey, P., Parejko, J. K., Pâris, I., Pellegrini, P., Pepper, J., Percival, W. J., Petitjean, P., Pfaffenberger, R., Pforr, J., Phleps, S., Pichon, C., Pieri, M. M., Prada, F., Price-Whelan, A. M., Raddick, M. J., Ramos, B. H. F., Reid, I. N., Reyle, C., Rich, J., Richards, G. T., Rieke, G. H., Rieke, M. J., Rix, H.-W., Robin, A. C., Rocha-Pinto, H. J., Rockosi, C. M., Roe, N. A., Rollinde, E., Ross, A. J., Ross, N. P., Rossetto, B., Sánchez, A. G., Santiago, B., Sayres, C., Schiavon, R., Schlegel, D. J., Schlesinger, K. J., Schmidt, S. J., Schneider, D. P., Sellgren, K., Shelden, A., Sheldon, E., Shetrone, M., Shu, Y., Silverman, J. D., Simmerer, J., Simmons, A. E., Sivarani, T., Skrutskie, M. F., Slosar, A., Smee, S., Smith, V. V., Snedden, S. A., Stassun, K. G., Steele, O., Steinmetz, M., Stockett, M. H., Stollberg, T., Strauss, M. A., Szalay, A. S., Tanaka, M., Thakar, A. R., Thomas, D., Tinker, J. L., Tofflemire, B. M., Tojeiro, R., Tremonti, C. A., Vargas Magaña, M., Verde, L., Vogt, N. P., Wake, D. A., Wan, X., Wang, J., Weaver, B. A., White, M., White, S. D. M., Wilson, J. C., Wisniewski, J. P., Wood-Vasey, W. M., Yanny, B., Yasuda, N., Yèche, C., York, D. G., Young, E., Zasowski, G., Zehavi, I., & Zhao, B. 2011, The Astronomical Journal, 142, 72

Fraser, A. E., Joyce, M., Anders, E. H., Tayar, J., & Cantiello, M. 2022, The Astrophys-

ical Journal, 941, 164

Frinchaboy, P. M., Thompson, B., Jackson, K. M., O'Connell, J., Meyer, B., Zasowski, G., Majewski, S. R., Chojnowksi, S. D., Johnson, J. A., Allende Prieto, C., Beers, T. C., Bizyaev, D., Brewington, H., Cunha, K., Ebelke, G., García Pérez, A. E., Hearty, F. R., Holtzman, J., Kinemuchi, K., Malanushenko, E., Malanushenko, V., Marchante, M., Mészáros, S., Muna, D., Nidever, D. L., Oravetz, D., Pan, K., Schiavon, R. P., Schneider, D. P., Shetrone, M., Simmons, A., Snedden, S., Smith, V. V., & Wilson, J. C. 2013, The Astrophysical Journal Letters, 777, L1

Gaia Collaboration, Brown, A. G. A., Vallenari, A., Prusti, T., de Bruijne, J. H. J., Babusiaux, C., Bailer-Jones, C. A. L., Biermann, M., Evans, D. W., Eyer, L., & et al. 2018, Astronomy and Astrophysics, 616, A1

Gao, X., Lind, K., Amarsi, A. M., Buder, S., Dotter, A., Nordlander, T., Asplund, M., Bland-Hawthorn, J., de Silva, G. M., D'Orazi, V., Freeman, K. C., Kos, J., Lewis, G. F., Lin, J., Martell, S. L., Schlesinger, K. J., Sharma, S., Simpson, J. D., Zucker, D. B., Zwitter, T., da Costa, G., Anguiano, B., Horner, J., Hyde, E. A., Kafle, P. R., Nataf, D. M., Reid, W., Stello, D., Ting, Y.-S., & Galah Collaboration. 2018, Monthly Notices of the Royal Astronomical Society, 481, 2666

García Pérez, A. E., Allende Prieto, C., Holtzman, J. A., Shetrone, M., Mészáros, S., Bizyaev, D., Carrera, R., Cunha, K., García-Hernández, D. A., Johnson, J. A., Majewski, S. R., Nidever, D. L., Schiavon, R. P., Shane, N., Smith, V. V., Sobeck, J., Troup, N., Zamora, O., Weinberg, D. H., Bovy, J., Eisenstein, D. J., Feuillet, D., Frinchaboy, P. M., Hayden, M. R., Hearty, F. R., Nguyen, D. C., O'Connell, R. W., Pinsonneault, M. H., Wilson, J. C., & Zasowski, G. 2016, The Astronomical Journal, 151, 144

Girardi, L. 2016, Annual Review of Astronomy and Astrophysics, 54, 95

Girardi, L., Bressan, A., Bertelli, G., & Chiosi, C. 2000, Astronomy and Astrophysics Supplement, 141, 371

González Hernández, J. I. & Bonifacio, P. 2009, Astronomy and Astrophysics, 497, 497

Gratton, R. G., Sneden, C., Carretta, E., & Bragaglia, A. 2000, Astronomy and Astrophysics, 354, 169

Gruyters, P., Korn, A. J., Richard, O., Grundahl, F., Collet, R., Mashonkina, L. I., Osorio, Y., & Barklem, P. S. 2013, Astronomy and Astrophysics, 555, A31

Gruyters, P., Nordlander, T., & Korn, A. J. 2014, Astronomy and Astrophysics, 567, A72

Gunn, J. E., Siegmund, W. A., Mannery, E. J., Owen, R. E., Hull, C. L., Leger, R. F., Carey, L. N., Knapp, G. R., York, D. G., Boroski, W. N., Kent, S. M., Lupton, R. H., Rockosi, C. M., Evans, M. L., Waddell, P., Anderson, J. E., Annis, J., Barentine, J. C., Bartoszek, L. M., Bastian, S., Bracker, S. B., Brewington, H. J., Briegel,

C. I., Brinkmann, J., Brown, Y. J., Carr, M. A., Czarapata, P. C., Drennan, C. C., Dombeck, T., Federwitz, G. R., Gillespie, B. A., Gonzales, C., Hansen, S. U., Harvanek, M., Hayes, J., Jordan, W., Kinney, E., Klaene, M., Kleinman, S. J., Kron, R. G., Kresinski, J., Lee, G., Limmongkol, S., Lindenmeyer, C. W., Long, D. C., Loomis, C. L., McGehee, P. M., Mantsch, P. M., Neilsen, Jr., E. H., Neswold, R. M., Newman, P. R., Nitta, A., Peoples, Jr., J., Pier, J. R., Prieto, P. S., Prosapio, A., Rivetta, C., Schneider, D. P., Snedden, S., & Wang, S.-i. 2006, The Astronomical Journal, 131, 2332

Hansen, C. J., Kawaler, S. D., & Trimble, V. 2004, Stellar interiors : physical principles, structure, and evolution

Harris, C. R., Millman, K. J., van der Walt, S. J., Gommers, R., Virtanen, P., Cournapeau, D., Wieser, E., Taylor, J., Berg, S., Smith, N. J., Kern, R., Picus, M., Hoyer, S., van Kerkwijk, M. H., Brett, M., Haldane, A., del Río, J. F., Wiebe, M., Peterson, P., Gérard-Marchant, P., Sheppard, K., Reddy, T., Weckesser, W., Abbasi, H., Gohlke, C., & Oliphant, T. E. 2020, Nature, 585, 357

Hayden, M. R., Bovy, J., Holtzman, J. A., Nidever, D. L., Bird, J. C., Weinberg, D. H., Andrews, B. H., Majewski, S. R., Allende Prieto, C., Anders, F., Beers, T. C., Bizyaev, D., Chiappini, C., Cunha, K., Frinchaboy, P., García-Herńand ez, D. A., García Pérez, A. E., Girardi, L., Harding, P., Hearty, F. R., Johnson, J. A., Mészáros, S., Minchev, I., O'Connell, R., Pan, K., Robin, A. C., Schiavon, R. P., Schneider, D. P., Schultheis, M., Shetrone, M., Skrutskie, M., Steinmetz, M., Smith, V., Wilson, J. C., Zamora, O., & Zasowski, G. 2015, The Astrophysical Journal, 808, 132

Hayden, M. R., Sharma, S., Bland-Hawthorn, J., Spina, L., Buder, S., Ciucă, I., Asplund, M., Casey, A. R., De Silva, G. M., D'Orazi, V., Freeman, K. C., Kos, J., Lewis, G. F., Lin, J., Lind, K., Martell, S. L., Schlesinger, K. J., Simpson, J. D., Zucker, D. B., Zwitter, T., Chen, B., Čotar, K., Feuillet, D., Horner, J., Joyce, M., Nordlander, T., Stello, D., Tepper-Garcia, T., Ting, Y.-s., Wang, P., Wittenmyer, R., & Wyse, R. 2022, Monthly Notices of the Royal Astronomical Society, 517, 5325

Holtzman, J. A., Hasselquist, S., Shetrone, M., Cunha, K., Allende Prieto, C., Anguiano, B., Bizyaev, D., Bovy, J., Casey, A., Edvardsson, B., Johnson, J. A., Jönsson, H., Meszaros, S., Smith, V. V., Sobeck, J., Zamora, O., Chojnowski, S. D., Fernandez-Trincado, J., Garcia-Hernandez, D. A., Majewski, S. R., Pinsonneault, M., Souto, D., Stringfellow, G. S., Tayar, J., Troup, N., & Zasowski, G. 2018, The Astronomical Journal, 156, 125

Hunt, E. L. & Reffert, S. 2023, Astronomy and Astrophysics, 673, A114

Jeffries, R. D., Naylor, T., Mayne, N. J., Bell, C. P. M., & Littlefair, S. P. 2013, Monthly Notices of the Royal Astronomical Society, 434, 2438

Jönsson, H., Holtzman, J. A., Allende Prieto, C., Cunha, K., García-Hernández, D. A., Hasselquist, S., Masseron, T., Osorio, Y., Shetrone, M., Smith, V., Stringfellow, G. S.,

Bizyaev, D., Edvardsson, B., Majewski, S. R., Mészáros, S., Souto, D., Zamora, O., Beaton, R. L., Bovy, J., Donor, J., Pinsonneault, M. H., Poovelil, V. J., & Sobeck, J. 2020, The Astronomical Journal, 160, 120

Kharchenko, N. V., Piskunov, A. E., Schilbach, E., Röser, S., & Scholz, R.-D. 2013, Astronomy and Astrophysics, 558, A53

King, J. R., Stephens, A., Boesgaard, A. M., & Deliyannis, C. 1998, The Astronomical Journal, 115, 666

Korn, A. J., Grundahl, F., Richard, O., Barklem, P. S., Mashonkina, L., Collet, R., Piskunov, N., & Gustafsson, B. 2006, , 442, 657

Korn, A. J., Grundahl, F., Richard, O., Mashonkina, L., Barklem, P. S., Collet, R., Gustafsson, B., & Piskunov, N. 2007, The Astrophysical Journal, 671, 402

Liu, F., Asplund, M., Yong, D., Feltzing, S., Dotter, A., Meléndez, J., & Ramírez, I. 2019, Astronomy and Astrophysics, 627, A117

Loebman, S. R., Debattista, V. P., Nidever, D. L., Hayden, M. R., Holtzman, J. A., Clarke, A. J., Roškar, R., & Valluri, M. 2016, The Astrophysical Journal Letters, 818, L6

Majewski, S. R., Schiavon, R. P., Frinchaboy, P. M., Allende Prieto, C., Barkhouser, R., Bizyaev, D., Blank, B., Brunner, S., Burton, A., Carrera, R., Chojnowski, S. D., Cunha, K., Epstein, C., Fitzgerald, G., García Pérez, A. E., Hearty, F. R., Henderson, C., Holtzman, J. A., Johnson, J. A., Lam, C. R., Lawler, J. E., Maseman, P., Mészáros, S., Nelson, M., Nguyen, D. C., Nidever, D. L., Pinsonneault, M., Shetrone, M., Smee, S., Smith, V. V., Stolberg, T., Skrutskie, M. F., Walker, E., Wilson, J. C., Zasowski, G., Anders, F., Basu, S., Beland, S., Blanton, M. R., Bovy, J., Brownstein, J. R., Carlberg, J., Chaplin, W., Chiappini, C., Eisenstein, D. J., Elsworth, Y., Feuillet, D., Fleming, S. W., Galbraith-Frew, J., García, R. A., García-Hernández, D. A., Gillespie, B. A., Girardi, L., Gunn, J. E., Hasselquist, S., Hayden, M. R., Hekker, S., Ivans, I., Kinemuchi, K., Klaene, M., Mahadevan, S., Mathur, S., Mosser, B., Muna, D., Munn, J. A., Nichol, R. C., O'Connell, R. W., Parejko, J. K., Robin, A. C., Rocha-Pinto, H., Schultheis, M., Serenelli, A. M., Shane, N., Silva Aguirre, V., Sobeck, J. S., Thompson, B., Troup, N. W., Weinberg, D. H., & Zamora, O. 2017, The Astronomical Journal, 154, 94

Martín, E. L., Lodieu, N., Pavlenko, Y., & Béjar, V. J. S. 2018, The Astrophysical Journal, 856, 40

Mészáros, S., Allende Prieto, C., Edvardsson, B., Castelli, F., García Pérez, A. E., Gustafsson, B., Majewski, S. R., Plez, B., Schiavon, R., Shetrone, M., & de Vicente, A. 2012, The Astronomical Journal, 144, 120

Michaud, G., Alecian, G., & Richer, J. 2015, Atomic Diffusion in Stars

Milone, A. P. & Marino, A. F. 2022, Universe, 8, 359

Myers, N., Donor, J., Spoo, T., Frinchaboy, P. M., Cunha, K., Price-Whelan, A. M., Majewski, S. R., Beaton, R. L., Zasowski, G., O'Connell, J., Ray, A. E., Bizyaev, D., Chiappini, C., García-Hernández, D. A., Geisler, D., Jönsson, H., Lane, R. R., Longa-Peña, P., Minchev, I., Minniti, D., Nitschelm, C., & Roman-Lopes, A. 2022, The Astronomical Journal, 164, 85

Nidever, D. L., Bovy, J., Bird, J. C., Andrews, B. H., Hayden, M., Holtzman, J., Majewski, S. R., Smith, V., Robin, A. C., García Pérez, A. E., Cunha, K., Allende Prieto, C., Zasowski, G., Schiavon, R. P., Johnson, J. A., Weinberg, D. H., Feuillet, D., Schneider, D. P., Shetrone, M., Sobeck, J., García-Hernández, D. A., Zamora, O., Rix, H.-W., Beers, T. C., Wilson, J. C., O'Connell, R. W., Minchev, I., Chiappini, C., Anders, F., Bizyaev, D., Brewington, H., Ebelke, G., Frinchaboy, P. M., Ge, J., Kinemuchi, K., Malanushenko, E., Malanushenko, V., Marchante, M., Mészáros, S., Oravetz, D., Pan, K., Simmons, A., & Skrutskie, M. F. 2014, The Astrophysical Journal, 796, 38

Nidever, D. L., Holtzman, J. A., Allende Prieto, C., Beland, S., Bender, C., Bizyaev, D., Burton, A., Desphande, R., Fleming, S. W., García Pérez, A. E., Hearty, F. R., Majewski, S. R., Mészáros, S., Muna, D., Nguyen, D., Schiavon, R. P., Shetrone, M., Skrutskie, M. F., Sobeck, J. S., & Wilson, J. C. 2015, The Astronomical Journal, 150, 173

Nordlander, T., Gruyters, P., Richard, O., & Korn, A. J. 2024, Monthly Notices of the Royal Astronomical Society, 527, 12120

Önehag, A., Gustafsson, B., & Korn, A. 2014, Astronomy and Astrophysics, 562, A102

Patton, R. A., Pinsonneault, M. H., Cao, L., Vrard, M., Mathur, S., García, R. A., Tayar, J., Daher, C. M., & Beck, P. G. 2024, Monthly Notices of the Royal Astronomical Society, 528, 3232

Paxton, B., Bildsten, L., Dotter, A., Herwig, F., Lesaffre, P., & Timmes, F. 2011, Astrophysical Journal Supplement, 192, 3

Paxton, B., Cantiello, M., Arras, P., Bildsten, L., Brown, E. F., Dotter, A., Mankovich, C., Montgomery, M. H., Stello, D., Timmes, F. X., & Townsend, R. 2013, Astrophysical Journal Supplement, 208, 4

Paxton, B., Marchant, P., Schwab, J., Bauer, E. B., Bildsten, L., Cantiello, M., Dessart, L., Farmer, R., Hu, H., Langer, N., Townsend, R. H. D., Townsley, D. M., & Timmes, F. X. 2015, Astrophysical Journal Supplement, 220, 15

Pence, W. 1999, in Astronomical Society of the Pacific Conference Series, Vol. 172, Astronomical Data Analysis Software and Systems VIII, ed. D. M. Mehringer, R. L. Plante, & D. A. Roberts, 487

Pinsonneault, M. H., Elsworth, Y. P., Tayar, J., Serenelli, A., Stello, D., Zinn, J., Mathur, S., García, R. A., Johnson, J. A., Hekker, S., Huber, D., Kallinger, T., Mészáros, S., Mosser, B., Stassun, K., Girardi, L., Rodrigues, T. S., Silva Aguirre, V., An, D., Basu, S., Chaplin, W. J., Corsaro, E., Cunha, K., García-Hernández, D. A., Holtzman, J., Jönsson, H., Shetrone, M., Smith, V. V., Sobeck, J. S., Stringfellow, G. S., Zamora, O., Beers, T. C., Fernández-Trincado, J. G., Frinchaboy, P. M., Hearty, F. R., & Nitschelm, C. 2018, Astrophysical Journal Supplement, 239, 32

Plez, B. 2012, Turbospectrum: Code for spectral synthesis

Price-Whelan, A. M., Hogg, D. W., Rix, H.-W., Beaton, R. L., Lewis, H. M., Nidever, D. L., Almeida, A., Badenes, C., Barba, R., Beers, T. C., Carlberg, J. K., De Lee, N., Fernández-Trincado, J. G., Frinchaboy, P. M., García-Hernández, D. A., Green, P. J., Hasselquist, S., Longa-Peña, P., Majewski, S. R., Nitschelm, C., Sobeck, J., Stassun, K. G., Stringfellow, G. S., & Troup, N. W. 2020, The Astrophysical Journal, 895, 2

Riello, M., De Angeli, F., Evans, D. W., Montegriffo, P., Carrasco, J. M., Busso, G., Palaversa, L., Burgess, P. W., Diener, C., Davidson, M., Rowell, N., Fabricius, C., Jordi, C., Bellazzini, M., Pancino, E., Harrison, D. L., Cacciari, C., van Leeuwen, F., Hambly, N. C., Hodgkin, S. T., Osborne, P. J., Altavilla, G., Barstow, M. A., Brown, A. G. A., Castellani, M., Cowell, S., De Luise, F., Gilmore, G., Giuffrida, G., Hidalgo, S., Holland, G., Marinoni, S., Pagani, C., Piersimoni, A. M., Pulone, L., Ragaini, S., Rainer, M., Richards, P. J., Sanna, N., Walton, N. A., Weiler, M., & Yoldas, A. 2021, Astronomy and Astrophysics, 649, A3

Sandage, A. 1957, The Astrophysical Journal, 125, 435

Santana, F. A., Beaton, R. L., Covey, K. R., O'Connell, J. E., Longa-Peña, P., Cohen, R., Fernández-Trincado, J. G., Hayes, C. R., Zasowski, G., Sobeck, J. S., Majewski, S. R., Chojnowski, S. D., De Lee, N., Oelkers, R. J., Stringfellow, G. S., Almeida, A., Anguiano, B., Donor, J., Frinchaboy, P. M., Hasselquist, S., Johnson, J. A., Kollmeier, J. A., Nidever, D. L., Price-Whelan, A. M., Rojas-Arriagada, A., Schultheis, M., Shetrone, M., Simon, J. D., Aerts, C., Borissova, J., Drout, M. R., Geisler, D., Law, C. Y., Medina, N., Minniti, D., Monachesi, A., Muñoz, R. R., Poleski, R., Roman-Lopes, A., Schlaufman, K. C., Stutz, A. M., Teske, J., Tkachenko, A., Van Saders, J. L., Weinberger, A., & Zoccali, M. 2021, arXiv e-prints, arXiv:2108.11908

Schiavon, R. P., Phillips, S. G., Myers, N., Horta, D., Minniti, D., Allende Prieto, C., Anguiano, B., Beaton, R. L., Beers, T. C., Brownstein, J. R., Cohen, R. E., Fernández-Trincado, J. G., Frinchaboy, P. M., Jönsson, H., Kisku, S., Lane, R. R., Majewski, S. R., Mason, A. C., Mészáros, S., & Stringfellow, G. S. 2024, Monthly Notices of the Royal Astronomical Society, 528, 1393

Schonhut-Stasik, J., Zinn, J. C., Stassun, K. G., Pinsonneault, M., Johnson, J. A., Warfield, J. T., Stello, D., Elsworth, Y., García, R. A., Mathur, S., Mosser, B., Hon, M., Tayar, J., Stringfellow, G. S., Beaton, R. L., Jönsson, H., & Minniti, D. 2024, The Astronomical Journal, 167, 50

Semenova, E., Bergemann, M., Deal, M., Serenelli, A., Hansen, C. J., Gallagher, A. J., Bayo, A., Bensby, T., Bragaglia, A., Carraro, G., Morbidelli, L., Pancino, E., & Smiljanic, R. 2020, Astronomy and Astrophysics, 643, A164

Shetrone, M., Bizyaev, D., Lawler, J. E., Allende Prieto, C., Johnson, J. A., Smith, V. V., Cunha, K., Holtzman, J., García Pérez, A. E., Mészáros, S., Sobeck, J., Zamora, O., García-Hernández, D. A., Souto, D., Chojnowski, D., Koesterke, L., Majewski, S., & Zasowski, G. 2015, Astrophysical Journal Supplement, 221, 24

Shetrone, M., Tayar, J., Johnson, J. A., Somers, G., Pinsonneault, M. H., Holtzman, J. A., Hasselquist, S., Masseron, T., Mészáros, S., Jönsson, H., Hawkins, K., Sobeck, J., Zamora, O., & García-Hernández, D. A. 2019, The Astrophysical Journal, 872, 137

Smith, V. V., Cunha, K., Shetrone, M. D., Meszaros, S., Allende Prieto, C., Bizyaev, D., García Pérez, A., Majewski, S. R., Schiavon, R., Holtzman, J., & Johnson, J. A. 2013, The Astrophysical Journal, 765, 16

Souto, D., Allende Prieto, C., Cunha, K., Pinsonneault, M., Smith, V. V., Garcia-Dias, R., Bovy, J., García-Hernández, D. A., Holtzman, J., Johnson, J. A., Jönsson, H., Majewski, S. R., Shetrone, M., Sobeck, J., Zamora, O., Pan, K., & Nitschelm, C. 2019, The Astrophysical Journal, 874, 97

Souto, D., Cunha, K., Smith, V., Allende Prieto, C., Pinsonneault, M., Zamora, O., García-Hernández, D. A., Mészáros, S., Bovy, J., García Pérez, A. E., Anders, F., Bizyaev, D., Carrera, R., Frinchaboy, P. M., Holtzman, J., Ivans, I., Majewski, S. R., Shetrone, M., Sobeck, J., Pan, K., Tang, B., Villanova, S., & Geisler, D. 2016, The Astrophysical Journal, 830, 35

Souto, D., Cunha, K., & Smith, V. V. 2021, The Astrophysical Journal, 917, 11

Souto, D., Cunha, K., Smith, V. V., Allende Prieto, C., García-Hernández, D. A., Pinsonneault, M., Holzer, P., Frinchaboy, P., Holtzman, J., Johnson, J. A., Jönsson, H., Majewski, S. R., Shetrone, M., Sobeck, J., Stringfellow, G., Teske, J., Zamora, O., Zasowski, G., Carrera, R., Stassun, K., Fernand ez-Trincado, J. G., Villanova, S., Minniti, D., & Santana, F. 2018, The Astrophysical Journal, 857, 14

Spoo, T., Tayar, J., Frinchaboy, P. M., Cunha, K., Myers, N., Donor, J., Majewski, S. R., Bizyaev, D., García-Hernández, D. A., Jönsson, H., Lane, R. R., Pan, K., Longa-Peña, P., & Roman-Lopes, A. 2022, The Astronomical Journal, 163, 229

Tayar, J. & Joyce, M. 2022, The Astrophysical Journal Letters, 935, L30

VandenBerg, D. A., Richard, O., Michaud, G., & Richer, J. 2002, The Astrophysical Journal, 571, 487

Vasiliev, E. & Baumgardt, H. 2021, Monthly Notices of the Royal Astronomical Society, 505, 5978

Virtanen, P., Gommers, R., Oliphant, T. E., Haberland, M., Reddy, T., Cournapeau, D., Burovski, E., Peterson, P., Weckesser, W., Bright, J., van der Walt, S. J., Brett, M., Wilson, J., Millman, K. J., Mayorov, N., Nelson, A. R. J., Jones, E., Kern, R., Larson, E., Carey, C. J., Polat, İ., Feng, Y., Moore, E. W., VanderPlas, J., Laxalde, D., Perktold, J., Cimrman, R., Henriksen, I., Quintero, E. A., Harris, C. R., Archibald, A. M., Ribeiro, A. H., Pedregosa, F., van Mulbregt, P., & SciPy 1.0 Contributors. 2020, Nature Methods, 17, 261

Viscasillas Vázquez, C., Magrini, L., Casali, G., Tautvaišienė, G., Spina, L., Van der Swaelmen, M., Randich, S., Bensby, T., Bragaglia, A., Friel, E., Feltzing, S., Sacco, G. G., Turchi, A., Jiménez-Esteban, F., D'Orazi, V., Delgado-Mena, E., Mikolaitis, Š., Drazdauskas, A., Minkevičiūtė, R., Stonkutė, E., Bagdonas, V., Montes, D., Guiglion, G., Baratella, M., Tabernero, H. M., Gilmore, G., Alfaro, E., Francois, P., Korn, A., Smiljanic, R., Bergemann, M., Franciosini, E., Gonneau, A., Hourihane, A., Worley, C. C., & Zaggia, S. 2022, Astronomy and Astrophysics, 660, A135

Wagner-Kaiser, R., Sarajedini, A., von Hippel, T., Stenning, D. C., van Dyk, D. A., Jeffery, E., Robinson, E., Stein, N., Anderson, J., & Jefferys, W. H. 2017, Monthly Notices of the Royal Astronomical Society, 468, 1038

Warfield, J. T., Zinn, J. C., Schonhut-Stasik, J., Johnson, J. W., Pinsonneault, M. H., Johnson, J. A., Stello, D., Beaton, R. L., Elsworth, Y., García, R. A., Mathur, S., Mosser, B., Serenelli, A., & Tayar, J. 2024, arXiv e-prints, arXiv:2403.16250

Wilson, J. C., Hearty, F. R., Skrutskie, M. F., Majewski, S. R., Holtzman, J. A., Eisenstein, D., Gunn, J., Blank, B., Henderson, C., Smee, S., Nelson, M., Nidever, D., Arns, J., Barkhouser, R., Barr, J., Beland, S., Bershady, M. A., Blanton, M. R., Brunner, S., Burton, A., Carey, L., Carr, M., Colque, J. P., Crane, J., Damke, G. J., Davidson, J. W., J., Dean, J., Di Mille, F., Don, K. W., Ebelke, G., Evans, M., Fitzgerald, G., Gillespie, B., Hall, M., Harding, A., Harding, P., Hammond, R., Hancock, D., Harrison, C., Hope, S., Horne, T., Karakla, J., Lam, C., Leger, F., MacDonald, N., Maseman, P., Matsunari, J., Melton, S., Mitcheltree, T., O'Brien, T., O'Connell, R. W., Patten, A., Richardson, W., Rieke, G., Rieke, M., Roman-Lopes, A., Schiavon, R. P., Sobeck, J. S., Stolberg, T., Stoll, R., Tembe, M., Trujillo, J. D., Uomoto, A., Vernieri, M., Walker, E., Weinberg, D. H., Young, E., Anthony-Brumfield, B., Bizyaev, D., Breslauer, B., De Lee, N., Downey, J., Halverson, S., Huehnerhoff, J., Klaene, M., Leon, E., Long, D., Mahadevan, S., Malanushenko, E., Nguyen, D. C., Owen, R., Sánchez-Gallego, J. R., Sayres, C., Shane, N., Shectman, S. A., Shetrone, M., Skinner, D., Stauffer, F., & Zhao, B. 2019, Publications of the Astronomical Society of the Pacific, 131, 055001

Zamora, O., García-Hernández, D. A., Allende Prieto, C., Carrera, R., Koesterke, L., Edvardsson, B., Castelli, F., Plez, B., Bizyaev, D., Cunha, K., García Pérez, A. E., Gustafsson, B., Holtzman, J. A., Lawler, J. E., Majewski, S. R., Manchado, A., Mészáros, S., Shane, N., Shetrone, M., Smith, V. V., & Zasowski, G. 2015, The Astronomical Journal, 149, 181

Zasowski, G., Cohen, R. E., Chojnowski, S. D., Santana, F., Oelkers, R. J., Andrews, B., Beaton, R. L., Bender, C., Bird, J. C., Bovy, J., Carlberg, J. K., Covey, K., Cunha, K., Dell'Agli, F., Fleming, S. W., Frinchaboy, P. M., García-Hernández, D. A., Harding, P., Holtzman, J., Johnson, J. A., Kollmeier, J. A., Majewski, S. R., Mészáros, S., Munn, J., Muñoz, R. R., Ness, M. K., Nidever, D. L., Poleski, R., Román-Zúñiga, C., Shetrone, M., Simon, J. D., Smith, V. V., Sobeck, J. S., Stringfellow, G. S., Szigetiáros, L., Tayar, J., & Troup, N. 2017, The Astronomical Journal, 154, 198

Zasowski, G., Johnson, J. A., Frinchaboy, P. M., Majewski, S. R., Nidever, D. L., Rocha Pinto, H. J., Girardi, L., Andrews, B., Chojnowski, S. D., Cudworth, K. M., Jackson, K., Munn, J., Skrutskie, M. F., Beaton, R. L., Blake, C. H., Covey, K., Deshpande, R., Epstein, C., Fabbian, D., Fleming, S. W., Garcia Hernandez, D. A., Herrero, A., Mahadevan, S., Mészáros, S., Schultheis, M., Sellgren, K., Terrien, R., van Saders, J., Allende Prieto, C., Bizyaev, D., Burton, A., Cunha, K., da Costa, L. N., Hasselquist, S., Hearty, F., Holtzman, J., García Pérez, A. E., Maia, M. A. G., O'Connell, R. W., O'Donnell, C., Pinsonneault, M., Santiago, B. X., Schiavon, R. P., Shetrone, M., Smith, V., & Wilson, J. C. 2013, The Astronomical Journal, 146, 81

VITA

Personal Background	Taylor Melissa Spoo La Vernia, TX Daughter of James Spoo Jr. and Bridget Redfern
Education	Diploma, La Vernia High School, La Vernia, TX, 2015 Bachelor of Science, Physics, Angelo State University, San Angelo, TX, 2019 Master of Science, Physics, Texas Christian University, Fort Worth, TX, 2021
Experience	Summer REU, University of Wisconsin - Madison, Madison, WI, 2018 Teaching assistantship, Texas Christian University, Fort Worth, 2019-2021 Research assistantship, Texas Christian University, Fort Worth, 2021
Professional Memberships	American Astronomical Society

ABSTRACT

MEASURING RELIABLE AGES FOR STARS: CALIBRATION OF THE [C/N] CHEMICAL CLOCK AND THE IMPACT OF ATOMIC DIFFUSION ON ABUNDANCE/AGE DETERMINATION OF MAIN SEQUENCE TURNOFF STARS

by Taylor M. Spoo, 2024
Department of Physics and Astronomy
Texas Christian University

Peter M. Frinchaboy III, Professor of Physics & Astronomy

In Galactic archeology, astronomers want to understand how the Milky Way formed and evolved. To be able to "time-stamp" events in chronological order, we need a reliable method to age-date large numbers of stars. Currently, the most reliable method is ages coming from star clusters, but they are limited in location and number. A useful tool to expand age-dating capabilities is chemical clocks: chemical abundances that are linked to stellar ages. In our work, we use open and globular clusters to establish a calibration between [C/N] and age, covering a metallicity range of $-1.2 \leq [Fe/H] \leq +0.3$ dex. With this improved calibration, we can determine ages for over 300,000 stars within the SDSS/APOGEE DR17 survey. While these chemical changes help us to estimate ages on the red giant branch, chemical changes can also hinder age estimations in other parts of the HR diagram. On the main sequence and near the turnoff, the surface abundances of a star change from a combination of gravitational settling and radiative acceleration working against it, a process known as atomic diffusion. In this case, the surface abundance is not an accurate prediction of the bulk abundances that determine

the stellar age. Recent studies suggest that this effect is not negligible, and in fact the ages derived from isochrones can be overestimated by 10-20% if atomic diffusion is not accounted for. We use SDSS/APOGEE DR17 to investigate atomic diffusion in the open clusters NGC 752 and Ruprecht 147 in order to constrain the variation of atomic diffusion signatures with age, and discuss how these results may affect the estimation of precise ages for subgiant stars.